USING SALT GRADIENT ENERGY AND THERMAL ENERGY TO ENHANCE REVERSE OSMOSIS DESALINATION

by

SANJANA YAGNAMBHATT

A dissertation submitted in partial fulfillment of the
requirements for the degree of

DOCTOR OF PHILOSOPHY IN MECHANICAL ENGINEERING

2024

Oakland University
Rochester, Michigan

Doctoral Advisory Committee:

Jonathan Maisonneuve, Ph.D., Chair
Laila Guessous, Ph.D.
Xia Wang, Ph.D.
Ziming Yang, Ph.D.
David Ladner, Ph.D. (observing member)

ACKNOWLEDGMENTS

In loving memory of my late father, Raghava Rao Chintalacheruvu, whose unwavering support, immeasurable encouragement, and profound wisdom were my guiding light throughout my academic journey, I dedicate this work. Your belief in the power of education and your commitment to my aspirations were the driving forces behind my quest for knowledge. This dissertation is a testament to the impact you've had on my lifetime.

I extend my heartfelt gratitude to my dissertation advisor, Dr. Jonathan Maisonneuve, whose mentorship, patience, expertise, and enthusiasm have been instrumental in shaping the direction of my research. Your insightful feedback, challenging questions, and constructive criticism have pushed me to achieve a higher standard of research and writing.

I am immensely grateful to my husband, Harsha Yagnambhatt. His patience, understanding, and belief in my abilities were instrumental in staying focused on my goals. Thank you for celebrating every milestone achieved, and for being my support system during both the highs and lows.

To the members of my dissertation committee, Dr. Xia Wang, Dr. Laila Guessous, Dr. Ziming Yang, and Dr. David Ladner, thank you for your time, expertise, and valuable insights. Their diverse perspectives and scholarly insights have enriched my work and challenged me to strive for greater depth and clarity.

I am deeply grateful to my mentors from Intel Corporation, DTE Energy and Borg Warner who have illuminated my path with their guidance, wisdom, and unwavering support.

I also wish to acknowledge the Graduate Fellowship from the School of Engineering and Computer Science at Oakland University, Scholarship from Society of Women Engineers and Intel Scholars Award by Intel Corporation.

I wish to acknowledge support from my mother and brother. Despite being separated by miles, their encouragement, love, and belief in my abilities were my constant companions throughout this journey.

To all those who have played a part, big or small, in supporting me during the completion of this dissertation, I extend my heartfelt thanks. Your contributions have made this achievement possible, and I am forever grateful for your presence in my life.

Sanjana Yagnambhatt

ABSTRACT

USING SALT GRADIENTS AND THERMAL ENERGY TO ENHANCE REVERSE OSMOSIS DESALINATION

by

SANJANA YAGNAMBHATT

Adviser: Jonathan Maisonneuve, Ph.D.

Improving desalination energy efficiency is crucial for meeting rising global water demands. Reverse osmosis (RO) is a common desalination process that uses an applied pressure to overcome the natural osmotic potential of seawater to drive nearly pure water permeate through a semipermeable membrane. However, it has high specific energy consumption ranging from 4-5 kWh/m^3 and environmental issues associated with discharging the highly concentrated brine that is left over after separation. This work investigates two methods of improving the energy efficiency of RO desalination: (1) Recovering salt gradient energy from desalination brine, and (2) Using thermal energy to pre-heat RO feed water and reduce mechanical pump work.

Through this work several scientific and technical advances are made. (1) A new maximum power point control strategy is developed for salt gradient energy systems, improving power by up to 44%. (2) Lab-scale implementation of this MPPT control strategy is shown to boost power density over threefold, from 0.6 W//m^2 to 2 W//m^2 for an osmotic energy system recovering energy from RO brine. (3) Using low grade heat, the power density of salt gradient energy systems is increased by up to 110%. (4) By

analyzing the energy balance of thermally enhanced RO, it is shown that the tradeoff between mechanical energy savings and thermal energy input can be favorable, and desalination energy was reduced by 12%

TABLE OF CONTENTS

TABLE OF CONTENTS—Continued

TABLE OF CONTENTS—Continued

TABLE OF CONTENTS—Continued

TABLE OF CONTENTS—Continued

LIST OF TABLES

LIST OF FIGURES

CHAPTER ONE
INTRODUCTION

1.1 Motivation

By 2050, water demand is expected to rise by 40% due to population growth [1–3]. Desalination is a means for meeting this increasing water demand because of its ability to use different sources of water that are unaffected by drought, such as brackish water and seawater, and its ability to produce water at different quality standards depending on the end use, such as drinking water, water for irrigation, and sanitation [4]. Currently, over 60% of clean water in the world is produced by desalination of seawater [5]. While seawater is abundant, the process of separating water from salt is energy intensive. At its thermodynamic limit, recovering 1 m^3 of freshwater from 2 m^3 of seawater (i.e. 50% recovery ratio) with a typical concentration of 35 g/l, requires approximately 0.5 kWh of energy [6]. However, desalination plants consume up to five times this amount of energy, and the associated greenhouse gas emissions are equivalent to 6.7 kg CO_2 per m^3 of water produced [7–9]. High energy consumption, environmental impact, and associated costs are the primary obstacles to increasing global freshwater production. The motivation of this work is to improve the energy efficiency of desalination to reduce its environmental footprint and increase water availability throughout the world.

1.2 Background

Reverse osmosis (RO) is the most popular desalination technology. It accounts for nearly 85 % of all desalination plants currently in operation and generates nearly 70% of all the water produced [5]. RO uses an applied pressure to overcome the natural osmotic

potential of seawater and drive nearly pure water to permeate through a semipermeable membrane. As shown in Figure 1.1, the system consists of a membrane, a high-pressure pump used to drive the permeate, and a pressure exchanger or energy recovery device that is used to recycle mechanical energy from the brine before it is discharged.

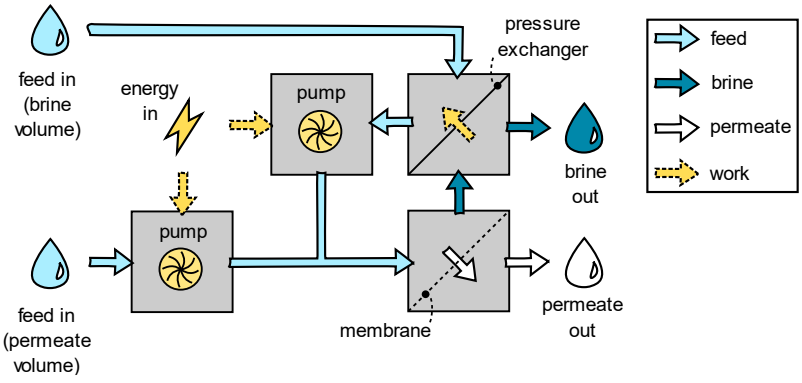

Figure 1.1 Schematic of a standard reverse osmosis (RO) desalination plant. Energy is supplied for mechanical pumping to pressurize feed solution above its osmotic potential, and thereby drive clean water permeate across the membrane. To reduce the pumping load, pressure is recycled from the remaining brine solution via a pressure exchanger.

The invention of the practical, semi-permeable asymmetric cellulose acetate membrane by Dr. Sidney Loeb and Dr. Srinivasa Sourirajan at the University of California, Los Angeles in 1956 revolutionized water desalination by reverse osmosis [10]. Shortly thereafter, in 1965, Dr. Loeb installed the first municipal reverse osmosis desalination plant in Coalinga, California. This plant used tubular membrane modules and had the capacity to produce 5,000 gallons of fresh water per day [11]. Since this pioneering work, the research and development of RO membranes and processes has followed several major trends.

1.2.1 Development of High-Performance Membranes

Most research on improving the water flux output of RO has focused on developing new membranes that are more permeable to water, more selective to salt, and can withstand more pressure. Most RO membranes are currently designed to withstand pressures of up to ~80 bar [12]; however, recent developments have achieved an increase in this burst pressure to up to 110 bar [13]. The upper limit of the membrane permeability is approximately 1-3 lmh/bar for seawater desalination [14]. Beyond this limit, the benefits associated with increased permeability tend to diminish (e.g., a decrease in the energy consumption at a constant permeate flux, an increase in the water flux, or operation at higher recovery ratios) [14,15]. Current membrane permeability achievable by spiral-wound RO membranes is decent enough because it approaches the operational limits set by thermodynamics and mass transfer limitations. Research suggests that increasing membrane selectivity should be targeted rather than an increase in water permeability. This shift in focus is driven by the current demand for advancements in product quality rather than solely emphasizing the quantity of permeate.

1.2.2 Strategies for Mitigating Membrane Fouling

Another important RO research trend has focused on tackling membrane fouling, which leads to increased energy consumption and operational costs for desalination plants. Fouling refers to the unwanted buildup of deposits on the membrane surface, leading to a reduction in the water permeate flux and an increase in the passage of solutes across the membrane [16]. Fouling reduces membrane life and membrane water permeability and increases pretreatment costs and membrane cleaning frequency. Over time, this leads to a higher applied pressure requirement to obtain the same amount of

water flux from the membrane. The fouling type and intensity depend on the feed water quality, membrane type, and operating conditions. Strategies to combat fouling include surface modification to make the membrane hydrophilic and smooth, pretreatment of feed water to remove contaminants before sending the water to the RO process, cleaning the membrane surface frequently, introducing air bubbles on the membrane to cause turbulence, and monitoring the membrane in real time to detect fouling in its early stages[17–20].

1.2.3 Energy Efficiency

RO systems are widely used for desalination and are energy intensive, consuming as high as 4-5 kWh/m^3 [7,21]. RO is the most widely used process, accounting for almost 85% of desalination plants, because its energy footprint is less than half that of other thermal desalination technologies. Figure 1.2 shows the specific energy consumption of RO compared with other desalination technologies, such as multistage-flash distillation and multi-effect distillation.

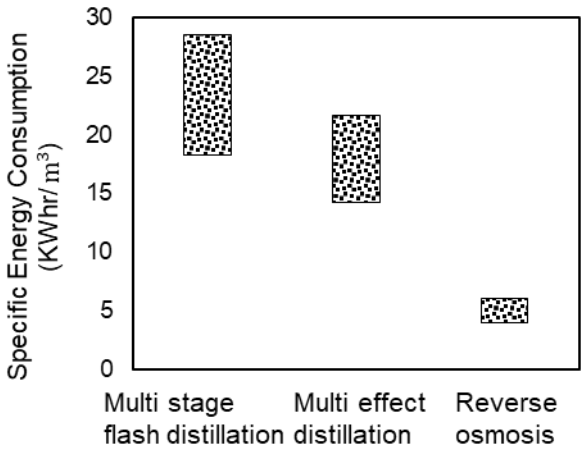

Figure 1.2 Specific energy consumption of RO compared with other desalination processes [22].

There is a need to reduce the energy consumption of RO desalination to reduce the associated carbon emissions and make RO more cost effective and environmentally friendly. Methods to reduce the electrical energy consumption of the RO process include (i) using energy recovery devices, (ii) multi-stage RO processes, (iii) batch RO, and (iv) using renewable energy to power RO.

Energy recovery devices are employed in RO plants to recover mechanical energy from the RO concentrated output and reuse it to pressurize the input feed water to potentially reduce the specific energy consumption of the RO desalination process. Energy recovery devices can potentially aid in reducing the size of the high-pressure pump used to supply the feed stream to the membrane module. In the early stages, centrifugal type energy recovery devices were used. Currently, isobaric chamber energy recovery devices with better energy efficiency are being used. There is limited scope for

further development in this area [23,24]. The energy savings associated with integrating these with RO plants were approximately 80% [25,26].

In a single-stage RO process, the osmotic pressure that must be overcome to produce a water flux is uneven throughout the membrane. This is because of the increase in the feed osmotic pressure as we pass through the membrane from the inlet to the outlet. However, a constant pressure is applied throughout the membrane system, and a large amount of energy is dissipated at the inlet of the membrane system, where the osmotic potential between the feed and permeate, which must be overcome to produce a water flux, is the lowest. To mitigate this loss, research efforts have led to two different process designs: (i) multistage RO and (ii) batch RO. In multistage RO, different RO membrane systems exist, where the solution passes from one stage (membrane system) to the other, and the pressure applied is tailored to the osmotic potential in each stage. In the batch RO process, the concentrated brine output from the feed is recirculated as the feed stream in a single RO membrane system until the brine is concentrated and beyond the scope of RO to be desalinated [27]. The energy savings associated with implementing multi-stage RO process is reported to be around 30% for seawater desalination [28] while those associated with implementing batch RO process are reported to be 64% for brackish water desalination and 23% for seawater desalination [27]. Although the energy savings are slightly higher for multistage RO, the batch process is more realistic than the multi-stage approach.

RO desalination can be powered with renewable energy sources, such as wind energy[29–32] and solar PV panels [33–36] to reduce environmental impact associated with high electrical energy consumption. Additionally, heat can serve as an alternative

power source for RO operations. Examples include, geothermal energy [37], organic Rankine cycle powered RO[38–42], ocean thermal energy [43], and thermal piston-powered RO [44–46].

1.3 Objectives

This dissertation will investigate two strategies to reduce energy consumption and improve the energy efficiency of RO desalination: (1) recovering energy from RO brine and (2) using low-grade heat to enhance water permeation.

1.3.1 Objective 1: Improve Osmotic Power Processes to Recover Energy from Desalination Brine

Despite being the most widely commercialized desalination technology, RO systems have drawbacks, including high specific energy consumption ranging from 4-5 kWh/m^3 as previously mentioned, and environmental issues associated with discharging the highly concentrated brine that is left over after separation [7,21]. It is common for desalination plants to discharge brine at a concentration of 70 g/l [47]. This is considered to be the most impactful environmental issue with regard to seawater desalination plants [48,49]. The salinity of seawater should remain at approximately 35-40 g/l to ensure the health and survival of marine species [49,50]. Some brine management systems have attempted to mitigate this problem by pumping discharge below the surface level into nutrient-rich areas. However, this process has been seen to cause eutrophication of the water from the excess nutrients, creating “dead zones” in which marine organisms cannot survive [48].

Interestingly, this problem presents an opportunity for future research. High concentration RO brine can also provide a valuable source of salt gradient energy, and if properly managed, both the environmental impact and energy efficiency of RO could be

improved. Energy can be recovered from RO brine by harnessing the chemical potential difference between highly concentrated RO brine and low-concentration solutions such as wastewater, river water, and brackish water. RO process can be coupled with electrochemical processes, such as reverse electrodialysis [51], or with osmotic processes, such as pressure-retarded osmosis (PRO) [52], to recover the chemical potential from brine and supply it back to the RO process using an energy recovery device.

PRO can generally achieve high power densities with cheaper membranes than reverse electrodialysis [53]. Therefore, our focus is on coupling RO with the PRO process to recover energy from salt gradients. Figure 1.3 provides an illustration of the basic PRO concept. In this process, high concentration draw solution (such as

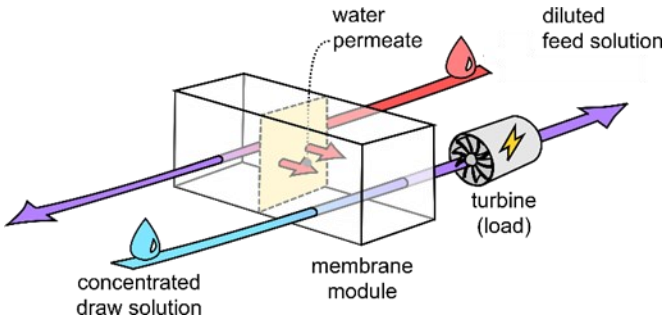

Figure 1.3 Concentrated solution such as seawater or desalination brine can be used to draw water permeate across a semi-permeable membrane from a diluted feed source to do positive work on a load such as a turbine.

desalination brine) is supplied to a membrane module and used to draw water permeate from a lower concentration feed source (such as seawater or other wastewater) against a

load (such as a turbine of some kind). Thus, the high osmotic potential of the draw solution was converted into useful mechanical work.

The RO-PRO concept is illustrated in Figure 1.4. In this system, high concentration RO brine is supplied to the PRO module under pressure and used to draw water from a relatively low concentration source, producing an expanding volume of pressurized fluid, which can do work on a load. If a pressure exchanger is used as the load, the salt gradient energy is effectively recycled back to the RO feed, reducing the load on the RO pump and saving energy.

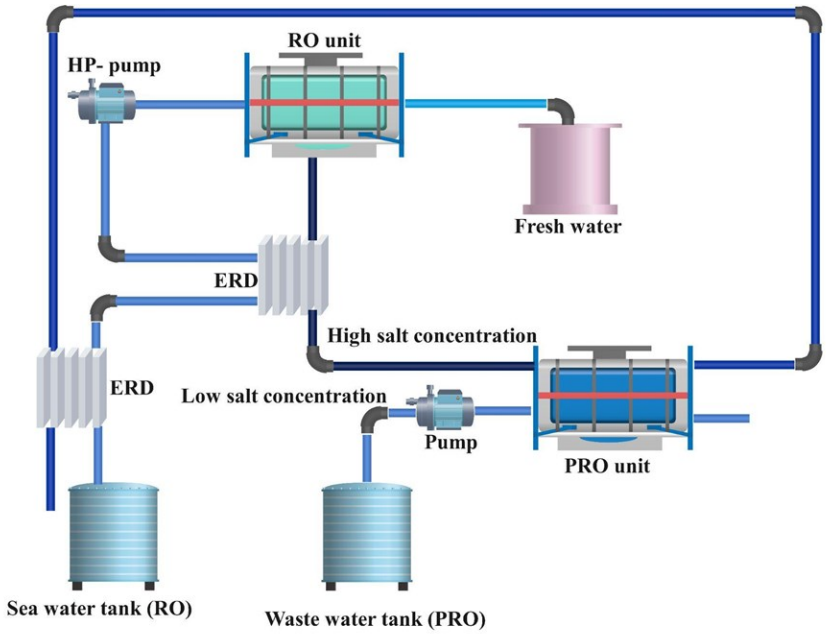

Figure 1.4 Schematic of the RO-PRO concept which recovers energy from desalination brine and recycles it back to pressurize seawater feed and thereby reduce RO energy use.

Coupling RO with PRO is shown to reduce energy consumption of RO process by up to 40 % [54–59]. In addition to energy savings, another favorable byproduct of coupling RO with PRO is the dilution of high concentration RO brine which otherwise is very harmful to marine life. The PRO energy recovery system can dilute the brine discharge from as high as 70 g/l to an acceptable concentration of 40 g/l or lower [47,60,61], which is much closer to bulk seawater concentrations and therefore significantly reduces the environmental impact.

Based on Statkraft's initial commercialization efforts of PRO from 2009 to 2013, it could not be economically viable owing to its limited energy potential and expenses associated with pretreating solutions before being supplied to the PRO system [62,63]. At the time, research mainly focused on PRO as a standalone power generation technology. High-performance membranes that boost performance have recently become commercially available. When PRO is coupled with RO, pretreatment costs are eliminated. Although these advancements are a step towards solving the problem of commercialization of PRO, there needs to be more focus on process improvement to fully utilize the potential of PRO in reducing the energy consumption of desalination.

Optimizing the operating parameters of the PRO process can significantly improve the PRO power output. So far, the focus has been on optimizing only the applied pressure, which leads to the maximum PRO power. Previously proposed methods to optimize the applied pressure include implementing a model-based maximum power point controller, mass feedback, and fuzzy logic controls for tracking the maximum power point and the Grey Wolf optimization algorithm [64–66]. The methods proposed thus far have ignored the trade-off between gross power and net power. There is a need for an automated

controller that accounts for this trade-off while adjusting the important operating parameters, including the supply rates of the feed and draw solutions and the applied pressure load, to ensure maximum net power operation of the PRO process. Therefore, the first objective of this dissertation is to improve the energy efficiency of the PRO process to significantly reduce the energy consumption of RO desalination.

1.3.2 Objective 2: Evaluate the Potential of Using Low-Grade Heat to Reduce the Specific Energy of RO Desalination

At present, very huge amounts of low grade heat which is estimated to be 72% of the global primary energy produced [67] from various sources such as industrial thermal processes, solar and geothermal energies is considered waste heat and not utilized efficiently [68]. The industrial waste heat in the EU is estimated to be 300 TW-h per year, excluding power plants and transportation. [67,69]. In the USA, 4000 TW-h of waste heat is available annually from the condensers of power plants in the temperature range of 40–49 °C [67,70]. The recovery and utilization of low-grade heat is an attractive and significant method for efficiently decreasing fossil fuel depletion and contaminant emissions.

Low-grade heat can be used to improve PRO performance, thereby reducing the electric energy consumption of the RO process. The PRO process can be improved when low-grade heat is supplied either to the feed or draw solutions or to both solutions. Figure 1.5 demonstrates the concept of thermally enhanced PRO, where heat is used to improve the PRO performance. Here the heat is supplied to feed solution. A significant increase in PRO power can be achieved via the application of low-grade heat, reaching 200 % [71]. This indicates that the energy savings of the RO process can be significantly improved

when PRO is supplied with hot solutions. Wang et al showed that increasing PRO operating temperatures from 20℃ to 50 ℃ reduced RO energy consumption by almost 20% in a RO-PRO system [72].

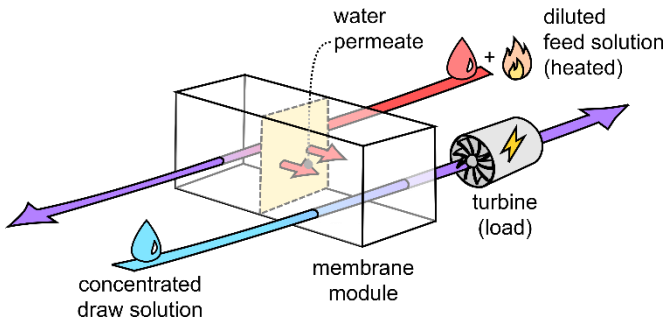

Figure 1.5 Concept of thermally-enhanced pressure retarded osmosis (PRO) where heat is supplied to the feed solution to improve the performance of PRO

Similarly, the energy consumption of the standalone RO process can be significantly reduced when heat is supplied to the RO feed. The concept of thermally enhanced RO is shown in Figure 1.6, where low-grade heat is supplied to the feed solution, and energy savings as high as 40% are observed when low-grade heat is supplied to brackish water in the RO desalination process [73].

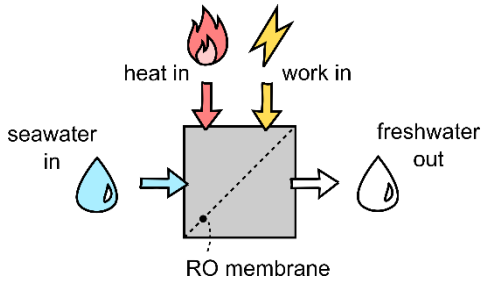

Figure 1.6 Concept of thermally enhanced Reverse Osmosis process where heat is supplied to the RO feed to reduce energy consumption of the RO process

Therefore, the second objective of this dissertation is to understand the dynamics behind this improvement with the addition of heat to both PRO and RO processes. The transport dynamics underlying this improvement at elevated operating temperatures have not yet been investigated. Current literature emphasizes energy savings in RO and the augmentation of power density of PRO. However, there exists a critical need to shift focus towards comprehending the dynamics that foster these improvements. This strategic redirection is imperative to optimize the utilization of heat resources effectively.

Low-grade heat is considered a free resource, and the heat energy supplied to the system is unaccounted for in the literature to date. This suggests that the energy savings are overestimated for cases in which low-grade heat is not a free resource. This also indicates the need to optimize the operating temperature to effectively use heat when it is not a free resource.

For thermally enhanced osmotic processes to make technical and economic sense, the performance improvement must be sufficient to justify the additional capital and operational costs associated with supplying heat to the system. Thermal enhancement is advantageous only if the heat is inexpensive relative to electric power.

1.4 Outline

In Chapter Two, a maximum power point tracking (MPPT) control strategy for the real-time and simultaneous control of PRO operating parameters is proposed, including not only the applied pressure, but also the feed and draw solution supply rates for the first time. This allowed us to obtain the maximum net power from the PRO system. The ability of the system to achieve the maximum net power output was demonstrated for various commercial membranes for both stand-alone PRO and combined RO-PRO

applications. A specific control algorithm involving an alternating sequence of perturb and observe is described, and both the steady-state and dynamic performance of the system are compared with a system operating under default operating conditions for a variety of PRO applications. The results provide insight into the optimal operating conditions that are case-specific.

In Chapter Three, the concept of real-time maximum power point tracking for a salt gradient osmotic power system is demonstrated experimentally for the first time in the literature. The transient response of a laboratory-scale osmotic system is characterized, showing water permeate flux, pressure losses, and power output in response to step changes in applied pressure and feed and draw circulation rates. A "perturb and observe" feedback algorithm and control strategy are implemented on a PRO system for both energy recovery from RO brine and standalone power generation. The role of the perturbation signal size and interval between steps in improving the MPPT algorithm performance is discussed, and recommendations are made on how to reduce the time taken by the MPPT algorithm to converge to a steady state.

In Chapter Four, the process of thermally enhanced PRO is investigated. Laboratory test trials of thermally enhanced PRO were conducted across a range of temperatures, and the results were used to validate a finite element model that described the concentration and temperature profiles across the membrane. This model addresses the shortcomings of other published PRO transport models and provides insights into the transport dynamics that lead to improved performance at higher temperatures. In addition, we introduce an effectiveness metric, which normalizes power improvements relative to temperature changes. The effectiveness of a range of feed and draw temperatures was evaluated. This

metric helps to optimize the operating temperature to reap the maximum benefits from heat, particularly when it is not a free resource.

In Chapter Five, the thermally enhanced RO process is investigated, accounting for the heat energy in the energy balance for the first time in the literature. The tradeoff between the thermal energy input and mechanical pump savings at elevated temperatures was analyzed. An analytical model was developed and used to establish the energy balance of both the conventional and thermally enhanced RO systems. The model was run under different operating conditions, for example, using different source water concentrations, such as seawater, brackish water, and oil and gas produced water, to identify circumstances that lead to a balance between heat energy input and electric energy savings. The model was also run with different membrane properties (permeability and selectivity), operating targets (water permeate rates and feed recovery ratios), equipment specifications (thermal and mechanical efficiencies), and environmental conditions (ambient temperatures) to identify any pattern associated with achieving a balance between heat energy input and electric energy savings.

Chapter Six outlines areas for future research that would enable further improvement in the energy savings of the desalination process. The application of the MPPT control strategy to develop a strategy to find the minimum specific energy consumption tracking point of a thermally enhanced RO system is proposed. This control strategy would be able to predict the operating temperatures that would lead to reduced RO electric energy consumption, while maintaining the desired energy balance between heat energy input and electric energy savings. As a next step, an economic analysis is proposed to determine the cost of water produced when thermal energy is added to an RO system to

reduce energy consumption. This would help understand whether the addition of heat to a desalination process can be economically justified after considering the associated capital and operating costs.

1.5 Publications

This work produced a total of four journal papers, three conference oral presentations, three conference poster presentations, and one technical report.

1.5.1 Journal Papers

1. S. Yagnambhatt, S. Khanmohammaddi, J. Maisonneuve "Demonstration of a Real-Time Maximum Power Point Tracker for Salt Gradient Osmotic Power Systems," In preparation.

2. S. Yagnambhatt, S. Khanmohammaddi, J. Maisonneuve, "Reducing the Specific Energy Use of Seawater Desalination with Thermally Enhanced Reverse Osmosis," Desalination, Vol. 573: 117163, 2024. DOI: 10.1016/j.desal.2023.117163

3. S. Chintalacheruvu, Y. Ren, and J. Maisonneuve, "Effectively using heat to thermally enhance pressure retarded osmosis," Desalination, Vol. 556: 116570, 2023. DOI: 10.1016/j.desal.2023.116570

4. J. Maisonneuve, S. Chintalacheruvu, "Increasing osmotic power and energy with maximum power point tracking," Applied Energy, Vol. 238, 2019. DOI: 10.1016/j.apenergy.2019.01.110.

1.5.2 Conference Presentations

1. S.Yagnambhatt, S. Khanmohammadi, and J. Maisonneuve, "Reducing the Specific Energy Use of Seawater Desalination With Thermally-Enhanced Reverse Osmosis." Oral presentation, 18th International Conference on Energy Sustainability (ES2024), American Society of Mechanical Engineers (ASME), Anaheim, CA, July 2024

2. S.Yagnambhatt, S. Khanmohammadi, and J. Maisonneuve, "Demonstration of a Real-Time Maximum Power Point Tracker for Salt Gradient Osmotic Power Systems." Poster presentation, North American Membrane Society (NAMS), Santa Fe, NM, May 2024

3. S. Chintalacheruvu, Y. Ren, and J. Maisonneuve, "Effectively Using Heat to Thermally Enhance Osmotic Processes for Power Generation and Desalination."

Oral presentation, North American Membrane Society (NAMS), Tuscaloosa, AL, May 2023

4. S. Chintalacheruvu, S. Khanmohammadi, and J. Maisonneuve, "Effectively Using Heat to Thermally Enhance Reverse Osmosis and Reduce Specific Energy Consumption of Desalination." Poster presentation, North American Membrane Society (NAMS), Tuscaloosa, AL, May 2023

5. S. Chintalacheruvu and J. Maisonneuve, "Effectively Using Heat to Thermally Enhance PRO," Oral presentation, Society of Women Engineers (SWE) Women in Engineering Conference (WE), Houston, TX, October 2022

6. S. Chintalacheruvu and J. Maisonneuve, "Effectively Using Heat to Thermally Enhance Osmosis," Poster presentation, North American Membrane Society (NAMS), Estes Park, CO, August 2021

1.5.3 Technical Reports

1. S. Averitt, S. Chintalacheruvu (lead), S. Khanmohammadi, N. Lemmons, D. Zehler, Harnessing the Energy of Saltwater Gradients to Improve the Efficiency of Seawater Desalination, U.S. DOE Marine Energy Collegiate Competition 2023. https://drive.google.com/drive/folders/1U48lSUXDwlodrTPBDkQzmpZsNy7IswIc

CHAPTER TWO
INCREASING OSMOTIC POWER AND ENERGY WITH MAXIMUM POWER POINT TRACKING

2.1 Introduction

Chemical potential energy is released as entropy when solutions of different concentrations mix, for example when river water meets the sea [74]. Pressure retarded osmosis (PRO) has been proposed as one method of converting this potential energy to useful work [61,75–78]. During the PRO process, diluted and concentrated solutions (referred to as feed and draw solutions) are supplied to opposite sides of a semi-permeable membrane, and some load (such as a hydro turbine) is placed at the concentrated side of the membrane outlet. Under such an arrangement, solvent will spontaneously permeate across the membrane via osmosis and do work on the load.

To produce maximum power and recover maximum energy from PRO it is necessary to carefully balance the gross output of the system against parasitic loads [79,80]. Experimental investigation and thermodynamic analysis has demonstrated in recent years that this can be achieved by operating the system with specific loading and with specific flow rates for diluted and concentrated supply streams [79,80]. Importantly, these studies have shown that operating conditions are highly case specific and dependent on materials, site conditions, and other constraints [81–84]. This has therefore motivated the development of various modeling tools for PRO design optimization [81–84]. While

---

Chapter Two is based primarily on a paper that was published in the Journal of Applied Energy.

J. Maisonneuve, S. Chintalacheruvu, "Increasing osmotic power and energy with maximum power point tracking," Applied Energy, Vol. 238, 2019. DOI: 10.1016/j.apenergy.2019.01.110.

necessary, such design efforts are ultimately limited by both the accuracy of the modeled system, and perhaps more importantly the inability to adapt design and operation in real-time in response to changing environmental conditions, material properties, and others.

More recently, the real-time control of osmotic power systems has been proposed using maximum power point tracking (MPPT), however critically these approaches have been limited to control of only a single parameter, that is applied pressure [65,66,85]. These systems have suggested the use of several control strategies such as perturb and observe (P&O), incremental mass resistance, mass feedback control, fuzzy logic and whale optimization. While these have shown the ability to optimize loading and thereby increase power output, they leave significant room for improvement as they omit the importance of additional control parameters that also affect performance, namely control of feed and draw flow rates. There is as yet not been any control strategy proposed in the literature for the real-time and simultaneous control of applied pressure, feed flow rates, and draw flow rates. This lack of a systematic approach to setting operating conditions has led in part to questions about whether the net power in PRO can in fact be positive, even with high gross power outputs [86,87].

This chapter addresses this gap in the literature and proposes a system for the real-time and simultaneous control of PRO operating parameters, including not only hydraulic loading, but also for the first-time feed and draw supply rates. This allows for obtaining maximum net power and maximum specific energy from the PRO system at both design stage, as well as in the field in response to changing conditions. A specific control algorithm involving an alternating sequence of P&O is described and both steady-state

and dynamic performance of the system is compared against a default system for a variety of PRO applications.

2.2 Theory

2.2.1 Controlling Operating Conditions

A simplified PRO power system is shown in Figure 2.1. The system consists of a membrane supplied by feed and draw pumps, with a turbine load placed on the draw side. This schematic omits the pressure exchanger that is generally used to recover energy from the pressurized draw stream, and thereby reduce load and associated losses on the draw pump.

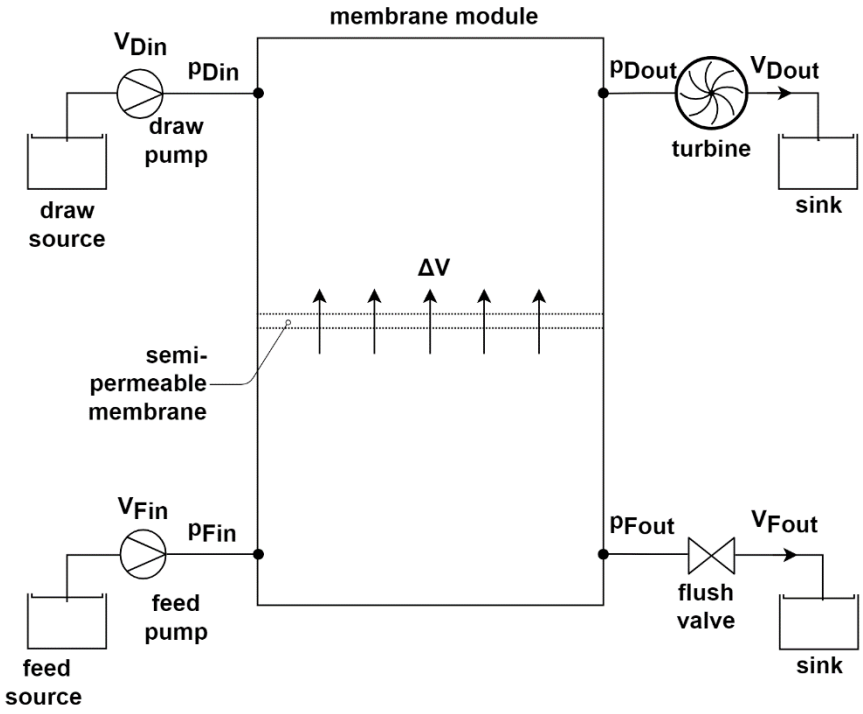

Figure 2.1 Simplified osmotic power system configuration.

The net rate of work available from such a PRO system $\dot{W}$ is given by the difference between power produced at the turbine and power consumed by the pumps,

$$\dot{W} = p_{D,out}\,\dot{V}_{D,out} - p_{D,in}\,\dot{V}_{D,in} - p_{F,in}\,\dot{V}_{F,in} \tag{2.1}$$

Flow rates $\dot{V}$ and pressures p are labelled in Figure 2.1.

In an ideal system, it is assumed that flow is frictionless and therefore $p_{D,in} = p_{D,out}$, and $p_{F,in} = 0$. Under these condition, the expression for net power reduces to the following, which is commonly associated with PRO power,

$$\dot{W} = \Delta p\,\dot{V}_P \tag{2.2}$$

Where Δp is the applied pressure difference across the membrane, and $\Delta\dot{V}$ is the permeate volume. Permeate is driven by osmotic pressure difference across the membrane $\Delta\pi$, and opposed by the applied pressure difference Δp (hence the term *pressure retarded*), as described in the following expression,

$$\frac{\dot{V}_P}{a} = J_w = A\,(\Delta\pi - \Delta p) \tag{2.3}$$

Where A is the membrane's permeability to water. When normalized over the surface area of the membrane a, the permeate can be written as water flux J_w.

Under such ideal conditions maximum power is obtained when $\Delta p = \Delta\pi / 2$. This pressure is obtained when the load presents the same resistance to flow as does the membrane (in a way that is analog to the voltage divider rule for maximum power transfer in a resistive circuit). Such conditions yield the theoretical limit to PRO power, which can be derived from eqs. (2) and (3),

$$\frac{\dot{W}_{limit}}{a} = A\,\frac{\Delta\pi^2}{4} \tag{2.4}$$

This power represents the theoretical maximum that can be obtained from an osmotic potential across a membrane.

In reality however, flow is viscous and pressure losses through the membrane module and throughout the system reduce power as well as shift the best applied pressure away from the theoretical point. In practice it is difficult to accurately anticipate the real osmotic pressure available across the membrane, and therefore difficult to set the appropriate applied pressure. For this reason, MPPT control algorithms have been proposed as effective means of identifying and operating at pressures that yield maximum power [65,66,85].

Eq. (2.1) also suggests that net power output can be increased by reducing the pumping power by using low operating flow rates $\dot{V}_{F,in}$ and $\dot{V}_{D,in}$. Extending this analysis suggests that ideally all feed volume would permeate the membrane $\dot{V}_{F,in} = \dot{V}_w$ (i.e. permeate recovery rate would approach 100 %) and that the draw flow rate $\dot{V}_{D,in}$ would approach zero. This is impractical however, for several reasons. These conditions lead to severe axial variations in the feed and draw concentrations and a rapid drop in the driving osmotic pressure difference [88,89]. The result is a severe drop in the power available for extraction at the turbine, and ultimately a drop in net power output. Cross flow rates need to be sufficiently high so as to maintain viable water flux and power density along the whole membrane surface. Also, pumping low volumes of feed and draw solutions through the membrane leads to severe external concentration polarization across thick boundary layers that develop due to reduced mixing action. Up to a certain point and in

certain cases, investing energy for additional pumping can be justified by the improved osmotic performance and power output. These tradeoffs have previously been demonstrated and discussed [81].

Maximum power transfer in PRO therefore requires that not only applied pressure, but also supply flow rates, be carefully controlled in an effort to minimize the overall effect that non-ideal phenomena have on power. Figure 2.2 suggests one strategy for controlling pressure and flow in a PRO system. The closed loop system achieves the desired operating conditions by coordinated control of the feed pump, draw pump, and load. This strategy can be implemented by supplying flow rate commands to variable speed pumps and resistance commands to variable load (or switching commands to power electronics in the case where the turbine is coupled to a generator with power converter). Specific values for these commands are determined by the control algorithm of choice. In the case of an MPPT algorithm, the controller receives feedback from measurement of net power generated by the PRO system.

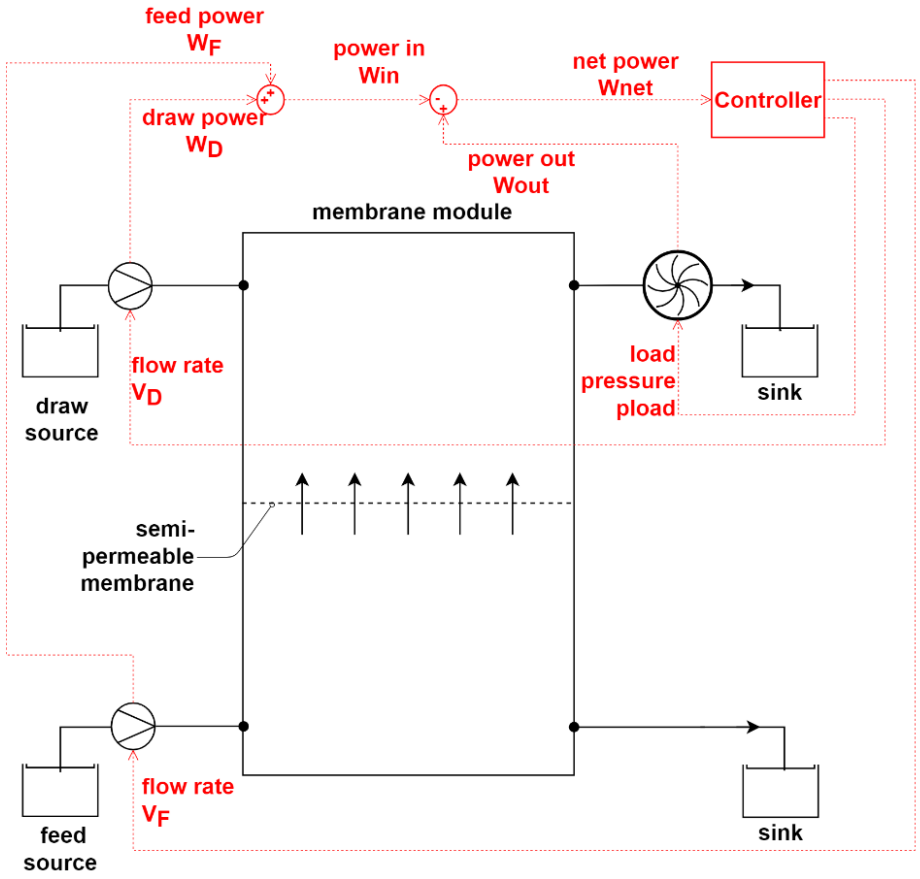

Figure 2.2 Maximum power point tracking in osmotic power system via feedback control of pump speed and load

2.2.2 Tracking Maximum Power

The feedback controller supplies signals to pumps and loads, and can be designed to accomplish a variety of operational objectives. For example, it could be designed to maintain certain feed recovery ratios, or certain mixing ratios. In this case, we propose a controller for operation at maximum net power output and another for operation at maximum energy recovery. Maximum power point tracking can be done with a variety of feedback control algorithms. Several algorithms have been proposed for PRO [65,66,85] and many others have also been developed for various applications [90–92]. Here, we

propose a simple perturb and observe (P&O) system in order to highlight the novelty of simultaneous control of loading as well as flow rates.

The P&O control logic for maximum power tracking is shown in Figure 2.3. The technique applies a common 'hill climbing' approach by taking steps towards the maximum power target via incremental changes in the operating parameters. Feedback from measured power output provides the signal to the algorithm to either repeat beneficial incremental changes, or reverse if they are detrimental. Because maximum power occurs at a unique combination of both flow rates and outlet pressure, this P&O method is applied to each of the operating variables in an alternating sequence. Figure 2.3 shows the sequence beginning with adjustment to the load pressure p_{load}, although the choice of starting variable is arbitrary. This first variable is varied by some step Δp_{load}, and the response of net power is sampled at some time interval δt. If the response is positive, the load is further varied. If the response is negative, the load opposites varied by a step in the opposite direction. Iteration continues over some period Δt, after which the first control signal is held constant, and the iterative process is applied to the second control variable $\dot{V}_D$. And so on for the third control variable $\dot{V}_F$.

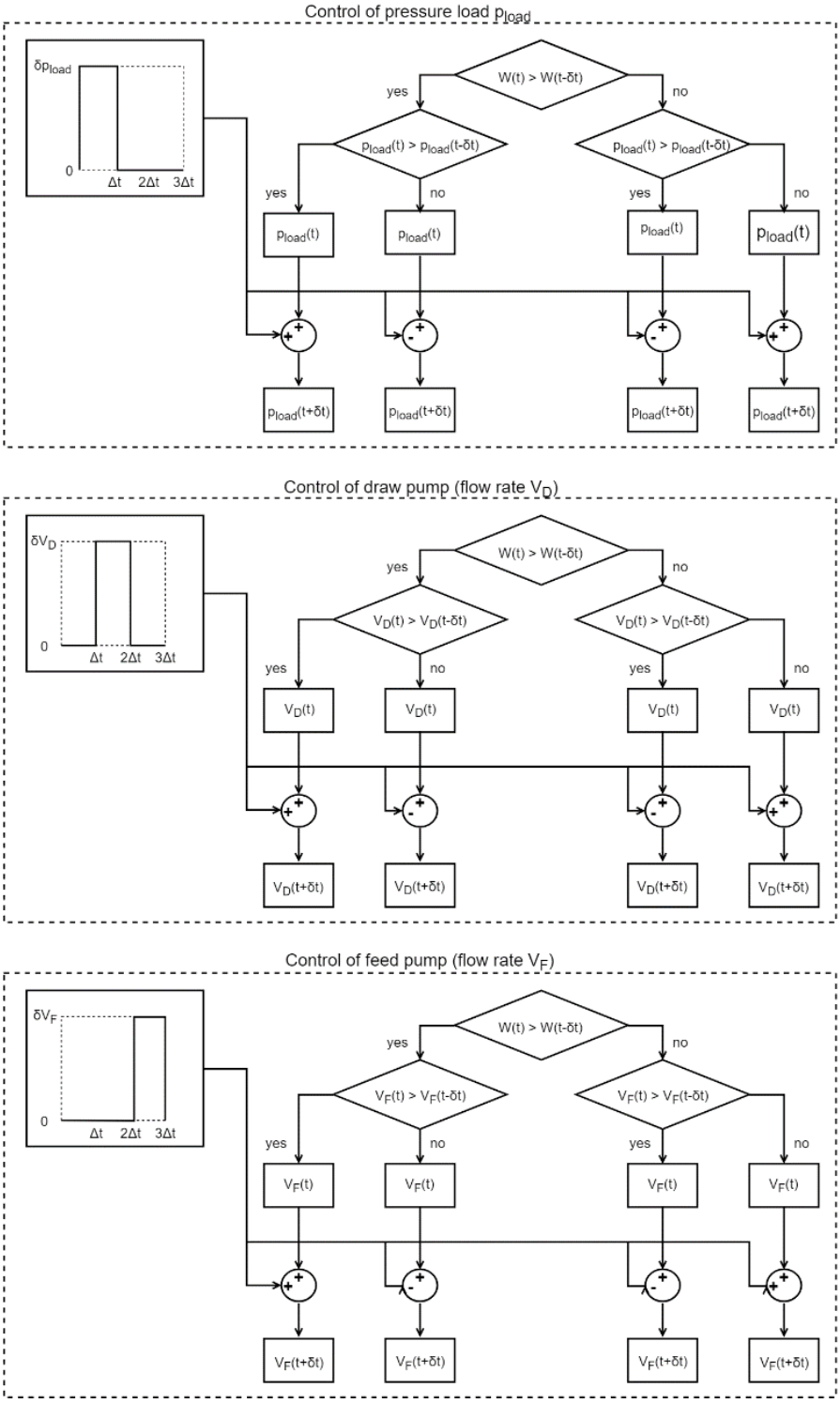

Figure 2.3 A perturb and observe control algorithm for real-time control of feed flow, draw flow, and load is capable of achieving maximum power point tracking in osmotic power systems.

2.3 Methodology

2.3.1 Modeling

The proposed MPPT strategy is implemented to control a PRO model, and the performance is demonstrated by simulation. The mathematical model has been previously described and validated [81,89] and is therefore only briefly reviewed here. This model describes differential transport dynamics of both water and salt, and the resulting interaction between hydro and chemical processes that produce a water permeate across the membrane.

As previously described in equation (2.3), water permeate is driven by the balance between the osmotic pressure difference $\Delta\pi$ and the applied pressure difference Δp across the membrane. In a finite element model each of these terms must be solved at each element. They are expressed in equations (2.5) and (2.6).

$$\Delta\pi = i\ R\ T\ \Delta c \tag{2.5}$$

$$\Delta p = p_D - p_F \tag{2.6}$$

Where i is number of ions in solute, R is the universal gas constant, T is the absolute temperature, and Δc is the concentration difference across the membrane. And where p_D and p_F are the hydraulic pressures at the draw and feed sides of the membrane.

Variations in hydrostatic pressure across the membrane surface are caused by friction. For the case of fully developed laminar flow in a spiral wound module, the Navier-Stokes equation shows that the pressure gradient in the direction of cross flow is,

$$\frac{dp}{dl} = -\dot{V}\ \frac{12\ \mu}{w\ h^3} \tag{2.7}$$

Where μ is the fluid viscosity, and w, l, and h, are the width, length, and depth of the flow channel. This is equivalent to the Darcy-Weisbach expression with friction factor of $f=96/Re$, which is the theoretical friction factor for fully developed laminar flow in a rectangular channel. Expressions for different flow regimes and geometries can also be derived but this simple case is used here to illustrate [93,94].

Variations in concentration across the membrane surface are caused by permeate mixing with the bulk solutions. This includes water permeate which leads to variations in feed and draw cross flow rates, as described in equations (2.8) and (2.9). It also includes salt permeate which diffuses through imperfect membranes, as described in equations (2.10) and (2.11).

$$\frac{d\dot{V}_D}{da} = J_w \tag{2.8}$$

$$\frac{d\dot{V}_F}{da} = -J_w \tag{2.9}$$

$$\frac{d\dot{m}_D}{da} = -J_s = -B\,\Delta c \tag{2.10}$$

$$\frac{d\dot{m}_F}{da} = J_s = B\,\Delta c \tag{2.11}$$

Where B is the membrane's permeability to salt, and where J_s is the mass permeate rate of salt, normalized over the membrane's surface area. Variations in the ratio of salt $\dot{m}$ to water $\dot{V}$ (i.e. concentration) are described by this set of differential equations.

In addition to mixing, accurate modeling of concentration across the membrane requires consideration for the boundary layers that develop at membrane surfaces, and

within the membrane substructure, a phenomenon referred to as polarization. The result is the formation of a concentration gradient normal to the membrane surface, which establishes the concentration difference across the membrane Δc. Polarization can be modeled with the solution-diffusion equation, which suggests that salt flux is the difference between diffusive and convective salt transport.

$$J_s = D\,\frac{dc}{dy} - J_w \tag{2.12}$$

In this expression, D is the diffusion coefficient, and y is the direction normal to the membrane surface.

2.3.2 Simulation

The system of equations together are the basis for a mathematical model which can be implemented and solved via several approaches. In this paper, we describe a relatively novel approach which we have previously proposed and validated [95,96]. This approach uses an equivalent circuit with lumped parameters representing finite elements of water volume and salt mass. The equivalent circuit model is shown in Figure 2.4.

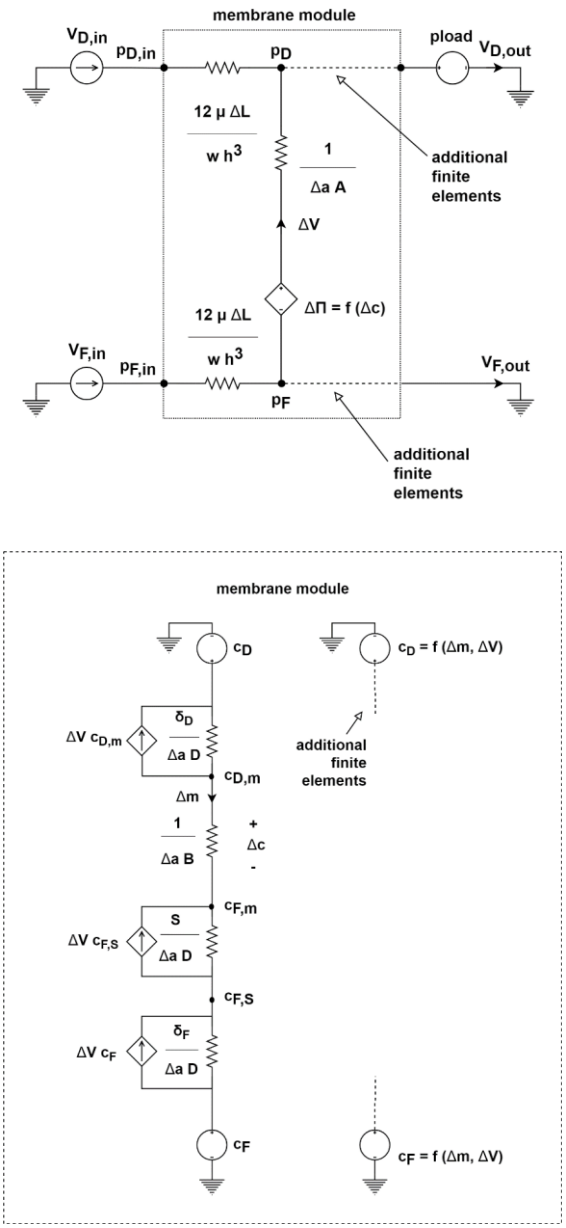

Figure 2.4 Lumped element equivalent circuit model of osmotic power system showing water transport (top), and salt transport (bottom) across a semi-permeable membrane.

This model includes two separate domains. The first uses current to represent water transport across membrane resistance and cross-flow resistances in the module, as shown in in Figure 2.4(a). Transport in this domain is driven by pressure which is analog to

voltage in an electric circuit. The second domain shown in Figure 2.4(b), uses current to represent the transport of salt across the membrane resistance, and across polarization layers. Diffusion in this domain is driven by concentration which is analog to voltage.

The model can be easily implemented with any circuit simulation software. In this case the circuit is implemented in Matlab Simulink software with 10 lumped elements. This level of resolution has been shown to be satisfactory, although of course, accuracy improves as the number of finite elements increases [96]. Simulation parameters are listed in Table 2.1. Module dimensions are selected based on reasonable values for commercial spiral-wound modules [96].

External boundary layer thickness is calculated as a function of the Sherwood number Sh,

$$\delta = \frac{d_h}{Sh} \tag{2.13}$$

Where d_h is the hydraulic diameter of the cross-flow channel. The Sherwood number is a function of the Reynold's number and the Schmidt number, and appropriate correlations are provided in [81].

Table 2.1 Simulation parameters.

Membrane Parameters			
	Porifera FO [81]	HTI TFC [97]	HTI CTA [97]
Water permeability, A ($l/m^2 \cdot h \cdot bar$)	4.21	1.63	0.51
Salt permeability, B ($l/m^2 \cdot h$)	1.43	1.42	2.19
Structure parameter, S (μm)	267	295	600

Table 2.1 —Continued

Module Dimensions	
Width, w	50 m
Length, l	1.5 m
Depth, h	0.5 mm
Boundary Layers	
Feed side thickness, δ_F	calculated at each finite element using eq. (2.13)
Draw side thickness, δ_D	calculated at each finite element using eq. (2.13)
Diffusion coefficient, D	1.5×10^{-9} m^2/s
Source Parameters	
Temperature, T	293 K
River water, c	0.1 g/l
Brackish water, c	1 g/l
Seawater, c	30 g/l
Reverse osmosis brine, c	55 g/l

2.4 Results and Discussion

2.4.1 Obtaining Maximum Power from Stand-alone PRO

The MPPT control system is demonstrated for the case of a stand-alone osmotic power system using seawater and river water [98–101]. Figure 2.5 shows the results for three commercial membranes listed in Table 2.1 and suggests that the MPPT controller effectively operates in real-time to track the maximum power point condition of the PRO system. An increase in net power output is observed as load and flow rates are adjusted

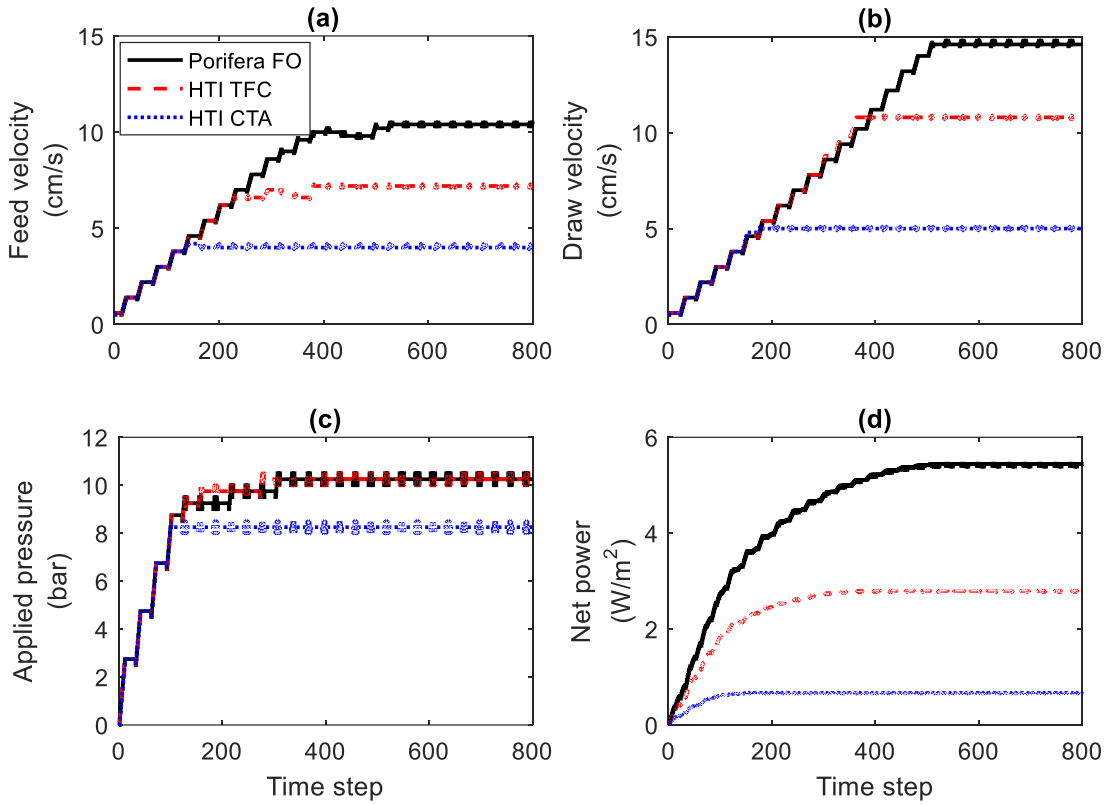

Figure 2.5 Real-time control of operating parameters (a) inlet feed velocity, (b) inlet draw velocity, and (c) load pressure, and the resulting effect which these have on (d) net power output. Results are shown for the case of stand-alone PRO with seawater draw solution and river water feed solution, with three different commercially available membranes. See Table 2.1 for simulation details.

from a start-up condition to their preferred positions. After between 200 and 500 time steps the system settles around the maximum power point. A time step is defined here as the desired sampling and control correction interval. After this time, the control variable oscillates around the preferred condition in a repetitive sequence of error and correction. Reducing this error can be done by reducing the magnitude of perturbations to the control variables, but this also increases the number of time steps required to achieve steady state operation [65,66]. Net power densities of 5.4 W/m^2 for Porifera, 2.8 W/m^2 for HTI TFC, and 0.7 W/m^2 for HTI CTA are shown here.

Figure 2.6 provides a closer view of the step changes applied to the pressure, feed flow, and draw flow for the case of the Porifera membrane. As illustrated, each of the control variables are varied in turn using incremental steps over a given time interval, and then held constant while the next control variable is adjusted, and so on in iteration. At steady state, oscillation around the preferred operating condition is also shown.

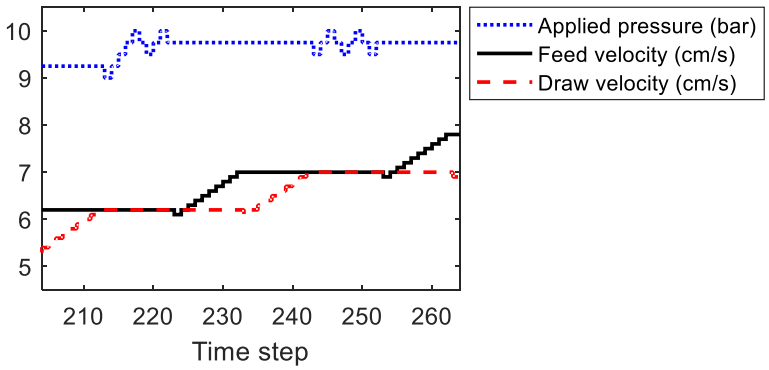

Figure 2.6 Detailed view of same case as Figure 2.5, showing step changes in applied pressure, feed velocity, and draw velocity using the iterative MPPT control cycle.

These results provide interesting insight into PRO dynamics and several general trends are observed. Figure 2.5 illustrates that preferred feed and draw flow rates differ from each other, with the former requiring between 4 and 10 cm/s, and the latter requiring higher flow between 5 and 15 cm/s. This is due to the tendency for external polarization to be more significant on the draw side. In fact, many polarization models altogether neglect the presence of feed side polarization [102]. Increasing velocity to promote mixing on the draw side therefore leas to a more significant improvement in permeate flux.

In addition, there is a pronounced difference in the feed and draw flow rates that are preferred for different membranes. In general, membranes with higher permeability tend to require higher flow. This is likely because the benefits of reducing polarization and dilution are much more pronounced in higher flux membranes.

Interestingly, the applied pressure settles at about the same point (~ 10 bar) for both the Porifera and HTI TFC membranes, while reaching a lower point (~ 8 bar) for the HTI CTA membrane. We hypothesize that the main driver here is the important difference in reverse salt permeability and structure parameter that leads to more important polarization in the case of the HTI CTA membrane. The bulk osmotic pressure difference between seawater and river water is approximately 25 bar, so in all cases the applied pressure is less than half. But in the case of the HTI CTA membrane, the applied pressure is further reduced by the lower effective concentration difference that occurs from more severe polarization.

It is useful also to consider the dimensionless expression of these operating conditions as shown in Figure 2.7. The ratio of permeate volume to feed volume suggests that less than 20 % recovery of the feed is desirable for maximum power production. This is significantly less than the recovery rates typically associated with other osmotic processes. While advantageous for power production, such low recovery rates will produce low specific energy results as discussed further on, and therefore might be reconsidered to place additional value on source volumes.

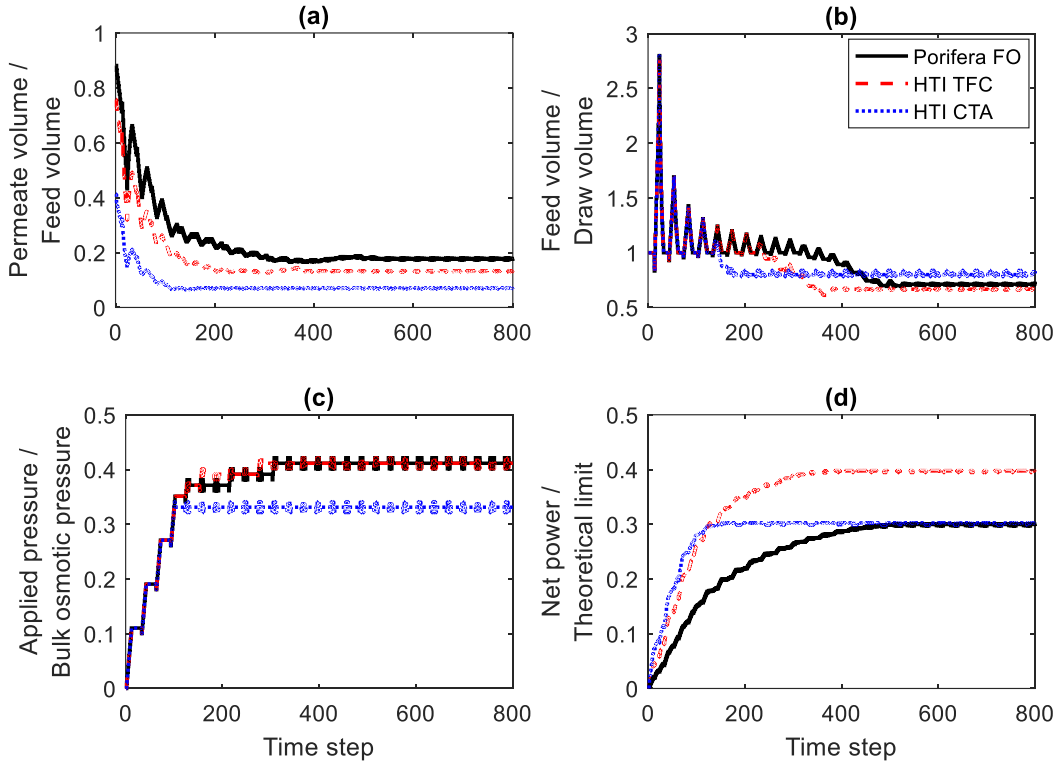

Figure 2.7 Dimensionless expressions of flow (a and b) and pressure (c), and their effect on power output (d). Results are shown for the case of stand-alone PRO with seawater draw solution and river water feed solution, with three different commercially available membranes. See Table 2.1 for simulation details.

We also compare performance of this system against a default reference. A wide range of operating parameters for flow rates and applied pressures have been proposed in the literature owing again to the highly case-specific nature of optimizing performance [66,82,84,100,103–106]. For reference we compare performance against default operation with cross flow velocities of 5 cm/s and with applied pressure equal to half the osmotic, which are common in the literature [81,82]. Figure 2.8 shows the steady state

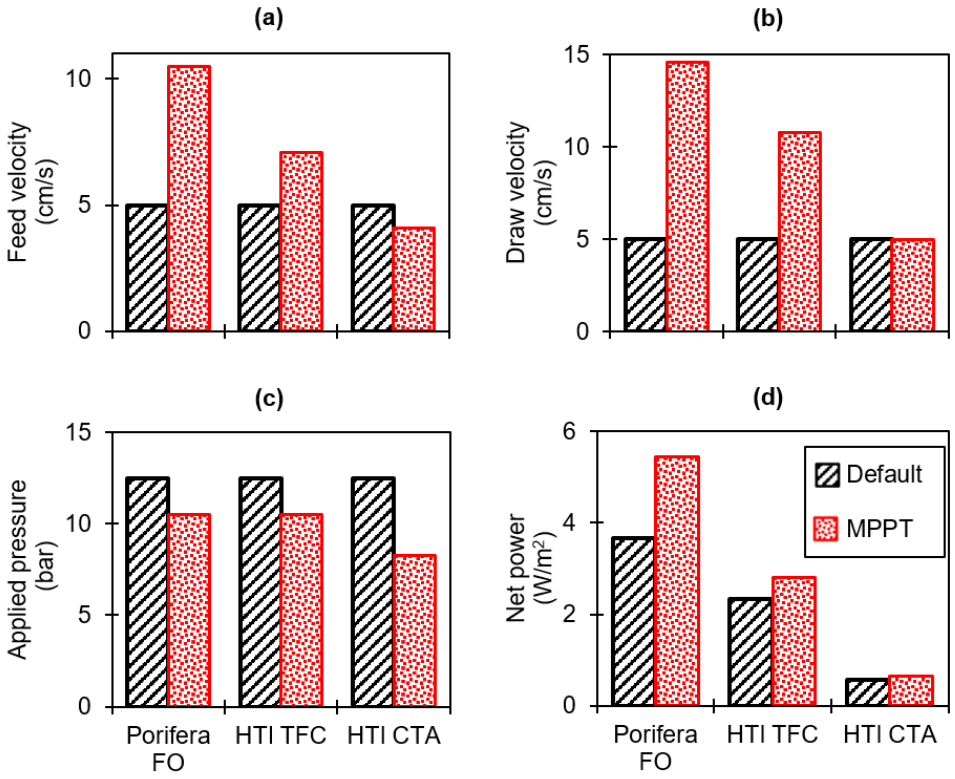

Figure 2.8 Steady-state operating parameters obtained when MPPT controller is implemented for stand-alone PRO, as compared to operation with default conditions suggested in the literature. See Table 2.1 for simulation details.

performance of the two cases and demonstrates higher net power of as much as 50 % when MPPT is used. Additionally, this figure demonstrates only steady state performance. Under variable conditions, the proposed controller allows for real-time adjustment which is not possible with operation at fixed default conditions.

The non-dimensional ratios for both the default and MPPT systems are also compared in Figure 2.9. Interestingly, the MPPT system not only produces higher power, but also.

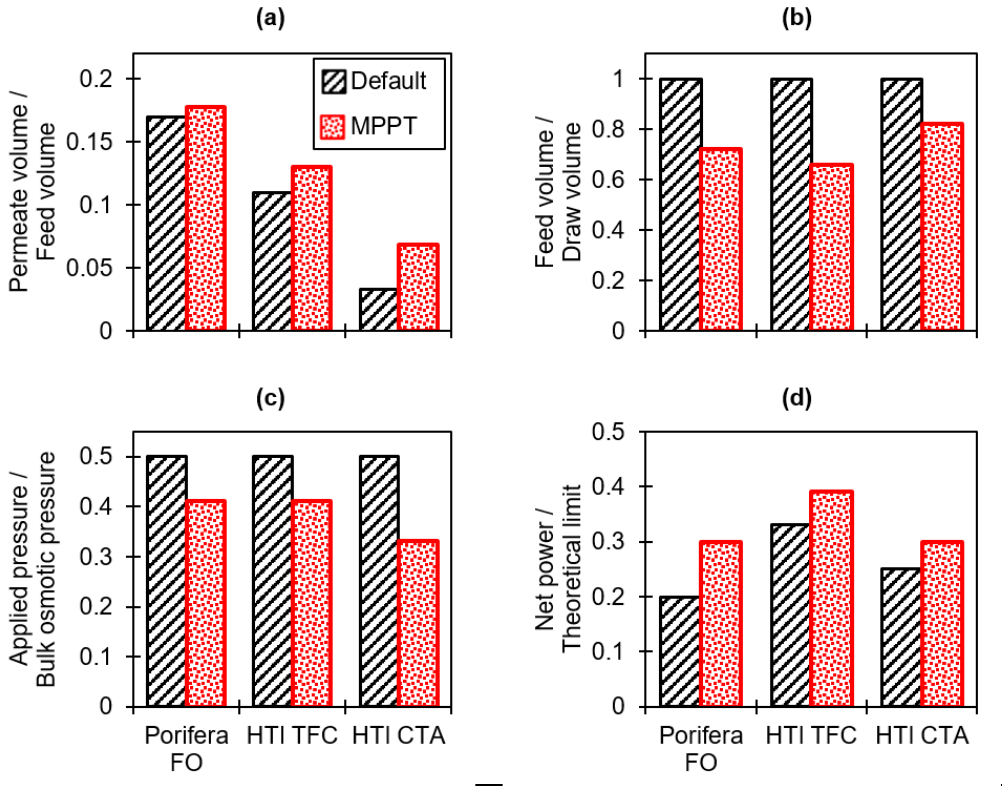

Figure 2.9 Dimensionless expressions for flow (a and b), pressure (c), and power (d) obtained at steady-state when MPPT controller is implemented for stand-alone PRO, as compared to operation with default conditions suggested in the literature. See Table 2.1 for simulation details.

does so at higher feed recovery ratios, suggesting that specific energy may in fact be increased.

2.4.2 Fouling Mitigation in Real Time

The previous results clearly illustrate that best operating conditions are unique and specific to membrane type, and we reasonably assume also unique to other conditions such as module geometry, environmental conditions, etc. Although general trends are observed, a practical PRO system with the target of achieving high power therefore requires optimization of operating conditions. Until now, most efforts to do so have

involved design stage modeling and optimization [107–111]. While this approach is necessary, its usefulness is limited by the accuracy of the modeling tools, and also by the inability to anticipate conditions in the field which vary with time and therefore require response. Real-time control and adjustment of operating conditions therefore offers significant advantages for dealing with such challenges, and should likely be implemented in addition to design stage optimization efforts. To illustrate, consider the effect that fouling has on membrane permeability [107–111], and how an MPPT controller can be used for real-time mitigation of the negative impact this has on power production.

Figure 2.10 shows the signal that is input to the model to simulate the drop in the permeability that occurs due to fouling. The profile is based on experimental results previously reported by Yip and Elimelech [107]. Overall, a drop of about 60 % of permeability occurs, after which membrane cleaning is performed and about 80 % of original permeability is recovered.

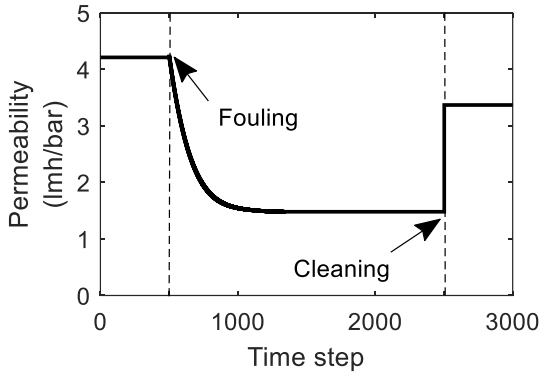

Figure 2.10 Drop in permeability over time that occurs due to fouling, followed by recovery of permeability due to membrane cleaning and maintenance.

The steady state performance of the MPPT controller is first compared to the default case given permeability at the three different stages of the fouling process. Figure 2.11 shows that significantly higher power is achieved during all of pre-fouling, fouling, and post-cleaning. The MPPT is shown to settle at the unique conditions that are preferred for each stage of the process and thereby achieve maximum power throughout.

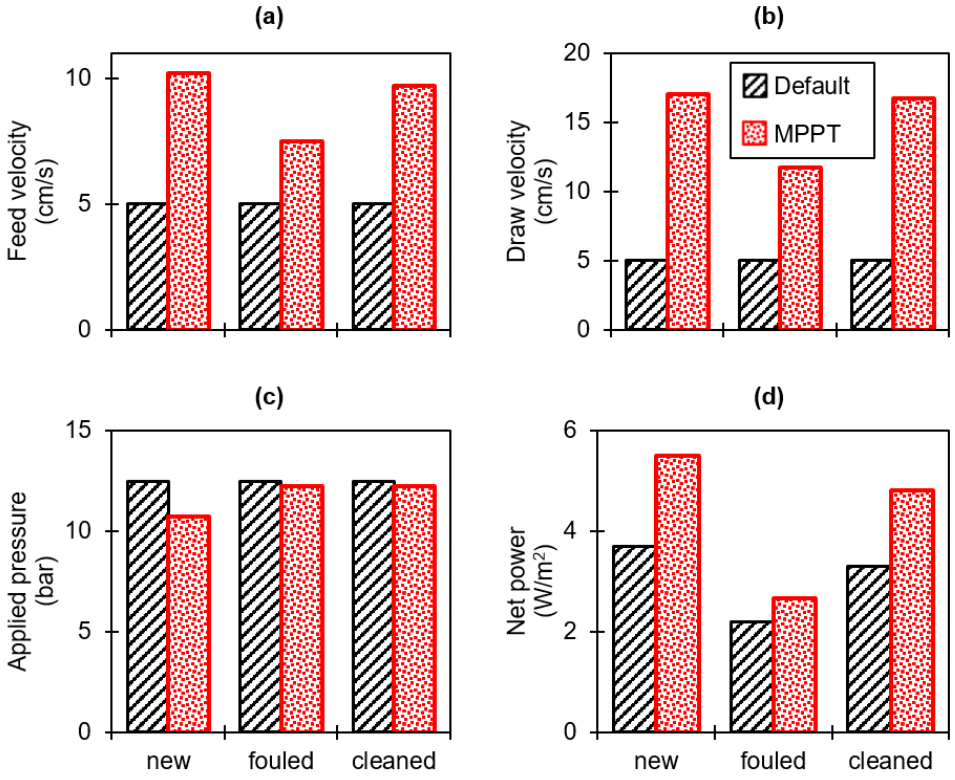

Figure 2.11 Steady-state operation achieved from MPPT control in response to various stages of fouling process in stand-alone PRO. Results of MPPT operation are compared against fixed operation at default parameters. See Table 4.1 for simulation details.

Figure 2.12 shows the operation of the controller in real-time, and compares performance against the case where the system has been optimized at the design stage but then fixed at those conditions throughout operation. Prior to fouling, the system

performance is very similar and only a slight improvement in power output is made by the controller as it adjusts to slight inaccuracies in the modeled optimization, for example. However, as fouling occurs and membrane permeability is compromised, a more important difference emerges between the two cases, finally settling at higher power of more than 20 % for the case with real-time control. After cleaning, as permeability is re-established, performance of the two cases again approaches one another. Importantly, in other cases where the design optimization is less accurate, the difference between the two systems would be more pronounced, as previously illustrated with steady state results in Figure 2.12. Membrane fouling is expected to be the most

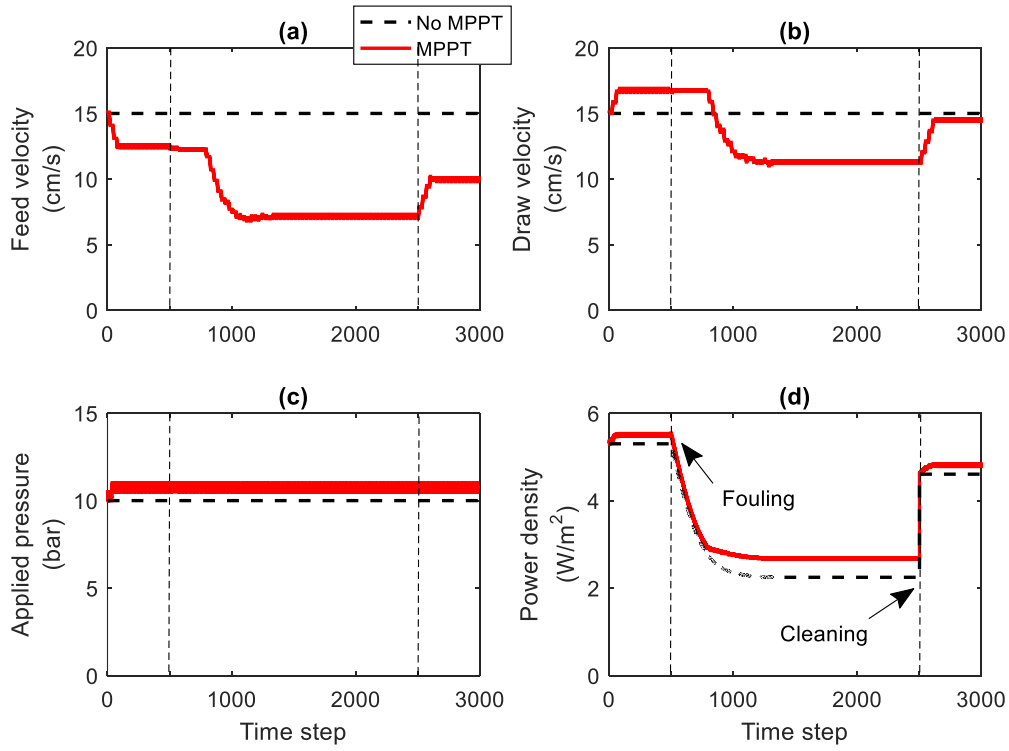

Figure 2.12 Real-time MPPT control in response to drop in membrane permeability from fouling. (a) Feed velocity, (b) draw velocity, (c) load pressure, and (d) net power density. This is shown for the case of stand-alone PRO using seawater and river water, and a Porifera membrane. Other simulation parameters are summarized in Table 2.1.

dynamic variable in a PRO system, however other variations in source concentration, temperature, and pump efficiencies for example can also be mitigated by real-time control.

2.4.3 Obtaining Maximum Power from RO-PRO

The MPPT controller can be used for a variety of PRO applications in addition to stand-alone power from seawater draw solution. This includes for recovering energy from concentrated brine that is rejected from RO desalination plants, a configuration referred to as RO-PRO [58,77,112–117]. Mixing this effluent with waste brackish water has been proposed and offers very large power densities. Figure 2.13 shows the results for the three commercial membranes and demonstrates the increase in power that is obtained by the MPPT controller relative to operation with default parameters. Power densities of 12.9 W/m^2 for the Porifera membrane, 7.9 W/m^2 for the HTI TFC, and 2.0 W/m^2 for the HTI CTA are obtained. These are up to twice as great as the power obtained with default conditions. Draw velocities are still higher than feed velocity, and they are both higher than the stand-alone PRO case. Here feed velocities reach between 6 and 15 cm/s, and draw velocities between 8 and 20 cm/s. These higher flow rates are a function of the larger driving force, which means that mitigating polarization and dilution effects with higher flow has a relatively larger benefit than in stand-alone PRO. In all three cases the applied pressure is less than half the bulk osmotic pressure difference which is about 45 bar.

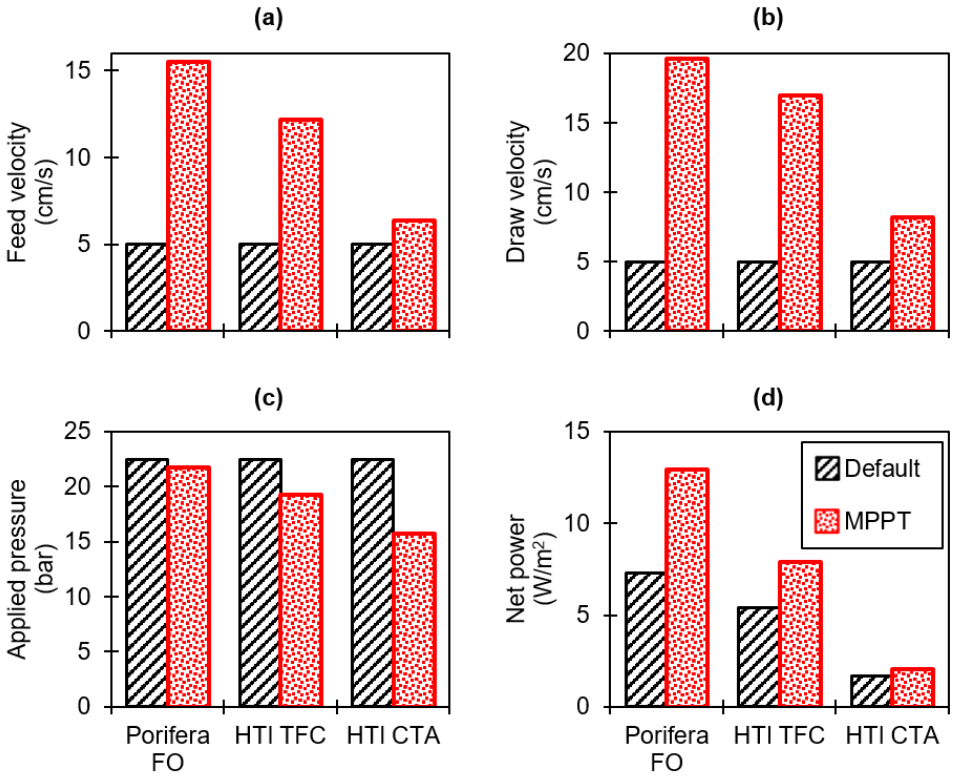

Figure 2.13 Steady-state operating parameters obtained when MPPT controller is implemented for RO-PRO, as compared to operation with default conditions suggested in the literature. See Table 2.1 for simulation details.

2.4.4 Obtaining Positive Net Energy

While obtaining sufficient power levels is essential to the viability of PRO power, recent publications have raised doubts about whether the balance between energy-in and energy-out is positive [104,115,116]. Figure 2.14 shows again the net power output for the stand-alone case previously examined in Figure 2.5 and the RO-PRO case from Figure 2.13. Here however, specific energy is also shown, which is the ratio between net energy output and the feed volume supplied to the system $\dot{W} \; / \; \dot{V}_{Fin}$.

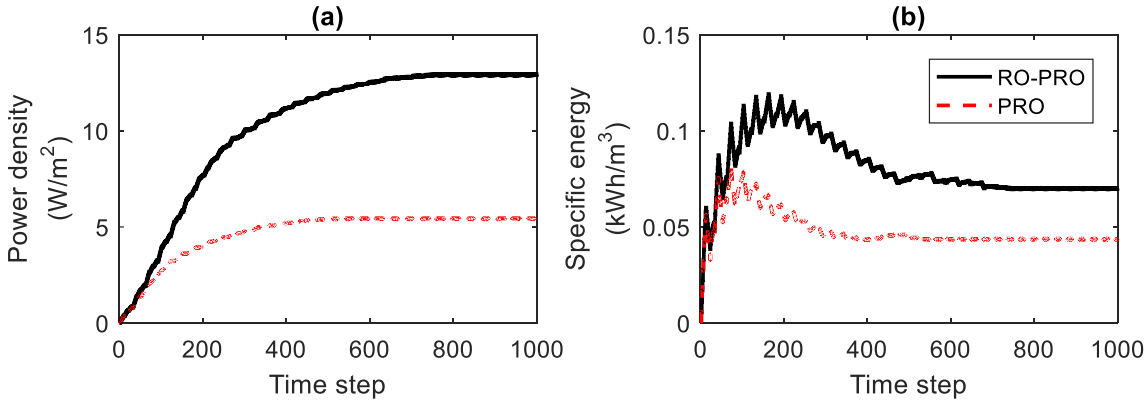

Figure 2.14 (a) Net power density and (b) specific energy $\dot{W} \; / \; \dot{V}_{Fin}$ obtained when a maximum power point tracking (MPPT) controller is used for cases of stand-alone PRO and combined RO-PRO. Porifera membrane is used along with other parameters summarized in Table 2.1.

The theoretical energy available by mixing seawater and river water is 0.69 kWh/m^3, and 1.39 kWh/m^3 for mixing RO brine with brackish water. The specific energy obtained here is much less, with steady-state operation achieving only 0.04 kWh/m^3 for stand-alone PRO, and 0.07 kWh/m^3 for RO-PRO. This is largely due to low feed water recovery rates that the controller identifies during maximum power tracking. While it is encouraging that these results are positive, it is important to consider them in light of the simplifications that have been made to the model. Our model considers concentration polarization, axial variations, and head losses due to friction, however, a more accurate energy balance estimate should consider additional losses such as pre-treatment energy loads (0.1-0.4 kWh/m^3), energy for pumping source water (0.02-0.05 kWh/m^3), and electro-mechanical losses (0.01-0.05 kWh/m^3) [116]. Subtracting these additional losses from the energy densities in Figure 2.14 leads to a negative energy balance.

Interestingly however, Figure 2.14 illustrates that maximum energy density does not occur under the same conditions as maximum power. In the case shown, net energy density appears to be greater at some intermediate step, and then drops as the control system moves towards the maximum power point. This tradeoff between energy and power has previously been analyzed [98,115,116,118,119]. It may therefore be advantageous to develop a control system that seeks to maximize net specific energy.

A maximum energy point tracking (MEPT) system is proposed here, and the performance of that controller is shown in Figure 2.15. The two cases of stand-alone PRO, and RO-PRO are again shown and can be compared to the previous results from Figure 2.11. As shown, the system achieves more than four times greater specific energy, with 0.16 kWh/m^3 for stand-alone PRO, and 0.30 kWh/m^3 for RO-PRO. If additional losses can be kept to the lower end of the previous estimates than positive energy output is possible. However, an additional challenge is that these higher energy levels have been obtained by reducing inlet flow rates, thereby accepting increased polarization and dilution, and ultimately sacrificing power. Power densities of only about 1 and 3.5 W/m^2 are obtained here for the stand-alone PRO, and RO-PRO cases respectively. These fall below the benchmark of 5 W/m^2 that is sometimes suggested for viability.

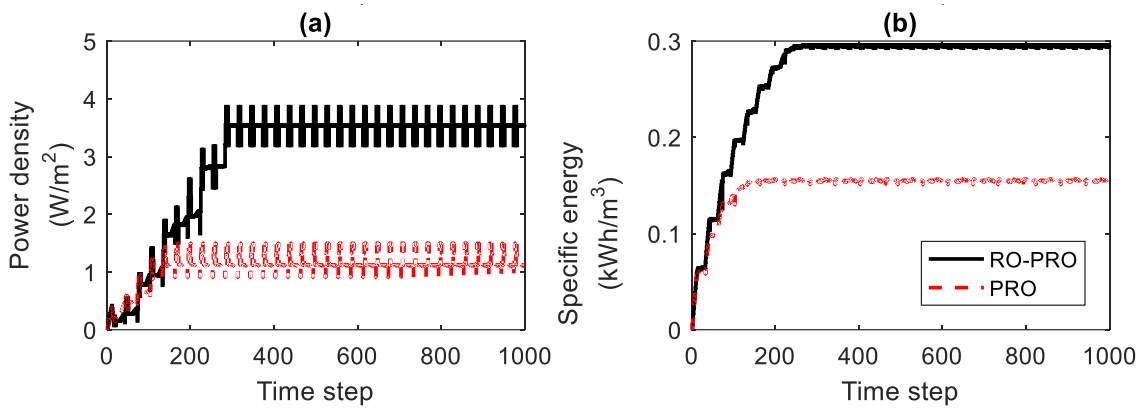

Figure 2.15 (a) Net power density and (b) specific energy $\dot{W} \ / \ \dot{V}_{Fin}$ when a maximum energy point tracking (MEPT) controller is used for cases of stand-alone PRO and combined RO-PRO. Porifera membrane is used along with other parameters summarized in Table 2.1.

2.5 Conclusions

This paper addresses the influence that operating conditions have on net power and how a particular set of operating conditions can help balance non-ideal factors and improve PRO performance. A feedback controller is introduced for the coordinated control of feed and draw pump speeds, and loading. A simple perturb and observe (P&O) algorithm is implemented here and used for both maximum power point tracking (MPPT) and maximum specific energy tracking. A mathematical model is described and used to simulate the performance of the controller given various membranes and scenarios. In general, the controller shows satisfactory behavior, settling at the target conditions and showing significant improvements relative to other rule of thumb operating conditions that have been used elsewhere in the literature. While the importance of selecting appropriate operating conditions for PRO has been previously discussed in the literature,

this is the first system that has been developed for real-time control of not only applied pressure, but also inlet flow rates.

The value of such a controller is illustrated by the wide range of feed and draw velocities that are obtained under different circumstances. Membrane properties are shown to have a significant effect on the best power conditions. For highly permeable membranes, operating at high cross flow velocities is preferred. This is because reductions in external polarization and axial dilution are leveraged by increased flux. For thick membranes with large structure parameter, lower applied pressures are preferred, due in part to more severe internal polarization and the lower effective osmotic difference. In the case of stand-alone PRO with river water and seawater, the best inlet velocities ranged from 4 to 15 cm/s depending on membrane properties. For combined RO-PRO systems that use RO brine and brackish water, the best inlet velocities ranged from 6 to 20 cm/s. Feed recovery rates ranged from 10 to 20 % for MPPT operation, and the ratio of feed to draw volume was shown to be less than 1. Applied pressure in all cases was less than half the osmotic pressure difference.

Although these values provide some guidance about the best operating conditions, it is also clear that results are very case specific. Membrane properties, module geometry, source chemistry, equipment efficiencies, pre-treatment systems, and many other factors, will all influence and change the solution for either maximum power or energy operation. In addition, changes in system parameters with time for example due to fouling, require real-time adjustment and correction. To operate efficiently, a practical PRO system therefore requires a controller such as the one proposed here. While we suggest a simple P&O algorithm here, more sophisticated control algorithms are also possible, and have

been widely adopted for a range of applications, for example for wind and solar power systems. Such controllers may also have applications to other osmotic processes which merits further investigation.

The tradeoff between high power production and energy production was clearly demonstrated in this paper. In the case of stand-alone PRO two different scenarios were illustrated, one for maximum power which achieved 5.4 W/m^2 but only 0.04 kWh/m^3, and a second for maximum energy which achieved 0.16 kWh/m^3 but only 1.0 W/m^2. In the case of combined RO-PRO, maximum power operation obtained 12.9 W/m^2 and 0.07 kWh/m^3, while maximum energy operation obtained 3.5 W/m^2 and 0.30 kWh/m^3. This tradeoff suggests that while high power densities (i.e. $\dot{W} > 5$ W/m^2) can be successfully obtained by application of the proper operating conditions, osmotic power systems still must overcome the hurdle of low specific energy densities in order to be a viable technology. This is especially true in light of estimates that suggest pre-treatment, source pumping, and other losses may require as much as 0.1 to 0.5 kWh/m^3 [116]. Over the past decade much research and development related to PRO has focused on membrane development for improved power density, and the result has been a steady improvement in power densities reported in the literature. It is hoped that similar efforts in pre-treatment, fouling mitigation, and process optimization will allow for positive net specific energies to be obtained while maintaining commercially competitive production rates.

2.6 Nomenclature

A	membrane water permeability ($m\ s^{-1}\ Pa^{-1}$)
a	membrane surface area (m^2)
B	membrane salt permeability ($m\ s^{-1}$)

c	concentration (g l^{-1})
D	diffusion coefficent (m s^{-2})
d	depth (m)
d_h	hydraulic diameter (m)
J_s	solute permeate flux (kg s^{-1} m^{-2})
J_w	solvent permeate flux (m^3 s^{-1} m^{-2})
l	length (m)
$\dot{m}$	mass flow rate (kg s^{-1})
p	pressure (Pa)
S	effective support layer thickness or structure parameter (m)
Sh	Sherwood number
R	gas constant (J mol^{-1} K^{-1})
T	absolute temperature (K)
t	time (s)
u	velocity (m s^{-1})
$\dot{V}$	volumetric flow rate (m^3 s^{-1})
$\dot{W}$	net power (W)
w	width (m)
y	direction normal to membrane surface

Greek symbols:

π	osmotic pressure (Pa)
δ	boundary layer thickness (m)
μ	viscosity

Subscripts:

D	draw
F	feed
p	permeate

CHAPTER THREE
DEMONSTRATION OF A REAL-TIME MAXIMUM POWER POINT TRACKER FOR SALT GRADIENT OSMOTIC POWER SYSTEMS

3.1 Introduction

The literature on maximum power point tracking (MPPT) for PRO so far includes several notable contributions. The application of MPPT to PRO power systems was first investigated by He et al. in 2015 [120]. In this work, In this work, the authors describe the importance of adjusting applied pressure in order to maximize power output. To achieve this, they proposed implementation of (1) a perturb and observe algorithm, and (2) an incremental mass resistance algorithm. In the first case, applied pressure is perturbed, the resulting effect on power is observed, and then applied pressure is iterated accordingly. In the second case, power is differentiated with respect to applied pressure in search of a zero peak, and then applied pressure is adjusted accordingly. Using these methods, maximum power of 2.5 W/m^2 and 3.8 W/m^2 were achieved with draw concentrations of 35 g/l and 55 g/l respectively. One notable limitation of this work was that it did not seek to optimize the operating feed and draw flow rates, which have a significant impact on power output. Also, the study was limited to only simulation, with the proposed MPPT algorithms being applied to a steady state PRO transport model.

As a follow up to this work, He et al. published in 2016 the results of two other MPPT algorithms for application to PRO [121]. These included (1) a mass feedback control algorithm, and (2) a fuzzy logic control algorithm. The first case is similar to the incremental mass resistance algorithm, wherein it seeks to minimize the derivative of power with respect to applied pressure, except that it also employs an adaptive gain in

proportion to the magnitude of the observed derivative. The second approach is also similar, except that it employs a series of predefined operator commands to steer the direction and magnitude of each perturbation. The advantage of these is that they vary the size of the perturbation applied to the pressure, starting initially with large steps to achieve rapid convergence, and then gradually reducing the perturbation size so as to minimize steady state energy losses. Results showed significant improvement in the MPPT performance but again, the scope of their work was limited to only optimization of the applied pressure, with no consideration for the operating flow rates. Also, the study was again limited to only simulation.

A third relevant study from the same group of M. H. Shaheen at the University of London was published in 2018 [122]. In this work, they proposed the application of a "whale optimization with differential evolution" method. This approach uses a fitness function derived from a PRO transport model to rapidly converge towards peak power. Using this approach, steady state maximum power was reached in ~ 1 s, much faster than the algorithms considered in previous work. In addition, the method showed stability around the maximum power point even under dynamic conditions, such as when concentration varied in real-time. Notably, the losses associated with feed and draw circulation were neglected, and therefore optimization of flow rates was not included in the methodology. And again, the proposed method was evaluated only with simulation using a PRO transport model.

Building on this prior work, our group at Oakland University published in 2019 the first PRO MPPT system that coordinated control of not only the applied pressure, but also the feed and draw circulation rates, as described in Chapter 2 [123]. Using a simple

perturb and observe algorithm applied in turn to each of the three control variables, maximum net power of up to 12.9 W/m^2 was achieved. Importantly, the analysis was limited to only simulation, applying the proposed MPPT system to a PRO transport model.

To date, there have been no attempts to implement a maximum power point tracking system on an actual PRO prototype. The scope of this study is to address this gap in the literature and to demonstrate the successful operation of a PRO MPPT system applied to an experimental laboratory test bench. A simple perturb and observe feedback algorithm is employed to control feed flow rates, draw flow rates, and applied pressure in a coordinated sequence. The transient response of the PRO system to step changes in operating conditions is characterized. Performance of the proposed MPPT system is demonstrated for PRO application to (1) energy recovery from desalination brine and (2) stand-alone power generation from seawater and river water.

3.2 Theory

3.2.1 Net Power from Pressure Retarded Osmosis

In a PRO power system work is extracted from the turbine as the product of permeate volume V_p and draw pressure $p_{D,out}$.

$$\dot{W}_{gross} = \dot{V}_p \, p_{D,out} \tag{3.1}$$

Where permeate volume is the difference between the volume at the inlet and outlet of the membrane, which must balance between both the feed and draw solutions (i.e. $V_p = V_{F,in} - V_{F,out} = V_{D,out} - V_{D,in}$), assuming incompressibility.

Work output from the turbine is considered "gross" because it does not account for parasitic loads that need to be supplied in order to operate the PRO cycle. These include the work input to the feed and draw pumps.

$$\dot{W}_F = \dot{V}_{F,in}\, p_{F,loss} \tag{3.2}$$

$$\dot{W}_D = \dot{V}_{D,in}\, p_{D,loss} \tag{3.3}$$

Where $\dot{V}_{F,in}$ and $\dot{V}_{D,in}$ are the feed and draw flow rates supplied to the membrane module, and $p_{F.loss}$ and $p_{D.loss}$ are the feed and draw pressure losses.

"Net" work is therefore the difference between the gross work output from the turbine and the work input to the pumps.

$$\dot{W}_{net} = \dot{W}_{gross} - \dot{W}_F - \dot{W}_D \tag{3.4}$$

Figure 3.1 provides an illustration of all the inputs that are defined in the energy balance from equations (3.1)-(3.4), and where they occur on the PRO network.

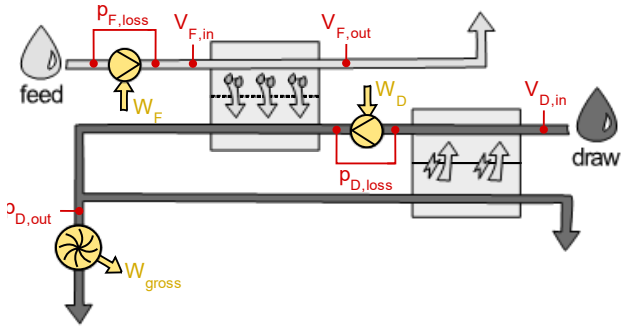

Figure 3.1 Net PRO power can be calculated from the difference of power output at the load ($W_{gross} = (V_{F,in} - V_{F,out})\, p_{D,out}$) and the power input to the feed pump ($W_F = V_{F,in}\, p_{F,loss}$) and to the draw pump ($W_D = V_{D,in}\, p_{D,loss}$).

3.2.2 Relationship Between Gross Power, Net Power, and Operating Conditions

Power output from PRO is sensitive to system operating conditions. Figure 3.2 illustrates the effect that circulating flow rates and applied pressure have on power and performance. As shown, increasing circulation rates of the feed and draw has a positive effect on water permeate rate and therefore gross power. This is because higher flow rates enhance mixing, reduce concentration polarization, and maintain more uniform bulk concentrations over the whole membrane surface. However, these benefits are accompanied by an increase in hydraulic pressure loss due to friction. Beyond a certain point the increase in gross power can be offset by the increased pumping power, and thereby lead to a reduction in net power.

Figure 3.2 also shows the tradeoff between applied pressure and water permeate that is a fundamental characteristic of PRO, as the two are inversely proportional. In an ideal simplified system, maximum power is achieved when applied pressure is half of the osmotic pressure difference [124]. In practice, however, non-ideal transport dynamics and inefficiencies throughout the system cause the maximum power point to occur at some other applied pressure.

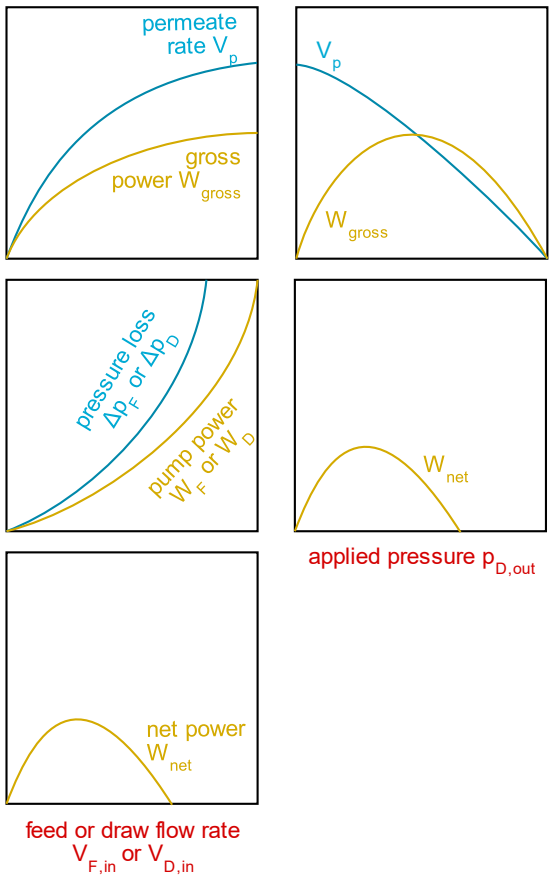

Figure 3.2 Effect that operating feed flow rate $\dot{V}_{D,in}$, draw flow rate $\dot{V}_{F,in}$, and applied pressure $p_{D,out}$ has on PRO power and performance. Plots are not to scale and are intended only to show general trends.

3.2.3 Real-Time Maximum Power Point Tracking

To maximize net power from the PRO system it is therefore necessary to carefully balance the operating conditions. In our previous work, we have shown that there is a unique combination of operating flow rates and applied pressure that will maximize net power output of a given PRO system [125]. While such theoretical analysis can be completed at the design stage, field conditions, material properties, and equipment efficiencies may vary in practice and with time. Therefore, a dynamic control system that

adjusts operating conditions in real-time is needed to ensure peak PRO performance. Figure 3.3 shows the basic feedback loop, whereby net power is tracked in real-time, and an appropriate algorithm is used to adjust input commands to the control points in order to track maximum net power.

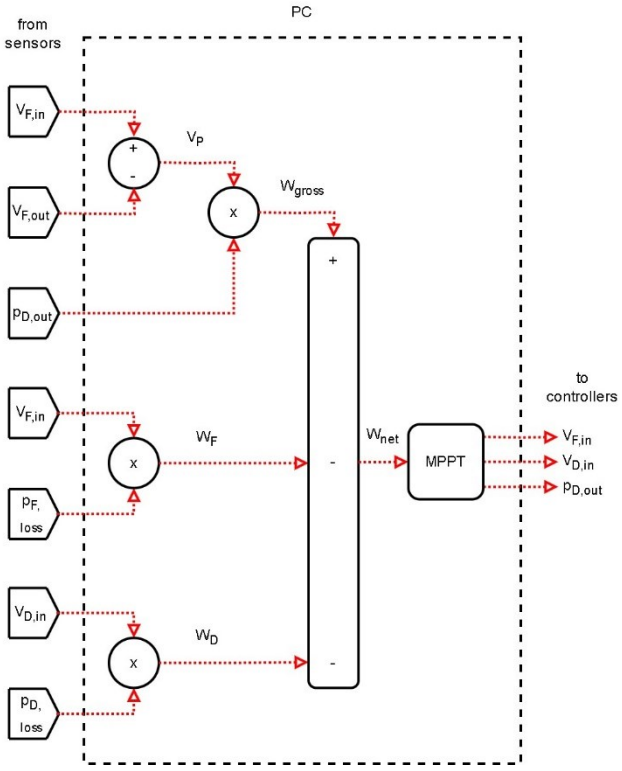

Figure 3.3 Feedback loop that evaluates net PRO power in real-time and uses a maximum power point tracker to adjust commands to the feed flow rate, draw flow rate, and applied pressure.

3.2.4 Perturb and Observe Control Algorithm

The concept of maximum power point tracking is well developed, such as for its application to photovoltaic solar panels, and a variety of algorithms have been proposed in the literature [126–129]. Perturb and observe (P&O) is one commonly used algorithm.

This algorithm works by perturbing (i.e. changing) the operating parameter of the system and then observing the resulting change in net power output. If the result is favorable, the algorithm further perturbs the operating parameter, but if the result is unfavorable, the change is reversed. Using this incremental approach, the algorithm gradually moves the system towards operation at its maximum power point. The basic logic is summarized in Figure 3.4. For this application, since PRO performance depends on several operating parameters, the P&O algorithm is applied iteratively to adjust the feed flow rate, draw flow rate, and applied pressure each in turn. The inherent disadvantages with this approach are that it can be slow to converge to the maximum power point, and once near, it will continue to oscillate, causing some energy loss. While other more sophisticated control algorithms can address these issues and improve performance, the simple P&O algorithm is sufficient for the scope of this study.

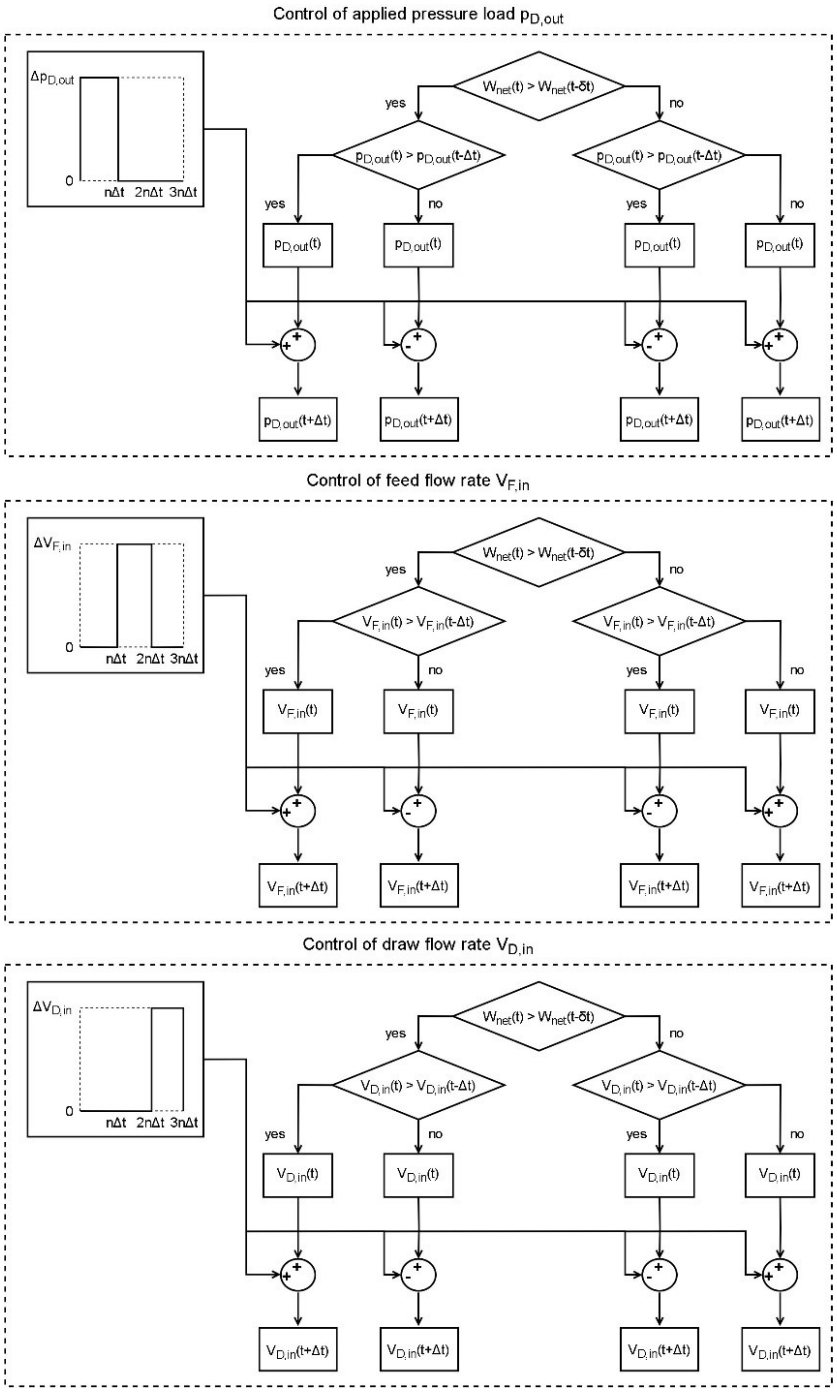

Figure 3.4 A perturb and observe algorithm for real-time control of feed flow rate, draw flow rate, and applied pressure is capable of operating PRO power systems near their maximum net power.

3.3 Materials and Methods

3.3.1 Laboratory Test Bench

To demonstrate operation and performance of the proposed MPPT a laboratory-scale PRO test bench was designed and built to verify the effectiveness of our MPPT control strategy. A visual of the laboratory system is provided in Figure 3.5. The bench consists of a 4-port flat-sheet membrane cell (CF042A, Sterlitech, Kent WA) that is supplied with feed and draw solutions from two variable speed pumps (GAF-T23-DE MSE, Micropump, Vancouver WA) that are controlled by mass flow controllers (KD100A-SCF-S0A-KA-2X and KF-F200A-SCF-S0A-KA-2X, Alicat Scientific, Tucson AZ). A mass flow meter mounted at the feed outlet (KD100A-SCF-S0A-KA-2X, Alicat Scientific, Tucson AZ) is used to establish a mass balance between flow in and out and thereby determine water permeate rates. Pressure applied to the draw solution is controlled by a pressure controller (PCS-100PSIG-D-PCA17/5P, Alicat Scientific, Tucson AZ) positioned at the draw outlet. Pressure losses along channels on both sides of the membrane are measured by differential pressure sensors (PS-30PSID-D/5P, Alicat Scientific, Tucson AZ). Table 3.1 provides a list of all instrumentation with key specifications.

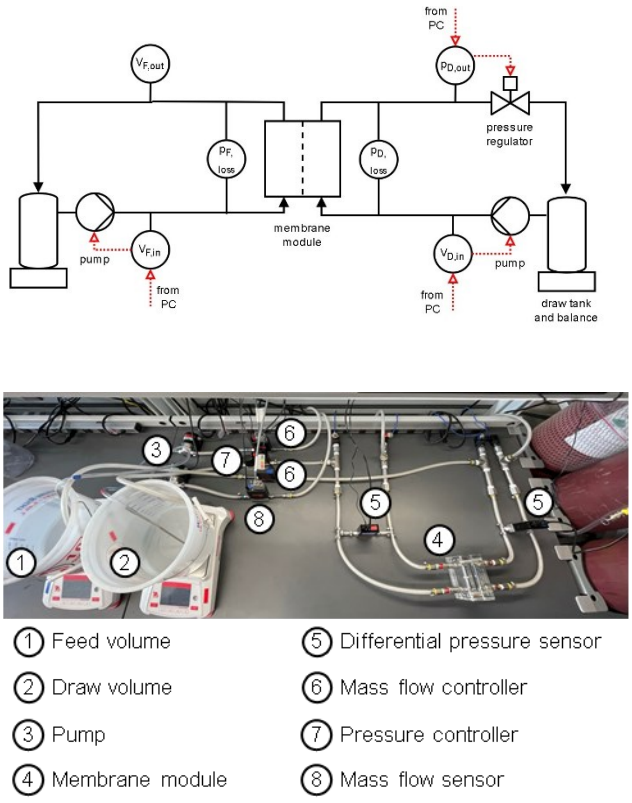

Figure 3.5 Laboratory scale PRO test bench at Oakland University.

Table 3.1 Instrumentation list and specifications.

Instrument	Supplier	Model #	Full Scale ± Uncertainty
Feed mass flow controller	Alicat Scientific (Tucson, AZ)	KD100A-SCF-S0A-KA-2X	1 kg/h ± greater of 0.2 % full scale or 0.6 % reading
Draw mass flow controller	Alicat Scientific (Tucson, AZ)	KF-F200A-SCF-S0A-KA-2X	10 kg/h ± greater of 0.2 % full scale or 0.6 % reading
Mass flow meter	Alicat Scientific (Tucson, AZ)	KD100A-SCF-S0A-KA-2X	1 kg/h ± 0.2 % full scale or 0.6 % reading
Applied pressure controller	Alicat Scientific (Tucson, AZ)	PCS-100PSIG-D-PCA17/5P	21 bar ± 0.25 % full scale

Table 3.1 —Continued

Instrument	Supplier	Model #	Full Scale ± Uncertainty
Differential pressure sensor	Alicat Scientific (Tucson, AZ)	PS-30PSID-D/5P	1 bar ± 0.25 % full scale

3.3.2 Membrane Selection

A commercial cellulose triacetate membrane (FTS H2O, Albany OR) was selected for this study. Flat-sheet membrane coupons were mounted in the clear acrylic module accommodating samples with an effective surface area of 42 cm^2 (107 mm length × 39 mm width). Characteristic membrane properties including water permeability, salt permeability, and effective thickness for this membrane were experimentally evaluated in our previous work [130] and the results are reported in Table 3.2. To facilitate operation at the desired flow velocities and provide support to the membrane, shims were inserted into both the feed and draw channels reducing the effective depth to 0.801 mm. The feed channel was also equipped with a 31-mil diamond-shaped spacer to provide support when pressure is applied. A summary of the membrane module parameters is also provided in Table 3.2.

Table 3.2 Membrane and module parameters.

Membrane properties	
Supplier	FTS H2O (Albany, OR)
Material	cellulose triacetate
Configuration	flat sheet
Water permeability	0.42± 0.01 [130]

Table 3.2 —Continued

Salt permeability	0.40±0.05 [130]
Structure parameter	0.607±0.01 [130]
Module properties	
Configuration	flat-sheet
Dimensions	107 mm x 39 mm
Area	42 cm^2
Channel depth	0.801 mm
Feed channel spacer	31-mil diamond-shaped

3.3.3 MPPT Implementation

The proposed MPPT control system was implemented using a commercial software package (FlowVision v2, Alicat Scientific, Tucson, AZ) that was supplied by the flow controller and pressure controller manufacturer. The software was used to acquire data from the flow and pressure sensors, evaluate net power based on these measurements (as detailed in Section 3.2.1.), run the perturb and observe control algorithm to determine the next perturbation, and accordingly send the updated input signal to the mass flow controllers and pressure controller. Table 3.3 shows the perturbation size used for the feed flow rate, draw flow rate, and applied pressure, as well as the step interval. Initial operating conditions are also specified. To ensure the safety of the equipment, limits were placed on the control protocol such that feed flow rate, draw flow rate, and applied pressure could not exceed 1 kg/h, 10 kg/h, and 20 bar respectively (even if desired by the P&O logic).

Table 3.3 PRO control parameters

Perturb and observe parameters	
Feed flow perturbation $\Delta V_{F,in}$	0.1 kg/h
Draw flow perturbation $\Delta V_{D,in}$	0.25 kg/h
Applied pressure perturbation $\Delta p_{D,out}$	1 bar
Step interval Δt	600 s
Steps per cycle per operating parameter n	4
Initial operating conditions	
Feed flow rate	1 kg/h
Draw flow rate	5 kg/h
Applied pressure difference	9 bar

3.3.4 Data Analysis

Water permeate rate and net PRO power were experimentally evaluated in real-time as operating conditions were varied by the MPPT system. Analysis of raw data followed the same basic theory outlined previously in equations (3.1)-(3.4), but additional details are provided in Supplementary Note 3.1. Notably, water permeate rate and power are calculated using the moving average of sensor data over the given cycle in order to smooth signals and filter noise. Propagation of experimental uncertainty is also detailed in Supplementary Note 3.1.

3.3.5 Experimental Test Conditions

Extensive testing was conducted to evaluate performance of the MPPT system for PRO Extensive testing was conducted to evaluate performance of the MPPT system for PRO application to (1) energy recovery from RO brine, and (2) stand-alone power generation. In the first case, feed and draw concentrations of 0 and 70 g/l were used to

approximate the use of fresh water and desalination brine. In the second case, feed and draw concentration of 0 and 35 g/l were used. All solutions were prepared using sodium chloride NaCl (> 99% purity, Fisher Scientific, Hampton, NH) dissolved in deionized water. All testing was conducted at room temperature. A summary of test conditions is provided in Table 3.4.

Table 3.4 Experimental test conditions

Test Conditions	
Flow configuration	Counter flow
Feed concentration	DI water
Draw concentration	35 and 70 g/l
Temperature	20 °C

3.4 Results

3.4.1 Control of PRO Operating Conditions

Performance of the PRO system is maximized by careful control of the feed circulation rate, draw circulation rate, and applied load pressure. In the proposed system, these variables are controlled using mass flow controllers that operate by adjusting the pump speed, and a pressure controller that operates by adjusting a valve to the desired setpoint. Figure 3.6 shows the mass flow rate, draw flow rate, and applied pressure in response to a series of step commands sent to their respective controllers. In most cases, the observed data tracks the command signal well and any difference between the two is within the margin of experimental uncertainty. However, for the draw flow rate, a discrepancy beyond just the experimental uncertainty is observed between real-time measurements

and command input. This may be caused by feedback between the draw flow controller located at the membrane inlet and the draw pressure controller (i.e. load) located at the membrane outlet. This may also indicate the need to adjust PID tuning constants for draw flow controller.

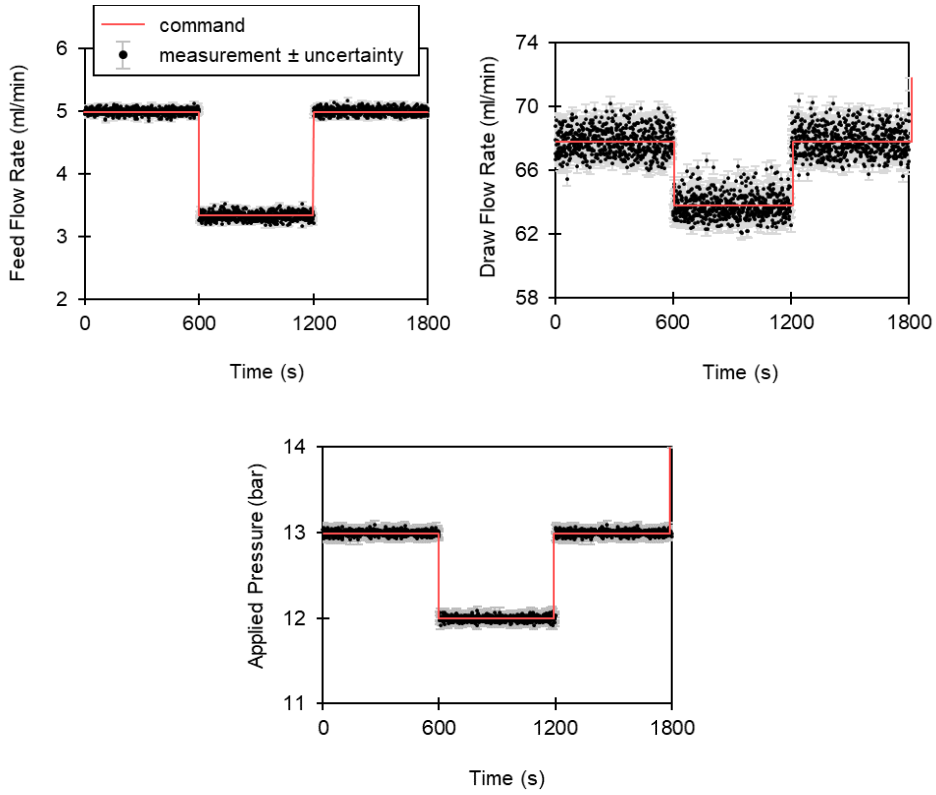

Figure 3.6 Experimentally observed PRO operating conditions in response to a series of step commands applied to their respective controllers.

3.4.2 Step Response of PRO System

Figure 3.7 shows the dynamic water permeate and output power of the PRO system in response to a series of step commands that are applied in turn to each of the three control variables. In some cases, the response is more pronounced than others, but this is a

function of the perturbation step size, and the characteristics of the PRO system, which will be more sensitive to operating conditions over certain particular ranges. In general, after a brief transient period of ~ 120 s, the system appears to settle to steady state. Steady state behavior agrees with the theoretical expectations. For example, an increase in the applied pressure leads necessarily to a drop in the water permeate flux (albeit a minor one), and in this particular case, the product of the two yields lower gross power and net power output. For the draw flow, an increase in the circulation rate led to a slight increase in the water permeate flux and as a result an increase in the gross power. The higher circulation rate however also increases pressure losses, such that in these cases the net power actually decreases (albeit only slightly). The effect of the feed flow rate is similar to that of the draw flow rate, although trends are reversed as the circulation rate is decreased here instead of increased.

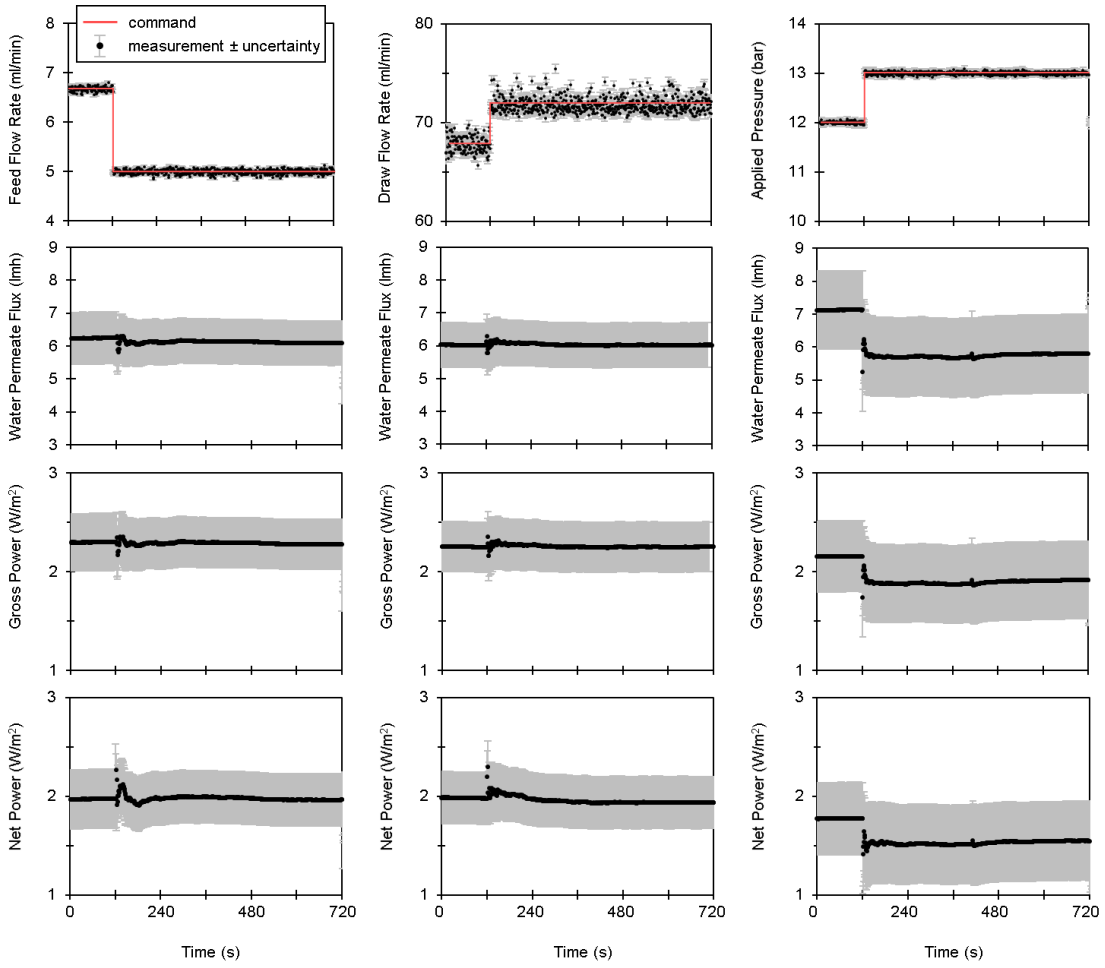

Figure 3.7 Real-time measurement of the water permeate flux, gross power density (average), and net power density (average) output of the PRO system in response to step changes in feed flow rate, draw flow rate, and applied pressure (from left to right)

3.4.3 Maximum Power Point Tracking

The PRO MPPT controller is demonstrated for the application of salt gradient energy recovery from reverse osmosis brine (cD = 70 g/l) in the presence of a low concentration wastewater feed source (cF ~ 0). Figure 3.8 shows the results and suggests that the MPPT controller effectively operates in real-time to maximize net power output by coordinating incremental adjustments in the feed flow rate, draw flow rate, and applied pressure.

For the first case representing energy recovery from RO, after approximately 18 steps of 600 s each (~ 10,800 s) the system settles near the maximum net power output of ~ 2 W/m^2. This is relatively low compared to power results published elsewhere in the literature [131–134], but this is because of our use of a low-cost commercially available cellulose-based membrane. More important in this context, is the significant improvement of net power output compared to the initial baseline power. In this case, we obtain more than 3× the initial baseline power of ~ 0.6 W/m^2. The operating conditions that yield this maximum power are feed flow rate $\dot{V}_F$ ~ 5 ml/min, draw flow rate $\dot{V}_D$ ~ 72 ml/min, and applied pressure Δp ~ 14 bar. In normalized terms, these flow rates translate to 0.26 cm/s and 4 cm/s respectively with a recovery ratio of 0.08. These particular values are specific to our PRO lab system and a unique maximum power solution can be expected for systems with different membranes, module dimensions, and feed and draw concentrations. However, in general, it can be expected that feed flow rates will be less than draw flow rates because pressure losses can be severe through the feed channel, since it is compressed against a spacer by the applied pressure. In addition external polarization is more significant on the draw side. Increasing circulation to promote mixing on the draw side therefore leads to a more significant improvement in permeate flux. In normalized terms, the applied pressure of 14 bar translates to ~ 24 % of the bulk osmotic pressure difference, much less than the value of 50 % that is typically suggested for PRO.

For the second case representing stand-alone power generation, the system settled near the maximum net power of ~ 0.2 W/m^2 again after approximately 18 steps or 10,800 s. In absolute terms this power is again quite underwhelming, which is mostly because of the

selection of a low flux membrane, however more significant is the relative improvement over baseline performance. In fact, in this case, net power under baseline conditions is actually negative and only becomes positive as the MPPT controller adjusts the PRO operation. The operating conditions that yield maximum net power are feed flow rate $\dot{V}_F$ ~ 6 ml/min, draw flow rate $\dot{V}_D$ ~ 64 ml/min, and applied pressure Δp ~ 7 bar. Again, these specific values are unique to the laboratory test bench with its particular specifications, dimensions, and efficiencies. But more generally, we observe that feed circulation rates will be less than draw circulation rates, and applied pressure will be less than half the bulk osmotic pressure. In relative terms, these flow rates translate to 0.32 cm/s and 3.4 cm/s respectively, and the applied pressure translates to ~ 24% of the bulk osmotic pressure difference.

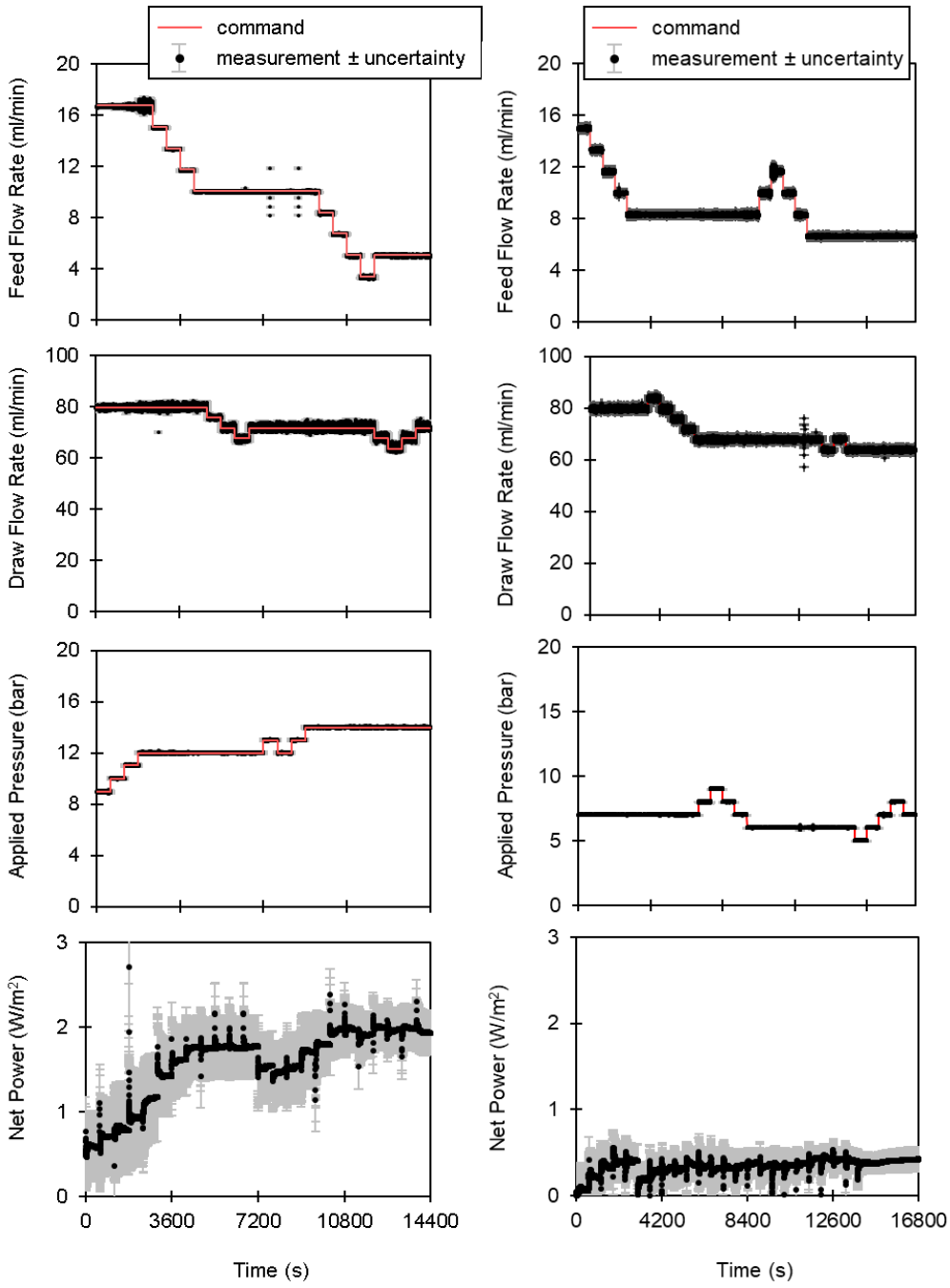

Figure 3.8 Demonstration of real time MPPT controller finding the feed flowrate, draw flowrate and applied pressure leading to maximum net power density of (a) a RO-PRO system (b) a PRO system with seawater as draw flow

3.4.4 Improving MPPT Performance

Although the MPPT controller successfully increased power output, several possible improvements can be considered to allow the system to converge more quickly and settle more closely to the maximum power point. Figure 3.9 shows the time that was required for net power to reach steady state during each of the MPPT steps shown previously. In the algorithm implemented in this study, steps were taken at intervals of 600 s in order to ensure that net power would settle to within 1 % of steady state. However, a much shorter interval between steps could reasonably be considered. For example, an interval of 60 s would result in net power settling to within 1 % of steady state at least 75 % of the time, and to within 5 % of steady state the rest of the time. Other more sophisticated strategies could also be considered, such as varying the interval to whatever time is needed to observe a change in net power that is less than some minimum threshold.

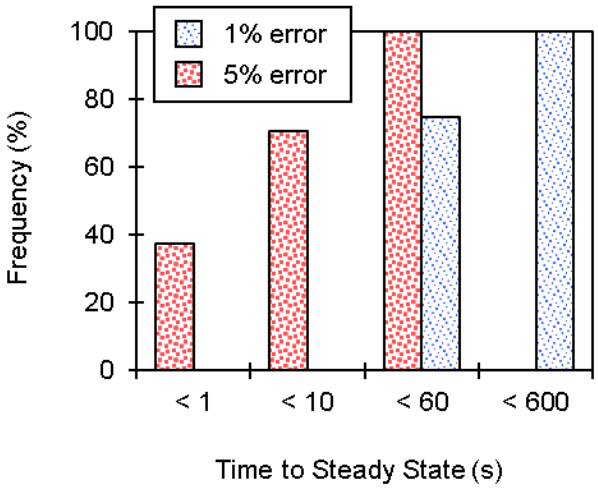

Figure 3.9 Comparing different step intervals which lead to steady state of the MPPT controller within 1% error and 5% error

In addition, smaller perturbation signals can be employed to allow the system to settle more closely to the maximum power point. In this study, constant perturbation signals of 1.7 ml/min, 4.3 ml/min, and 1 bar were applied to the feed flow controller, draw flow controller, and applied pressure controller. These represent respectively 34 %, 6 %, and 8 % of the final steady state operating conditions. Such large perturbations will prevent the system from converging very closely to the maximum power point. A variable perturbation size would be more appropriate, such as for example, perturbing the command signal by only 1 % of its value. Of course, smaller perturbations would increase the time needed to converge towards the maximum power point, but presumably this would be mitigated by the smaller step intervals suggested above. Additionally, smaller perturbations may also have a favorable reduction in the time to steady state.

3.5 Conclusions

In this study, the concept of maximum power point tracking is experimentally applied to a laboratory-scale pressure retarded osmosis power system in order to maximize net power output. This is achieved by the coordinated real-time control of the feed circulation rate, the draw circulation rate, and the applied load pressure using a perturb and observe feedback algorithm. Although maximum power point trackers have been proposed for osmotic power systems elsewhere in the literature [120–123,135], this is the first time that the concept has been experimentally demonstrated.

The system is shown to successfully increase net power in real-time. In the case where high concentration draw solution is used (representing application to RO-PRO energy recovery), net power of ~2 W/m^2 is achieved, an improvement of more than 3× the power observed under the initial baseline conditions. In the case where seawater draw solution is

used (to represent stand-alone PRO power generation), net power of ~0.2 W/m^2 is achieved, a significant improvement over the negative power observed under baseline conditions. Although absolute power results are underwhelming, the relative improvement nevertheless provides a clear demonstration of the MPPT utility.

The performance of the PRO system is shown to be sensitive to operating conditions and maximum power is achieved for a particular combination of flow rates and applied pressures. For the cases studied, feed and draw circulation rates between 5-6 ml/min and 64-72 ml/min respectively were preferred, together with applied pressures between 7-14 bar. These particular values are highly case specific and unique to the laboratory test conditions. Factors such as membrane properties, module geometry, source chemistry, equipment efficiencies, and pre-treatment systems will all influence the maximum power point and its corresponding operating conditions. However, certain trends observed here can be extended to PRO operation more generally. (1) Draw circulation rates should be greater than feed circulation rates – higher draw flow rates will help to mitigate concentration polarization that is more severe in the draw solution, and lower feed flow rates will help to minimize pressure losses that can be more severe in the compressed feed channel. (2) Applied pressure should be less than half the osmotic pressure difference. And (3), higher flow rates and higher applied pressures will be energetically justified in high power applications, such as cases that have large concentration gradients. For the purpose of experimentally demonstrating PRO MPPT for the first time, a simple perturb and observe algorithm was employed in this study. However, there is certainly much room for improvement. The literature regarding MPPT is well developed such as for application to solar photovoltaics, and much can be learned for application to PRO.

More sophisticated algorithms can be employed to allow the system to converge more quickly and settle more closely to the maximum power point. At a minimum, we suggest reducing the time interval between steps to increase the controller speed. From our analysis, it appears that the PRO time constant is on the order of 60 s, but further testing is required to confirm, especially in response to perturbations of different sizes. We also suggest reducing the perturbation size to reduce steady state energy losses. With continued research and development, the PRO MPPT concept can be refined and contribute to more efficient salt gradient energy conversion systems for a variety of water/energy applications.

3.6 Nomenclature

n	number of time intervals
p	pressure (Pa)
t	time (s)
V	volume (m^3)
W	work (J)

Greek symbols:

Δ	difference over time

Subscripts:

D	draw
F	feed
gross	gross
in	membrane inlet
loss	pressure loss
net	net
out	membrane outlet
p	permeate

3.7 Supplementary Notes

3.7.1 Supplementary Note 3.1: Water permeate and power analysis

Water permeate flux and net PRO power were experimentally evaluated in real-time as operating conditions were varied by the maximum power point tracking algorithm and controller. Testing was conducted on a laboratory scale PRO bench at Oakland University. Figure S3.1 provides a sample of raw data collected over a period of 60 s. Also shown is the input command signals for the three control variables, as well as a moving average for the raw experimental data. Table S3.1 provides a detailed description of how measured data is analyzed to calculate water permeate flux and net power output. As shown, the moving average of sensor data is used to filter noise when evaluating water permeate rate and power, especially related to the draw side pressure loss which shows very high variability. Propagation of experimental uncertainty is also described in Table S3.1.

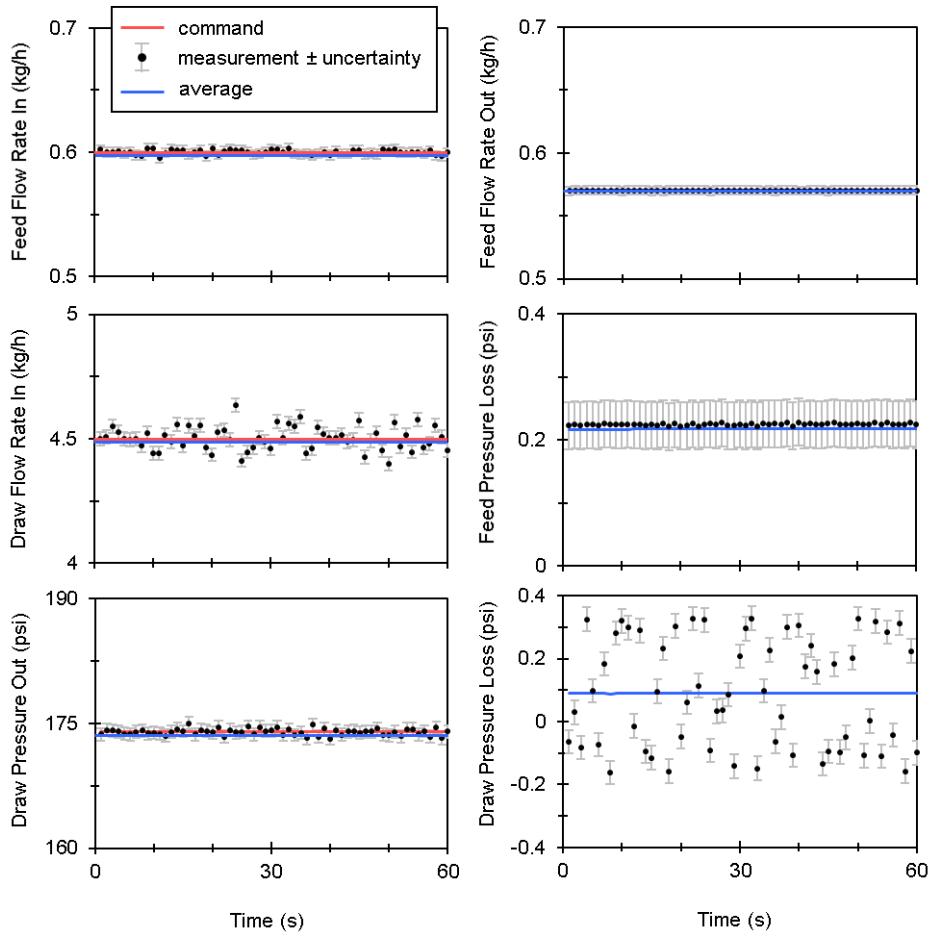

Figure S3.1. Sample of raw experimental test data obtained during real-time operation of the PRO maximum power point tracker. Inlet feed flow rate is controlled and measured by a mass flow controller (K-D100A-SCF-S0A-KA-2X, Alicat Scientific (Tucson, AZ), 1 ± 0.006 kg/hr). Inlet draw flow rate is controlled and measured by a mass flow controller (KF-F200A-SCF-S0A-KA-2X, Alicat Scientific (Tucson, AZ), 10 ± 0.06 kg/hr). Pressure applied to the draw outlet is controlled and measured by a pressure controller (PCS-100PSIG-D-PCA17/5P, Alicat Scientific (Tucson, AZ), 300 ± 0.75 psi). Outlet feed flow rate is measured by flow sensor (K-D100A-SCF-S0A-KA-2X, Alicat Scientific (Tucson, AZ), 1 ± 0.006 kg/h). Pressure loss across the feed channel is measured by a differential pressure sensor (PS-30PSID-D/5P, Alicat Scientific (Tucson, AZ), 15 ±0.0375 psi). Pressure loss across the draw channel is measured by a differential pressure sensor (PS-30PSID-D/5P, Alicat Scientific (Tucson, AZ), 15 ±0.0375 psi).

Table S3.1 Analysis of sample raw data and propagation of experimental uncertainty

Parameter	Value	Measurement or Analysis
Preparation of draw solution		
Feed water mass $m_{D,w}$	5276.0 ± 0.2 g	Mass balance, AX8201, Ohaus (Parsippany, NJ), 8000 ± 0.2 g
Feed salt mass $m_{D,s}$	369.6 ± 0.2 g	Mass balance, AX8201, Ohaus (Parsippany, NJ), 8000 ± 0.2 g
Feed concentration c_D	70.05 ± 0.04 g/l	$c_D = \frac{m_{D,s}}{m_{D,w}}\rho$, $\frac{\delta c_D}{c_D} = \sqrt{\left(\frac{\delta m_{D,w}}{m_{D,w}}\right)^2 + \left(\frac{\delta m_{D,s}}{m_{D,s}}\right)^2}$ $\rho = 1000$ kg/m^3
Measurements at sample instant t = 60 s		
Inlet feed flow rate $\dot{m}_{F,in}$	0.5998 ± 0.0036 kg/h	Mass flow controller, KF-D100A-SCF-S0A-KA-2X, Alicat Scientific (Tucson, AZ), 1 ± 0.006 kg/h or 0.6 % reading (greater of the two)
Inlet draw flow rate $\dot{m}_{D,in}$	4.4530 ± 0.0267 kg/h	Mass flow controller, KF-F200A-SCF-S0A-KA-2X, Alicat Scientific (Tucson, AZ), 10 ± 0.06 kg/h or 0.6 % reading
Outlet feed flow rate $\dot{m}_{F,out}$	0.5702 ± 0.0034 kg/h	Mass flow meter, K-D100A-SCF-S0A-KA-2X, Alicat Scientific (Tucson, AZ), 1 ± 0.006 kg/h or 0.6 % reading
Outlet draw pressure $p_{D,out}$	174.06 ± 0.75 psi	Pressure controller, PCS-100PSIG-D-PCA17/5P, Alicat Scientific (Tucson, AZ), 300 ± 0.75 psi
Feed pressure loss $p_{F,loss}$	0.1877 ± 0.0375 psi	Differential pressure meter, PS-30PSID-D/5P, Alicat Scientific (Tucson, AZ), 15 ± 0.0375 psi
Draw pressure loss $p_{D,loss}$	0.0876 ± 0.0375 psi	Differential pressure meter, PS-30PSID-D/5P, Alicat Scientific (Tucson, AZ), 15 ± 0.0375 psi
Average measurements from t = 0 up to sample instant t = 60 s		
Average of inlet feed flow rate $\overline{\dot{m}_{F,in}}$	0.6000 ± 0.0036 kg/h	$\overline{\dot{m}_{F,in}} = \frac{1}{n}\sum_{i=1}^{n}\dot{m}_{F,in}(i)$ $\overline{\delta\dot{m}_{F,in}} = \frac{1}{n}\sum_{i=1}^{n}\delta\dot{m}_{F,in}(i)$

Table S3.1 —Continued

Average of inlet draw flow rate $\overline{\dot{m}_{D,in}}$	4.5000 ± 0.0267 kg/h	$\overline{\dot{m}_{D,in}} = \frac{1}{n}\sum_{i=1}^{n} \dot{m}_{D,in}(i)$ $\delta\,\overline{\dot{m}_{D,in}} = \frac{1}{n}\sum_{i=1}^{n} (\delta\dot{m}_{D,in}(i))$
Average of outlet feed flow rate $\overline{\dot{m}_{F,out}}$	0.5701 ± 0.0034 kg/h	$\overline{\dot{m}_{F,out}} = \frac{1}{n}\sum_{i=1}^{n} \dot{m}_{F,out}(i)$ $\delta\,\overline{\dot{m}_{F,out}} = \frac{1}{n}\sum_{i=1}^{n} (\delta\dot{m}_{F,out}(i))$
Average of outlet draw pressure $\overline{p_{D,out}}$	174.00 ± 0.75 psi	$\overline{p_{D,out}} = \frac{1}{n}\sum_{i=1}^{n} p_{D,out}(i)$ $\delta\,\overline{p_{D,out}} = \frac{1}{n}\sum_{i=1}^{n} (\delta p_{D,out}(i))$
Average of feed pressure loss $\overline{p_{F,loss}}$	0.1876 ± 0.0375 psi	$\overline{p_{F,loss}} = \frac{1}{n}\sum_{i=1}^{n} p_{F,loss}(i)$ $\delta\,\overline{p_{F,loss}} = \frac{1}{n}\sum_{i=1}^{n} (\delta p_{F,loss}(i))$
Average of draw pressure loss $\overline{p_{D,loss}}$	0.0863 ± 0.0375 psi	$\overline{p_{D,loss}} = \frac{1}{n}\sum_{i=1}^{n} p_{D,loss}(i)$ $\delta\,\overline{p_{D,loss}} = \frac{1}{n}\sum_{i=1}^{n} (\delta p_{D,loss}(i))$

Flux and power analysis at sample instant t = 60 s

Inlet feed pressure $p_{F,in}$	16.20 ± 0.10 psi	$p_{F,in} = k\,\dot{m}_{F,in}$, $\frac{\delta p_{F,in}}{p_{F,in}} = \frac{\delta \dot{m}_{F,in}}{\dot{m}_{F,in}}$ k = 28.034 psi / kg/h, as specified in mass flow controller literature (KF-D100A-SCF-S0A-KA-2X, Alicat Scientific)
Applied pressure difference Δp	157.80 ± 0.76 psi	$\Delta p = \overline{p_{D,out}} - p_{F,in}$, $\delta\Delta p = \sqrt{\delta\overline{p_{D,out}}^2 + \delta p_{F,in}^2}$
Water permeate flux J_w	7.127 ± 1.182 l /m^2/h	$J_w = \frac{\overline{\dot{m}_{F,in}} - \overline{\dot{m}_{F,out}}}{a\,\rho}$, $\delta J_w = \sqrt{\delta\overline{\dot{m}_{F,in}}^2 + \delta\overline{\dot{m}_{F,out}}^2}$ a = 0.0042 m^2 , ρ = 1000 kg/m^3
Gross power density $\dot{W}_{gross}$	2.154 ± 0.357 W/ m^2	$\dot{W}_{gross} = J_w\,\Delta p$, $\frac{\delta \dot{W}_{gross}}{\dot{W}_{gross}} = \sqrt{\left(\frac{\delta J_w}{J_w}\right)^2 + \left(\frac{\delta \Delta p}{\Delta p}\right)^2}$

Table S3.1 —Continued

Feed power loss $\dot{W}_{F,loss}$	0.060 ± 0.010 W/ m^2	$\dot{W}_{F,loss} = \frac{\overline{\dot{m}_{F,in}}\ \overline{p_{F,loss}}}{a\,\rho}$, $\frac{\delta \dot{W}_{F,loss}}{\dot{W}_{F,loss}} = \sqrt{\left(\frac{\delta \overline{\dot{m}_{F,in}}}{\overline{\dot{m}_{F,in}}}\right)^2 + \left(\frac{\delta \overline{p_{F,loss}}}{\overline{p_{F,loss}}}\right)^2}$ a = 0.0042 m^2 , ρ = 1000 kg/m^3
Draw power loss $\dot{W}_{D,loss}$	0.176 ± 0.074 W/ m^2	$\dot{W}_{D,loss} = \frac{\overline{\dot{m}_{D,in}}\ \overline{p_{D,loss}}}{a\,\rho}$, $\frac{\delta \dot{W}_{D,loss}}{\dot{W}_{D,loss}} = \sqrt{\left(\frac{\delta \overline{\dot{m}_{D,in}}}{\overline{\dot{m}_{D,in}}}\right)^2 + \left(\frac{\delta \overline{p_{D,loss}}}{\overline{p_{D,loss}}}\right)^2}$ a = 0.0042 m^2 , ρ = 1045 kg/m^3
Net power density $\dot{W}_{net}$	1.918 ± 0.365 W/ m^2	$\dot{W}_{net} = \dot{W}_{gross} - \dot{W}_{F,loss} - \dot{W}_{D,loss}$, $\frac{\delta \dot{W}_{net}}{\dot{W}_{net}} = \sqrt{\delta \dot{W}_{gross}{}^2 + \delta \dot{W}_{F,loss}{}^2 + \delta \dot{W}_{D,loss}{}^2}$

CHAPTER FOUR
EFFECTIVELY USING HEAT TO THERMALLY ENHANCE PRESSURE RETARDED OSMOSIS

4.1 Introduction

Thermal energy from sources such as solar radiation and industrial waste heat is abundant and represents a tremendous resource for improving the sustainability of water and energy infrastructure in the US and throughout the world [136,137,70]. With this motivation, there has recently been increased interest in exploiting thermal gradients in membrane-based processes. This has led to advances and innovation in water treatment and desalination processes such as development of membrane distillation [138–141], and in energy recovery and power generation processes such as development of pressure retarded vapor permeation [142,143], closed-loop osmotic heat engines [144–147], and others .

Of particular interest is the potential for using heat to improve the performance of pressure retarded osmosis for power generation [71,72,148–157]. Pressure retarded osmosis (PRO) is an energy conversion process that uses the chemical potential available from salt gradients to drive osmosis against a load, thereby doing useful mechanical work [57,158–161], as illustrated in Figure 4.1. The concept can be exploited for electricity generation in a stand-alone power plant [63,162–164], or for energy recovery from the concentrated brine of a desalination plant [165–167] .

Chapter Four is based primarily on a paper that was published in the Desalination Journal.

S. Chintalacheruvu, Y. Ren, and J. Maisonneuve, "Effectively using heat to thermally enhance pressure retarded osmosis," Desalination, Vol. 556: 116570, 2023. DOI: 10.1016/j.desal.2023.116570

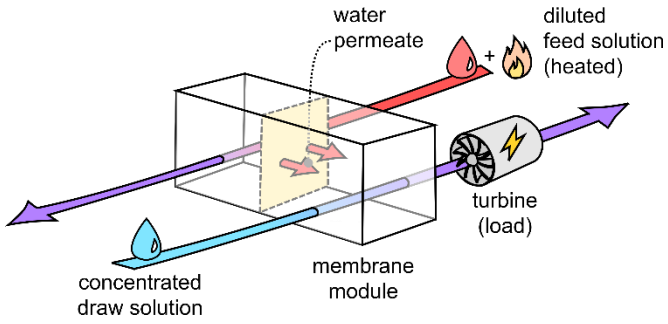

Figure 4.1 Concentrated solution such as seawater or desalination brine can be used to draw water permeate across a semi-permeable membrane from a diluted feed source to do positive work on a load such as a turbine. The concept is known as pressure retarded osmosis (PRO) and can be thermally-enhanced via the application of heat.

Recent work has demonstrated that PRO can be greatly enhanced via the application of low-grade heat. Significant improvements in water permeate and energy recovery rates can be achieved by heating feed and draw solutions that are supplied to the membrane module. For example, power can be increased by more than 200 % compared to baseline operation at room temperature [71,150], to achieve power density well above 10 W/m^2 at relatively low temperatures between 40-50 °C [71,72,151]. Similar trends have also been reported when heat is applied to other osmotic processes. For example, in thermally-enhanced forward osmosis (FO) [168–178], water flux can be more than doubled at low temperatures between 40-50 °C [171,177]. And in thermally-enhanced reverse osmosis (RO) [73,179,180], the specific energy of seawater desalination can be reduced by 10-40 % in certain cases [73].

Therefore, while the literature on thermally-enhanced osmosis is extensive, certain contradictions and questions persist. For example, the literature for thermally-enhanced PRO shows that heating only the feed solution consistently outperforms heating only the draw [151,153,155], however it is not clear why this is. It is generally agreed that much

of the improvement observed in thermally enhanced osmosis is because warmer membranes tend to be more permeable [71,72,148–152,155–157,169,171,175,178], and therefore it might be supposed that heating the feed will yield a hotter membrane than heating the draw, but again it is not clear why this is. Detailed models such as developed by Chowdhury and McCutcheon [172] provide some insight into the fundamental transport mechanisms that might explain this dynamic, but in general, very few publications provide a detailed description of the temperature field in the membrane module and therefore it is difficult to confirm what dynamics are primarily responsible for the observed trends. Interestingly, the literature on thermally-enhanced FO is not nearly as consistent, with certain publications suggesting a preference for heating only draw solution [173,175,181], and others suggesting to heat only the feed [168,169,172,177]. Any explanation of the fundamental mechanics behind thermally-enhanced osmosis, must therefore reconcile these apparent differences.

In addition, a second gap in the current literature is related to the question of effectiveness. While certain publications have considered whether it is more effective to heat the feed or draw solutions [151,153,155], as discussed above, there are so far none that consider what specific operating temperatures are most effective. In the case where heat to the system is to be supplied by an external source of thermal energy, efforts should be made to ensure that a maximum increase in PRO power is achieved per unit temperature change.

This chapter investigates the process of thermally-enhanced PRO and addresses these specific gaps in the current literature: (1) What transport mechanisms govern the preference to heat either feed or draw solutions? And (2), what temperatures most

effectively increase power? Laboratory test trials of thermally-enhanced PRO are conducted across a range of feed and draw temperatures, and results are used to validate a finite element model that describes concentration and temperature profiles across the membrane. This model addresses several shortcomings in other published PRO transport models, and provides insight into the fundamental transport mechanisms that govern the preference to heat feed. In addition, we introduce an effectiveness metric, which normalizes power improvements relative to temperature changes. The effectiveness of a range of feed and draw temperatures is evaluated, and compared against results reported elsewhere in the literature.

4.2 Theory

During PRO, water permeates across a selective membrane to do work on an applied load. The rate at which work is done $\dot{W}$ is the product of the volume rate of water permeate $\dot{V}_p$ and the applied load pressure Δp.

$$\dot{W} = \dot{V}_p \, \Delta p \tag{4.1}$$

Because water permeate is driven by osmosis, and osmosis is largely dependent on concentration and temperature, a careful analysis of mass and heat transport dynamics is necessary to describe thermally-enhanced PRO. Figure 4.2 provides a simplified illustration of the process at steady-state, using a convenient lumped-element equivalent circuit. The circuit shows water transfer driven by the difference between osmotic pressure and applied pressure, salt transfer driven by diffusion and water convection, and heat transfer driven by diffusion and water and salt convection. Governing equations for

each of the three domains are described throughout Section 4.2, and a numerical finite element solution to the system of equations is provided in Section 4.3.

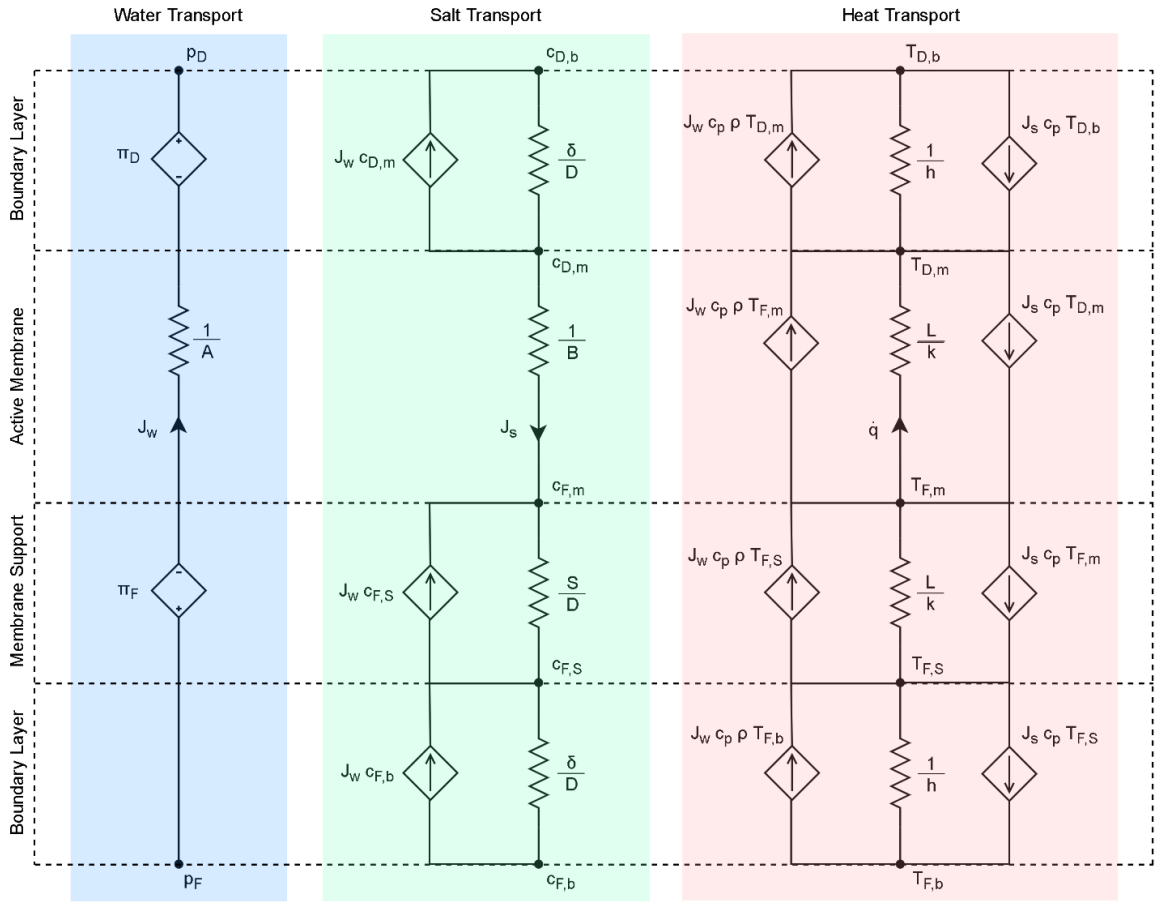

Figure 4.2 Lumped-element analog circuit approximating steady-state water, salt, and heat transport during thermally enhance pressure retarded osmosis.

4.2.1 Water Transport

PRO water permeate is driven by osmotic pressure against an applied pressure, as a function of the membrane's permeability. The volume rate of water permeate $\dot{V}_p$ can be normalized per unit membrane area a and expressed as water flux J_w.

$$J_w = \frac{\dot{V}_p}{a} = A\,(\Delta\pi - \Delta p) \tag{4.2}$$

Where A is the membrane's permeability to water, $\Delta\pi = \pi_{D,m} - \pi_{F,m}$ is the driving osmotic pressure difference across the active membrane, and $\Delta p = p_D - p_F$ is the opposing applied pressure difference.

Osmotic pressure is often approximated by the Van't Hoff equation.

$$\pi = i\,R\,T\,c\,/\,M \tag{4.3}$$

Where i is the number of ions, R is the gas constant, T is the solution temperature, c is the salt concentration, and M is the molar mass of salt.

The osmotic pressure difference across the active membrane layer will be less than the difference between the bulk feed and draw solutions. This is because osmotic pressure is a function of both temperature and concentration, and both of these will exhibit non-linear distributions across the membrane profile. Therefore, to determine $\Delta\pi$, it is necessary to define the temperature and concentration at the active membrane surfaces, which are $T_{D,m}$ and $c_{D,m}$ at the draw-side and $T_{F,m}$ and $c_{F,m}$ at the feed-side. A careful analysis of both thermal and salt transport dynamics is needed to accurately evaluate water permeate.

In a thermally-enhanced PRO process, osmotic pressure will be directly influenced by temperature. Figure 4.3(a) shows osmotic pressure difference across a membrane as a function of temperature at the active membrane surfaces.

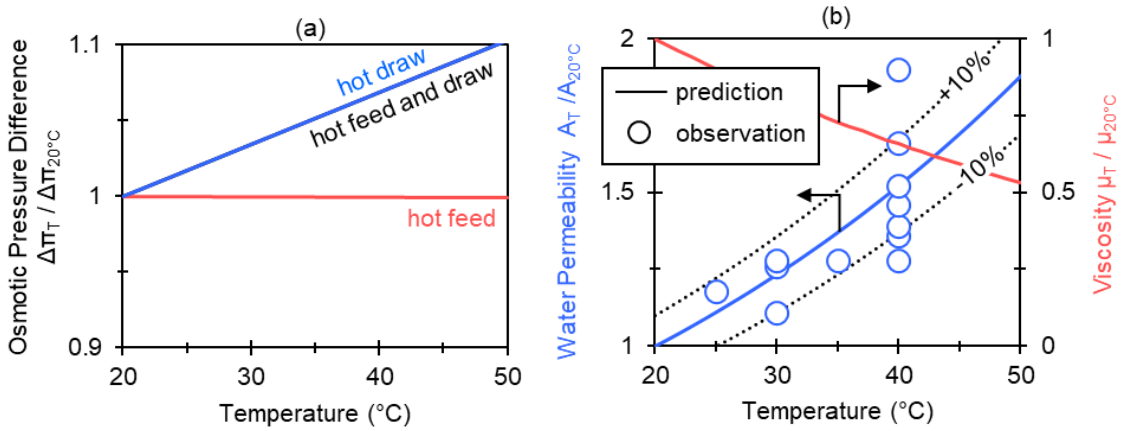

Figure 4.3 (a) Osmotic pressure difference across the active membrane layer when both the feed-side and draw-side membrane surfaces are heated, as well as when only one of the feed-side or draw-side surfaces are heated. (b) Membrane water permeability as a function of temperature can be predicted from the inversely proportional drop in the permeate fluid viscosity, as described in equations (4.4) and (4.5). The prediction for membrane water permeability is compared against experimental observations selected from the literature [71,144,150,157,172,174,175,182].

As shown, when both feed and draw surfaces are heated, the osmotic pressure difference will scale proportionally with temperature, increasing by about 10 % from 20 to 50 °C. A similar, and even slightly greater increase in osmotic pressure difference is observed when only the draw-side is heated. This is because thermally-induced increases to the feed-side osmotic pressure are undesirable, although mostly negligible because the feed solution osmotic pressure is minor. Considered in isolation, this dynamic would suggest that heating only draw solution is preferable to heating feed, however the literature indicates otherwise [151,153,155]. Other competing dynamics help to explain this apparent discrepancy.

Among these other dynamics, it is generally agreed that much of the improved flux observed in thermally-enhanced osmosis is due to a perceived increase in membrane water permeability [71,72,148–152,155,157,169,171,175,178]. Importantly, this

perceived increase in membrane water permeability is due primarily to changes in the permeate fluid viscosity [149,152,178,180], rather than any thermally induced change in the membrane structure itself [149,153]. Figure 4.3(b) shows the theoretical membrane water permeability *A* that would be anticipated simply from the inversely proportional change in fluid viscosity μ, as defined by equations (4.4) and (4.5) [73,149,152,172,180,183–185]. A collection of water permeability measurements selected from the literature are also included in the plot, to compare against the prediction. As shown, the change in the apparent membrane permeability can be reasonably approximated by the change in viscosity, with only a few exceptions falling beyond the 10 % margin of error.

$$\mathrm{A} = \mathrm{A}_{20\,^{\circ}\mathrm{C}}\,\frac{\mu_{20\,^{\circ}\mathrm{C}}}{\mu} \tag{4.4}$$

$$\mu = 0.4599\,\exp(1.796 \times 10^{3}\,\mathrm{c} - 0.021\,\mathrm{T}) \tag{4.5}$$

As shown, thermally induced changes in membrane permeability appear to be more significant than changes induced in the osmotic pressure. For example, when permeate temperature increases from 20 to 50 °C, the permeate fluid viscosity is nearly halved, and consequently the membrane water permeability is nearly doubled. Such a change in membrane permeability will have a significant effect on water flux and power, as others in the literature have also suggested [71,72,148–152,155,157]. However, this analysis does not necessarily explain why heating feed increases water flux more than heating draw [151,153,155]. To make such a determination, it is necessary to consider the temperature profile across the asymmetric membrane and determine whether hot feed or hot draw will yield a hotter active membrane layer. Presumably a hot active membrane

layer would maximize the membrane water permeability by minimizing the fluid viscosity. Analysis of the concentration and temperature profiles that result from salt and heat transport across the membrane is provided in Sections 4.2.2 and 4.2.3

4.2.2 Salt Transport

High PRO water flux requires that the osmotic pressure difference across the active membrane be maximized, and ideally approach the difference between the bulk solutions. This is difficult to achieve because of non-ideal transport dynamics such as the leakage of salt across the imperfectly selective membrane, and the accumulation of salt in the membrane support structure and boundary layers. These tend to develop a non-linear concentration profile across the membrane and as a result, the effective concentration difference across the active membrane is much less than the potential difference between the bulk solutions. This dynamic is typically referred to as concentration polarization and has been widely studied for a number of osmosis applications [125,186–189].

Concentration at the draw and feed surfaces of the active membrane $c_{D,m}$ and $c_{F,m}$ can be evaluated by considering the polarization profile that results from the steady-state equilibrium of salt and water transport across the membrane. Salt transport through the active membrane layer is driven by diffusion, as defined in equation (4.6). And salt transport through the membrane support structure and surface boundary layers is driven by both convection from water flux and back diffusion along the concentration gradient, as defined in equation (4.7). Salt flux J_s is defined here as the mass rate of salt permeate $\dot{m}_s$ normalized per unit membrane area a.

$$J_s = \frac{\dot{m}_s}{a} = B\,\Delta c \tag{4.6}$$

$$J_s = \frac{\dot{m}_s}{a} = D\,\frac{dc}{dn} - J_w\,c \tag{4.7}$$

Where B is the membrane salt permeability, $\Delta c = c_{D,m} - c_{F,m}$ is the effective concentration difference across the active membrane, D is the salt diffusivity, and dc / dn is the concentration gradient normal to the membrane surface.

Adding heat to the PRO process will affect salt transport in a number of ways. First, the perceived increase in membrane water permeability discussed previously, will be coupled with an increase in salt permeability [71,72,148–153,155,157,169,171,175]. Again, most of the observed increase in permeability will be due to changes in the fluid properties, in this case an increase in the salt diffusivity [149,152,172,175], rather than any thermally induced changes in the membrane structure itself. Figure 4.4(a) shows the theoretical membrane salt permeability that can be anticipated from the proportional change in salt diffusivity, as defined by equations (4.8) and (4.9) (see Supplementary Note 4.1 for derivation) [125,153]. A collection of salt permeability measurements from the literature are also included in the plot, to compare against the prediction. As shown, the change in the apparent membrane salt permeability can be approximated by the change in diffusivity, with a few exceptions falling beyond the 20 % margin of error.

$$B = B_{20\,°C}\ \frac{D}{D_{20\,°C}} \tag{4.8}$$

$$D = \ 6.725 \times 10^{-6} \exp\left(1.546 \times 10^{-4}\,c - \frac{2513}{T}\right) \tag{4.9}$$

As shown, thermally induced changes in the apparent salt permeability of the membrane are significant. For example, when fluid temperature increases from 20 to 50 °C, the salt diffusivity and hence salt permeability more than double. This increase in salt

permeability is even greater than the increase in water permeability reported previously in Figure 4.3, so that the A/B ratio drops by almost 20 % from 20 to 50 °C. This increase in B and this drop in A/B are certainly not desirable, but their significance can only be properly evaluated by considering their net effect on water permeate and ultimately PRO power. For example, it is very possible that a small change in A can be more significant than a large change in B.

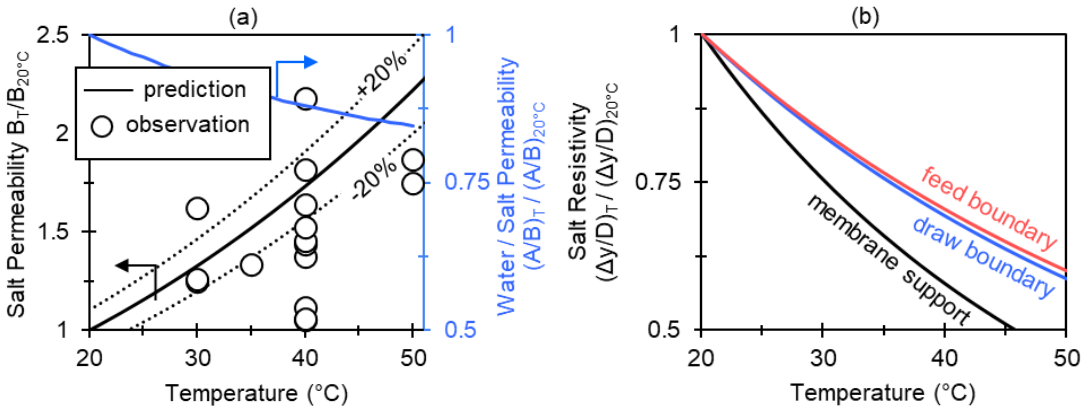

Figure 4.4 (a) Membrane salt permeability as a function of temperature can be predicted from the proportional change in salt diffusivity, as described in equations (4.8) and (4.9). The model for membrane salt permeability is compared against experimental observations from the literature [71,144,154,171,172,174,175,181]. (b) Resistivity to salt diffusion presented by the feed boundary layer, the draw boundary layer, and the membrane support layer when each of these layers are heated.

Equally important to consider is that although salt flux is exacerbated in thermally-enhanced osmosis, the accumulation of salts within the membrane support structure and at its surfaces is mitigated. This can be observed from analysis of equation (4.7) which defines resistivity to salt diffusion as Δn / D, where Δn is the thickness of some part of a discretized membrane profile. This can be the thickness of the feed boundary layer δ_F, the

thickness of the draw boundary layer δ_D, or the effective thickness of the support layer S. The thickness of each of these layers is itself a function of temperature as defined later in Section 4.3, and as a result will increase slightly with heat. Nevertheless, this increased thickness will be less than the increased diffusivity, such that the overall effect of heat will be to reduce salt resistivity [72,150,154,157]. Figure 4.4(b) shows the resistivity of each of the three layers as a function of temperature. In all cases a marked drop in the resistance to salt diffusion is observed. For example, as temperature increases from 20 to 50 °C, the boundary layer resistivities are reduced by 40 % and the support layer by 55 %. Such a drop will favor water permeate by lessening the severity of concentration polarization [148,151,157].

4.2.3 Heat Transport

From the analysis of water and salt mass transport presented so far, it should be clear that water permeate in a thermally-enhanced PRO process depends on the temperature profile across the membrane. For example, the membrane's apparent water and salt permeability are a function of the fluid temperature as it passes through the active membrane layer. Also, the concentration difference across the membrane depends on the severity of polarization, which is sensitive to temperature. And of course, the osmotic pressure difference itself is a direct function of fluid temperature at both the feed and draw membrane surfaces. An accurate picture of the temperature field is therefore essential to any prediction of water permeate.

Temperature distribution across the membrane depends largely on the way in which heat is delivered to the system, and the boundary conditions that are thereby imposed. Recently, a number of creative methods have been proposed to deliver heat directly to the

membrane and thereby provide more efficient temperature control of targeted layers [190–200]. In this study however, we focus our analysis on the case where heat is supplied to the bulk fluids before they are introduced to the membrane module. When only one of either the bulk feed or draw solutions are heated, heat transfer by diffusion and convection will establish an equilibrium temperature gradient across the membrane and its thermal boundary layers. Of course, when both bulk solutions are heated to the same temperature, the profile is simply uniform (assuming no heat loss to the surrounding environment).

Steady-state heat transport through the active membrane and its support and boundary layers is the equilibrium of both diffusion as well as convection from water flux from the feed and salt flux from the draw, as defined in equation (4.10). Heat flux $\dot{q}$ is defined here as the rate of thermal energy transfer $\dot{Q}$ normalized per unit membrane area a.

$$\dot{q} = \frac{\dot{Q}}{a} = k \frac{dT}{dn} + J_w \rho c_{p,w} T - J_s c_{p,s} T \tag{4.10}$$

Where k is the thermal conductivity, dT / dn is the temperature gradient normal to the membrane surface, ρ and $c_{p,w}$ are the density and specific heat capacity of water, and $c_{p,s}$ is the specific heat capacity of salt.

4.3 Materials and Methods

4.3.1 Experimental Analysis

4.3.1.1 Laboratory Test Apparatus

Laboratory-scale experimental testing was performed to evaluate the performance of thermally-enhanced PRO at a number of temperatures and operating pressures. The laboratory bench shown in Figure 4.5 was used for all experiments. The bench consists of

a 4-port flat-sheet membrane cell (CF042, Sterlitech, Kent, WA) supplied by variable speed pumps (GAF-T23-DEMSE, Micropump, Vancouver, WA). Temperature of each stream is regulated independently by circulating fluid through a custom PID-controlled thermal bath (WRNK-171S K-type thermocouple and SYL-2352 PID temperature controller, Auber Instruments, Alpharetta, GA). Applied pressure is controlled via a spring-loaded back-pressure regulator (KBP series, Swagelok, Solon, OH). Pressure transmitters (± 0.625 psi, EW-68075-50, Cole-Parmer, Vernon Hills, IL) and temperature transmitters (± 0.465 °C, 800-200-1-1-8-8-040-6 RTD, Noshok, Berea, OH) are mounted at inlet and outlet membrane ports. Data is recorded by an auto-logging system (EW-30005-35 Precision Digital, Hopkinton, MA) connected to a PC.

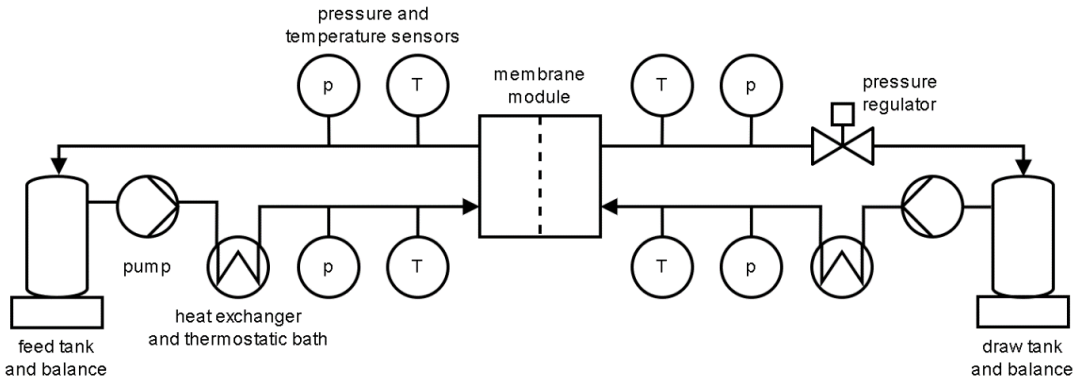

Figure 4.5 Schematic of the laboratory osmosis bench consisting of membrane housing, feed and draw tanks and pumps, and temperature and pressure controls and sensors.

4.4.1.2 Membrane and Module Parameters

A commercial cellulose triacetate membrane (FTS H2O, Albany, OR) was selected for this study. This membrane has been previously used in a variety of osmosis studies

[201–205]. Flat-sheet membrane coupons were mounted in the clear acrylic module accommodating samples with effective area of 42 cm^2. (107 mm length × 39 mm width). To facilitate operation at the desired flow velocities and provide support to the membranes, shims were inserted into both the feed and draw channels reducing the effective depth to 0.801 mm. The feed channel was also equipped with a 31-mil diamond-shaped spacer to provide support for when pressure is applied. A summary of the membrane module parameters is provided in Table 4.1.

Membrane characterization was done following standard test procedures [186,206] to find the membrane's water permeability A, salt permeability B, and structure parameter S. All testing was performed at room temperature to provide a reference from which permeability could be evaluated as a function of temperature, as described in equations (4.4) and (4.8). Results are shown in Figure 4.6, and a detailed record of raw test data and analysis is provided in Supplementary Notes 4.2-4.4.

Table 4.1 Membrane and module parameters.

Material	cellulose triacetate
Configuration	flat sheet
Dimensions (l × w)	107 mm × 39 mm
Area a	42 cm^2.
Channel depth d	0.801 mm
Feed channel spacer	31-mil diamond-shaped

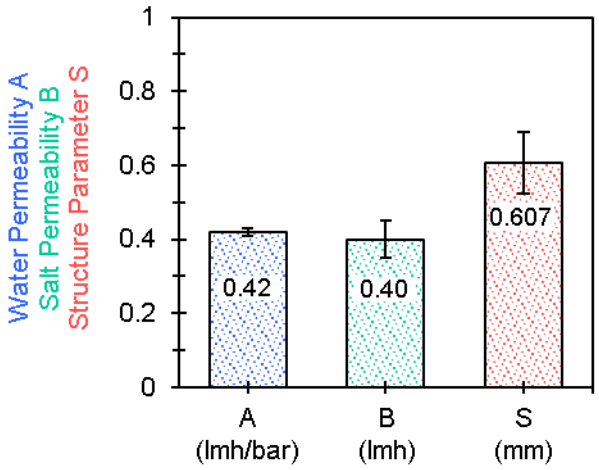

Figure 4.6 Characteristic membrane parameters measured at room temperature following standard test methods [186,206].

4.4.1.3 Osmosis Test Conditions

PRO performance was evaluated across a range of feed and draw temperatures from 20–50 °C and applied pressures from 0–8 bar. Feed and draw solutions with concentrations of 0.1 and 35 g/l were prepared from sodium chloride NaCl (> 99% purity, Fisher Scientific, Hampton, NH) and deionized water, and then supplied to the membrane cell at circulation rates of 0.147 m/s. A summary of test conditions is provided in Table 4.2.

Water permeate flux J_w across the membrane was experimentally measured by observing the change in feed and draw mass Δm at mass balances (± 0.2 g, AX8201 Ohaus, Parsippany, NJ) over some time interval Δt of at least 60 minutes, as described in equation (4.11). For verification, the change in both the feed and draw mass was recorded and compared. Power $\dot{W}$ was then obtained as the product of water flux and the applied

pressure difference, as described in equation (4.12). A detailed description of raw data, analysis methods, and propagation of uncertainty is provided in Supplementary Note 4.5.

Table 4.2 Experimental test conditions

Flow configuration	Counter flow
Flow velocity u	0.147 m/s
Salt	NaCl
Feed concentration c_F	0.1 g/l
Draw concentration c_D	35 g/l
Pressure difference Δp	0 – 8 bar
Temperature T_F and T_D	20 – 50 °C

$$J_w = \frac{\Delta m}{a\ \rho\ \Delta t} \tag{4.11}$$

$$\frac{\dot{W}}{a} = J_w\ \Delta p \tag{4.12}$$

To provide a measure of effectiveness, the observed permeate and power results were normalized over thermal energy input. Equation (4.13) defines the change in flux and power per unit temperature change, relative to the baseline case in which feed and draw are at room temperature. Similar metrics have previously been proposed in the literature, such as in [152,176], but in those cases the change in temperature over which performance was normalized, considered only the change of one of the bulk solutions, not both. So, for example, when both feed and draw solutions are heated, previously proposed metrics would normalize performance over the same change in temperature as when only one fluid was heated. This does not accurately reflect the fact that heating both

will require approximately double the thermal energy input as compared to when only one solution is heated. By making such a distinction, the effectiveness metric we define here provides a better representation of thermal energy investment, and we recommend it for future studies related to thermally-enhanced osmosis. We propose another approach to calculating the effectiveness based on the increase in power density with respect to the heat added. This is described in detail in Supplementary Note 4.7.

$$\eta = \frac{\left(\frac{J_w - J_{w,20\,^\circ C}}{J_{w,20\,^\circ C}}\right)}{\left(T_F - T_{F,20\,^\circ C}\right) + \left(T_D - T_{D,20\,^\circ C}\right)} = \frac{\left(\frac{\dot{W} - \dot{W}_{20\,^\circ C}}{\dot{W}_{20\,^\circ C}}\right)}{\left(T_F - T_{F,20\,^\circ C}\right) + \left(T_D - T_{D,20\,^\circ C}\right)} \tag{4.13}$$

4.3.2 Numerical Analysis

Numerical analysis was undertaken to confirm experimental results and identify transport dynamics that are responsible for observed trends. To do this, the governing transport equations introduced in Section 4.2 were discretized to express changes in concentration Δc and temperature ΔT over a finite element of the membrane profile. Table 4.3 provides a summary of the discretized transport equations that are specific to each of the membrane's sublayers. As shown, the active membrane layer (with thickness t_m), the support structure (with thickness t_S), and both of the thermal and concentration surface boundaries (with thicknesses δ_t and δ respectively) are discretized into N number of elements, such that the thickness of each finite element is given by Δn. A distinction is made between the thermal and concentration boundary layers, which are not of the same

thickness and therefore only partially overlap. In this case, the thermal boundary layer extends beyond the concentration boundary by a difference of $\delta_t - \delta$.

Table 4.3 Discretized transport equations for concentration and temperature across a finite element of the membrane's normal profile.

	Feed boundary layer		Membrane		Draw boundary layer	
Discrete change in:	Thermal	Thermal and concentration	Support layer	Active layer	Thermal and concentration	Thermal
Position Δn	$(\delta_{F,t} - \delta_F)/N$	δ_F/N	t_S/N	t_m/N	δ_D/N	$(\delta_{D,t} - \delta_D)/N$
Concentration $\Delta c(i)$	0	$\frac{J_w\, c(i) + J_s}{D(i)}\Delta n$	$\frac{J_w\, c(i) + J_s}{D(i)}\frac{S\,\Delta n}{t_S}$	$\frac{J_s}{B(i)}\frac{\Delta n}{t_m}$	$\frac{J_w\, c(i) + J_s}{D(i)}\Delta n$	0
Temperature $\Delta T(i)$	$\frac{\left(\dot{q} - J_w\, \rho(i) c_{p,w}(i) T(i) + J_s\, c_{p,s}\, T(i)\right)}{h_F}\frac{\Delta n}{\delta}$		$\frac{\left(\dot{q} - J_w\, \rho(i) c_{p,w}(i) T(i) + J_s\, c_{p,s}\, T(i)\right)}{k(i)}\Delta n$		$\frac{\left(\dot{q} - J_w\, \rho(i)\, c_{p,w}(i)\, T(i) + J_s\, c_{p,s}\, T(i)\right)}{h_D}\frac{\Delta n}{\delta}$	

With the transport equations discretized, the concentration and temperature of a given element i+1 can be obtained by adding the discrete change to the initial values at element I, so that $c(i+1) = c(i) + \Delta c(i)$ and $T(i+1) = T(i) + \Delta T(i)$. Using this step-wise approach concentration and temperature profiles can be generated. Importantly, fluid properties such as viscosity, density, specific heat capacity, conductivity, and diffusivity, are functions of concentration and temperature and must therefore be updated at each element i. In addition, analysis of the discretized concentration and temperature equations in Table 4.3 shows that they are functions of water flux J_w, salt flux J_s, and heat flux $\dot{q}$, which are themselves functions of concentration and temperature. To solve this system of equations a numerical approach is used whereby an initial guess for each of the flux values is provided and then compared to the solution obtained after the concentration and temperature gradients are solved. The guess is updated, and the process is repeated until

the solution converges to within some acceptable tolerance. The flow chart in Figure 4.7 illustrates the proposed logic and sequence of operations.

Microsoft Excel 2019 (Microsoft, Redmond WA) software was used to implement the finite element model and simulate each of the experimental cases. A summary of the simulation input parameters is provided in Table 4.4. Unless otherwise specified, all simulation input parameters are consistent with experimental test conditions described in Section 4.3.1. Empirical expressions are provided to update fluid properties across the membrane profile, including viscosity μ, density ρ, specific heat capacity of water $c_{p,w}$, conductivity of water k_w, and diffusivity D. An expression for the thermal conductivity of the support structure k_S is defined by the sum of the water conductivity k_w and the polymer conductivity k_m which are parallel thermal branches in some proportion defined by the membrane porosity ε. Expressions for the Sherwood number Sh and the Nusselt number Nu, which are critical to concentration and thermal boundary layer dynamics, are provided from the literature for osmosis with a flat sheet membrane with a distinction made for the spacer-filled feed channel.

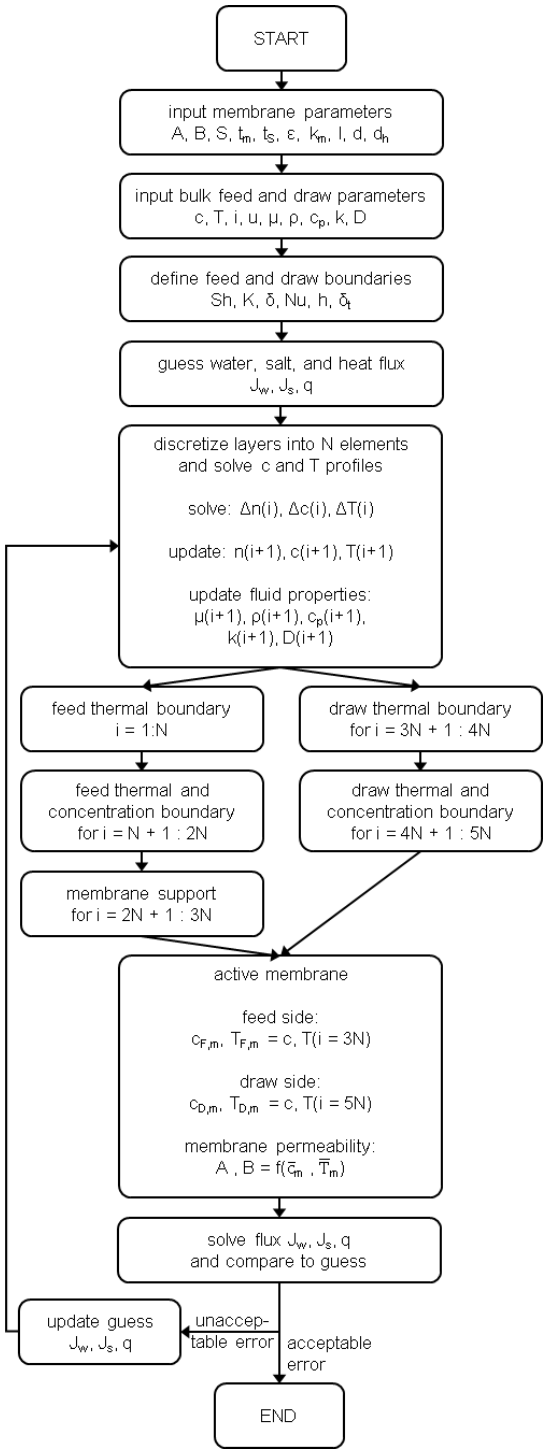

Figure 4.7 Numerical model for finite element analysis of temperature and concentration across a membrane in a thermally-enhanced pressure retarded osmosis process.

Table 4.4 Simulation input parameters

Membrane parameters	
Water permeability A	experimentally obtained
Salt permeability B	experimentally obtained
Structure parameter S	experimentally obtained
Active layer thickness t_m	0.1 μm [172]
Support layer thickness t_S	85 μm [172]
Membrane parameters	
Porosity ε	0.59 [172]
Membrane conductivity k_m	0.17 W/m/K [172]
Support conductivity k_S	$\varepsilon k_w + (1-\varepsilon) k_m$ [172,177,181,207]
Hydraulic diameter d_h	2 d [208]
Fluid properties	
Viscosity μ	$0.4599 \exp(1.796 \times 10^3 c - 0.021 T)$ [172,184,185]
Density ρ	$1005 + 7.062 \times 10^5 c - 0.3148 (T - 273.15) - 824.3 (T - 273.15) \frac{c}{M} - 3.783 \times 10^8 c^2$
Specific heat $c_{p,w}$	$4204 - 6.126 \times 10^6 c - 1.553 (T - 273) + 0.01977 (T - 273)^2 + 1.867 \times 10^4 (T - 273) c + 3.247 \times 10^{10} c^2$
Thermal conductivity k_w	$0.0013377 T + 0.2165$ [172]
Salt diffusivity D	$6.725 \times 10^{-6} \exp\left(1.546 \times 10^{-4} c - \frac{2513}{T}\right)$ [125,153]

Table 4.4—Continued

Concentration boundary	Feed	Draw
Sherwood *Sh*	$0.46\ \mathrm{Re}^{0.36}\ \mathrm{Sc}^{0.36}$ [209–211]	$1.85\ \mathrm{Re}^{\frac{1}{3}}\ \mathrm{Sc}^{\frac{1}{3}}\ \left(\frac{d_h}{l}\right)^{\frac{1}{3}}$ [94,209,210,212–214]
Mass transfer coefficient *K*		$\mathrm{Sh}\ D/d_h$
Boundary thickness δ		d_h/Sh
Thermal boundary	**Feed**	**Draw**
Nusselt *Nu*	$0.664\ \mathrm{Re}^{\frac{1}{2}}\ \mathrm{Pr}^{\frac{1}{3}}$ [215–220]	$1.85\ \mathrm{Re}^{\frac{1}{3}}\ \mathrm{Pr}^{\frac{1}{3}}\ \left(\frac{d_h}{l}\right)^{\frac{1}{3}}$ [215,218,221–223]
Convection coefficient *h*		$\mathrm{Nu}\ k/d_h$
Boundary thickness δ_t		$\mathrm{Le}^{\frac{1}{3}}\ d_h/\mathrm{Sh}$

This numerical model makes several improvements over others that have been proposed in the literature. Namely, this model discretizes the membrane profile solving for temperature and concentration at finite elements across the membrane support and boundary layers. This allows for fluid properties to be updated as a function of the concentration and temperature at each element, including viscosity, density, specific heat capacity, conductivity, and diffusivity. In contrast, most other models for thermally-enhanced osmosis take a lumped-element approach and solve for concentration and temperature at only the membrane surfaces [71,153–155,157,172,174,177,181]. As a result, most other models are often forced to assume fluid properties based on the concentration and temperatures of the bulk solutions [151,154,157]. Another important distinction between this model and others in the literature, is that we distinguish between the thickness of the concentration and thermal boundary layers, whereas most

publications assume that the two exactly overlap spatially [155,169,172,181]. This distinction allows for a much more accurate description of the concentration and temperature profiles, of the resulting fluid properties, and of heat and mass transfer across the membrane.

4.4 Results

4.4.1 Heating Feed is More Effective than Heating Draw in Thermally-Enhanced PRO

Figure 4.8 shows PRO water flux and power density at several combinations of feed and draw temperatures. An increase in temperature is clearly associated with an increase in water flux and power. For example, at zero applied pressure, the water flux increases from 10.8 to 17.3 lmh as feed and draw temperatures increase from 20 to 40 °C. Similarly, at an applied pressure difference of 7.5 bar, the power density is nearly doubled from 1.07 to 2.06 W/m^2 as feed and draw temperatures increase from 20 to 40 °C. In addition, Figure 4.8 shows good agreement between the model predictions and experimental observations with an overall coefficient of determination $R^2 = 0.88$ (see Supplementary Note 4.6).

Figure 4.8 also shows that heating only the feed solution increases power by more than heating only the draw solution, and almost as much as when both solutions are heated. For example, at applied pressure of 7.5 bar, heating feed from 20 to 40 °C increases power density from 1.07 to 1.99 W/m^2, whereas heating draw increases power only to 1.72 W/m^2. These results suggest that thermal energy can be more effectively used by supplying it to the feed solution.

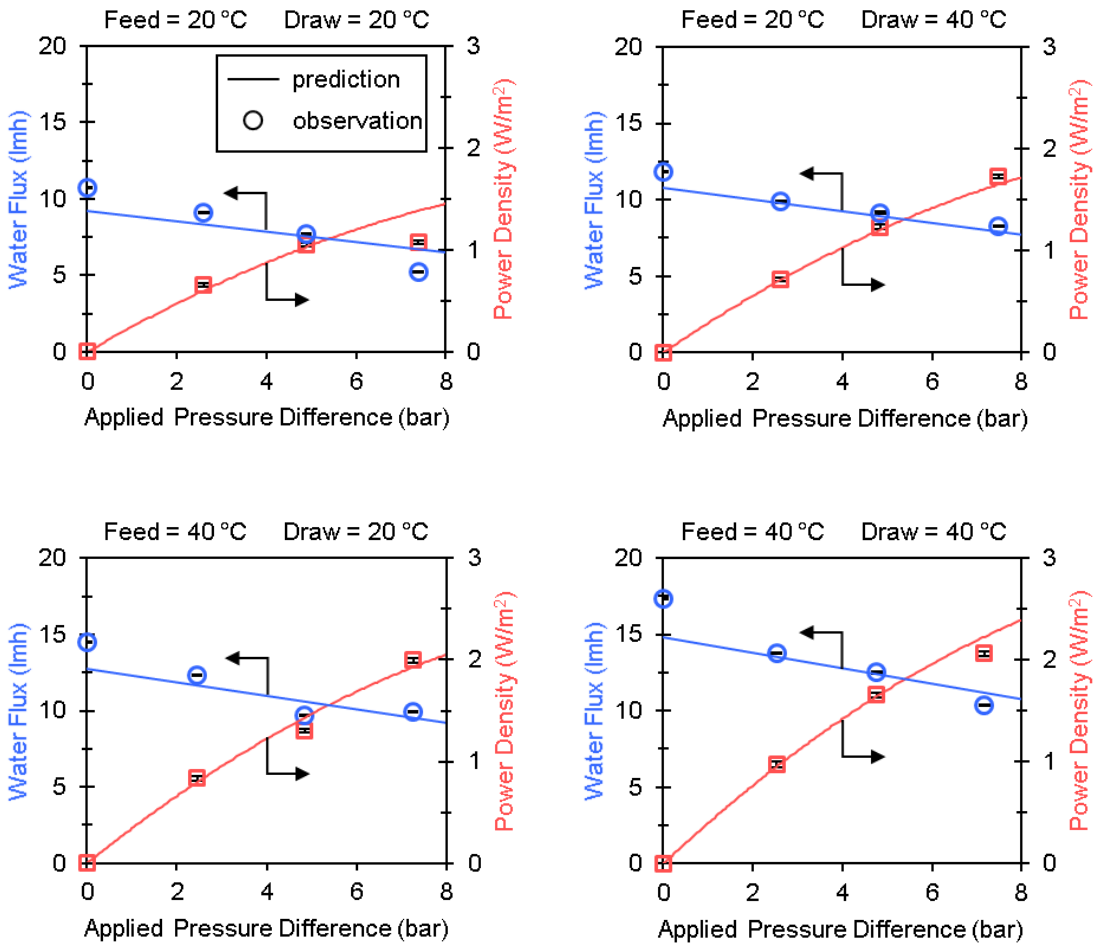

Figure 4.8 PRO water flux (left axis) and power density (right axis) at a variety of feed and draw temperatures. Experimental test conditions are specified in Table 4.2 and simulation input parameters are specified in Table 4.4.

To further illustrate this concept, we previously defined the metric of effectiveness in equation (4.13), which normalizes the percent change in power over the change in temperature. Figure 4.9 shows the effectiveness of the same temperature combinations considered previously in Figure 4.8, at a given applied pressure of 7.5 bar. As shown, heating both the feed and draw solutions does yield the highest power, but it requires more thermal energy input than heating only one of the solutions. The most effective use

of heat is shown for the case when only feed is heated, where a power increase of 4.15 % W/m^2 per °C is observed, compared to a power increase of only 2.26 % W/m^2 per °C when both solutions are heated.

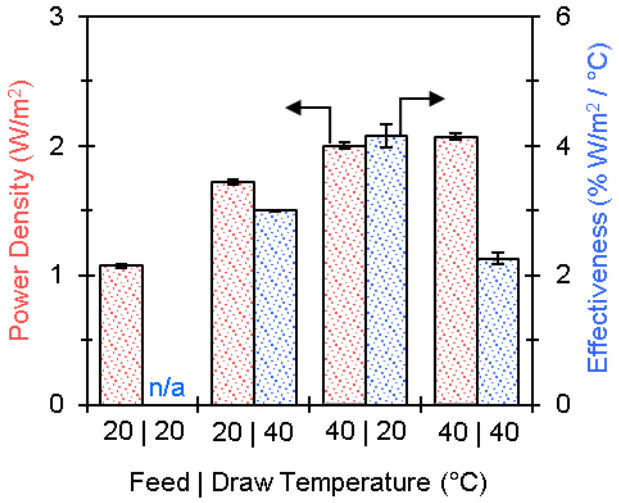

Figure 4.9 PRO power density (left axis) and effectiveness (right axis) for a variety of feed and draw temperatures, at an applied pressure difference of 7.5 bar. Effectiveness is a measure of the percent improvement in power per unit temperature change, relative to the baseline case at 20 °C. Experimental test conditions are specified in Table 4.2 and simulation input parameters are specified in Table 4.4.

4.4.2 Higher Temperatures Yield Higher Power but Lower Temperatures are More Effective

Given the effectiveness of heating only the feed, Figure 4.10 shows PRO performance in response to a range of different feed temperatures, and Figure 4.11 shows the effectiveness. As expected, flux and power increase with temperature, with maximum power of 2.22 W/m^2 observed at the highest feed temperature of 50 °C. However, when normalized per unit of temperature change, it appears that as feed is heated from 30 to 40

and then 50 °C, there is a diminishing return on the increase in power. The most effective use of heat is observed when feed temperature is only modestly increased to 30 °C, in which case a 5.79 % W/m^2 power increase per °C is obtained.

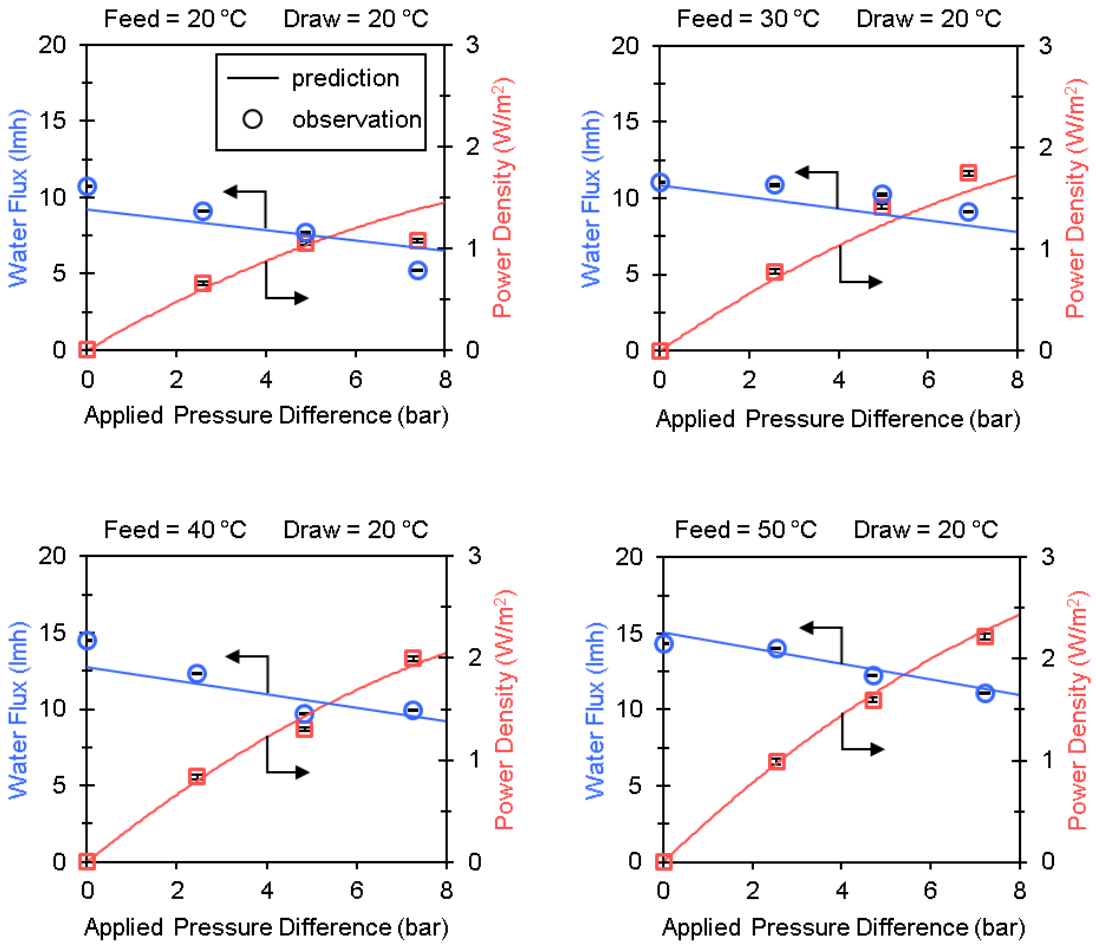

Figure 4.10 PRO water flux (left axis) and power density (right axis) with feed solution heated to a variety of temperatures. Experimental test conditions are specified in Table 4.2 and simulation input parameters are specified in Table 4.4.

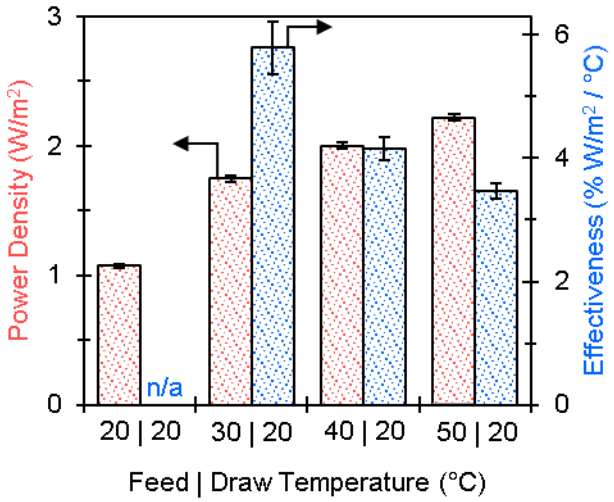

Figure 4.11 PRO power density (left axis) and effectiveness (right axis) at a variety of feed temperatures, given a draw temperature of 20 °C and an applied pressure difference of 7.5 bar. Effectiveness is a measure of the percent improvement in power per unit temperature change, relative to the baseline case at 20 °C. Experimental test conditions are specified in Table 4.2 and simulation input parameters are specified in Table 4.4.

Each of the six cases from Figures 4.9 and 4.11 are summarized in Figure 4.12, where they are listed in order of increasing number of degrees temperature change. If it is assumed that the feed and draw circulation rates are balanced, then the x-axis represents the amount of heat supplied to the system. As shown, the highest power is not necessarily achieved for the case in which the greatest amount of heat is supplied. For example, the case where T_F = 50 °C and T_D = 20 °C yields higher power and yet consumes less heat than the case where both $T_F = T_D$ = 40 °C. Similarly, the case where T_F = 30 °C and T_D = 20 °C yields more power than the case where T_F = 20 °C and T_D = 40 °C, despite the fact that the latter receives more heat. These illustrate that adding more heat to the system does not necessarily improve performance. Rather, a small amount of heat if applied strategically, can have a greater positive impact on power than a larger amount of heat. It

appears that to maximize power, heat should be concentrated towards the feed, and to maximize effectiveness, small amounts of heat should be used.

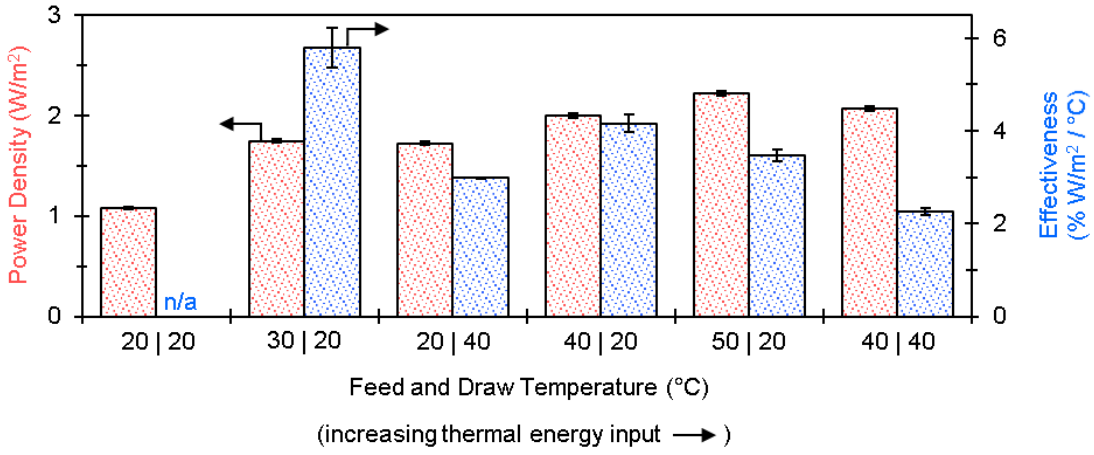

Figure 4.12 PRO power density (left axis) and effectiveness (right axis) at a variety of feed and draw, given an applied pressure difference of 7.5 bar. Effectiveness is a measure of the percent improvement in power per unit temperature change, relative to the baseline case at 20 °C. Experimental test conditions are specified in Table 4.2 and simulation input parameters are specified in Table 4.4.

4.5 Discussion

4.5.1 Why Heating Feed is Preferable to Heating Draw in Thermally-Enhanced PRO

To identify the fundamental transport mechanics that explain why hot feed performs better than hot draw, it is useful to compare the temperature profiles that form across the membrane under both scenarios. Figure 4.13 shows temperature and concentration across the active membrane as well as its support and boundary layers, as predicted by the numerical model that was experimentally validated. Several general profile features can be noted. For one, thermal gradients tend to be mostly linear, despite the fact that governing equations are non-linear. This indicates that heat transfer is driven

predominantly by thermal diffusion, which can be confirmed with additional analysis. The non-linearities that would be induced by heat carried by salt and mass flux is not significant in the illustrated scenarios. The salt concentration gradient on the other hand is characterized by a non-linear profile, indicating that salt transfer is driven by both diffusion as well as mass transport as it is carried by water flux.

Of further interest, is that Figure 4.13 illustrates an important difference in the temperature of the membrane depending on which fluid is heated. During PRO the active layer is oriented towards the draw solution, so it might be expected that the membrane temperature would approach the bulk draw temperature, but that is not the case. When only feed is heated to 40 °C, the active membrane temperature is 32.9 °C, whereas when draw is heated, the active membrane temperature is significantly less at only 27.7 °C. This is the result of more severe temperature polarization that is observed on the draw side of the membrane, caused by the large thermal resistance of the draw-side thermal boundary layer. In contrast, the feed-side thermal boundary layer is well mixed, owing to the presence of a spacer and to the pressure-induced deformation of the membrane which acts to reduce the feed flow channel, and therefore the feed-side thermal resistance is minimal. The temperature of this active membrane layer is critical because the apparent membrane permeability will be mostly a function of the fluid viscosity in and around the active membrane. For example, in the cases illustrated in Figure 4.13, membrane temperatures and the resulting fluid viscosity will yield apparent membrane water permeabilities of 0.531 lmh/bar when feed is heated, and only 0.476 lmh/bar when draw is heated.

A second dynamic that is also illustrated in Figure 4.13, is that having a hot feed appears to mitigate concentration polarization more than does a hot draw. As shown, not only is the active membrane warmer with a hot feed, but so are the membrane support and boundary layers. These cause a beneficial increase in salt diffusivity in these critical regions and ultimately reduce polarization. For example, when feed is heated to 40 °C, the effective concentration difference across the active membrane is 29.0 g/l, whereas when draw is heated, the effective concentration difference is slightly less at 28.2 g/l. Although not as significant as the previously mentioned effect on membrane permeability, the reduced polarization is nonetheless beneficial and again favors heating feed rather than draw.

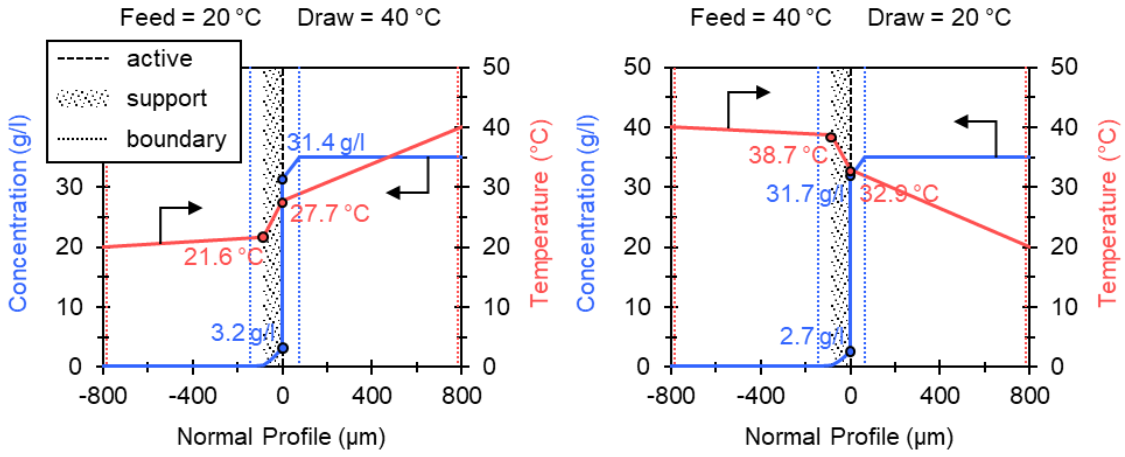

Figure 4.13 Concentration profile (left axis) and temperature profile (right axis) across the active membrane and its support and boundary layers, when either the draw solution or feed solution are heated. Simulation input parameters are specified in Table 4.4.

4.5.2 Effective Operation at Low Temperatures is Confirmed Throughout the Literature

To confirm the trends observed in this study, the effectiveness results are compared to data reported elsewhere in the literature, as shown in Figure 4.14. Because thermal effectiveness is a new metric that we are proposing, the referenced results shown here are calculated based upon published power density data. As shown, the effectiveness of 5.79 % W/m^2 / °C obtained in this study is among the highest so far achieved in the literature, with the exception of recent results reported by Wang et al. [150]. In general, we observe from both this study and more widely throughout the literature that heating PRO feed is more effective than heating draw [151,153,155]. Results also consistently show that heat is most effective when used to only slightly increase operating temperatures for example to 30 °C, while larger increases in temperature to 40 and 50 °C are usually associated with lower effectiveness.

More difficult to reconcile are the recent results by Wang et al. [150], which report very large effectiveness of up to 9.0 % W/m^2 / °C when both feed and draw are heated to 30 °C. It is likely that these effectiveness results are inflated by the very high cross-flow velocities of 44–89 cm/s that were used in their experimental trials. For comparison, the cross-flow velocities in our study were maintained at only ~ 15 cm/s. Very high circulation rates will mitigate axial variations in temperature by reducing residence time of fluid in the membrane module, and thereby help to maintain high source temperatures over the whole membrane area. In contrast, low circulation rates and high residence times will be characterized by significant temperature drops along the length of the membrane, in which case much of the benefit of heating the source fluids is lost. This observation raises the interesting point that increasing the temperature of a rapidly circulating fluid

requires much more thermal energy than for a slowly circulating fluid, and therefore comparing the performance results strictly in terms of the feed and draw temperatures provides only a limited characterization of the process. For future study, we suggest considering the efficiency of the process in terms of the change in power output relative to the required thermal energy input, across a range of operating temperatures and circulation rates.

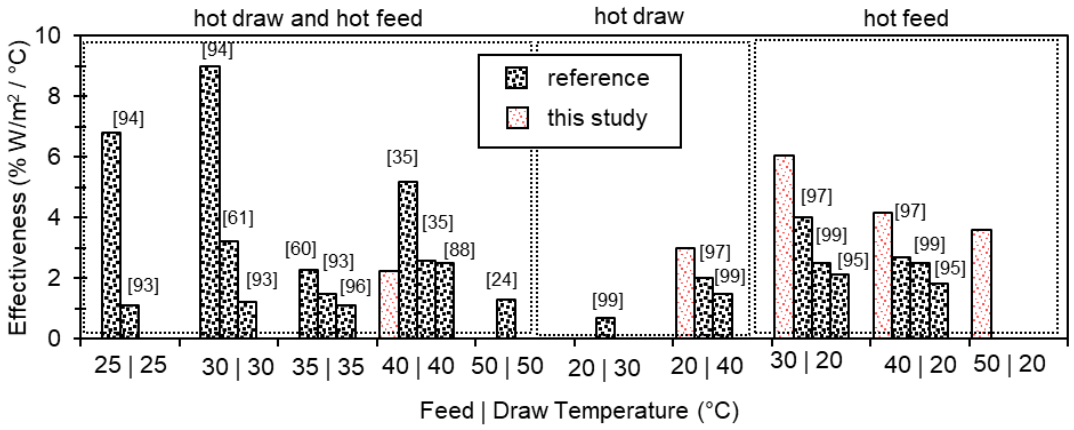

Figure 4.14 Effectiveness results obtained from this study as compared to results published throughout the literature. Effectiveness is a measure of the percent improvement in power per unit temperature change, relative to the baseline case at 20 °C.

4.6 Conclusions

In this study we have demonstrated the concept of using heat to thermally-enhance osmotic power. In general, adding thermal energy to increase operating temperature of either the feed or draw solutions was shown to significantly increase water flux and power generation by osmosis. A maximum increase of more than 110 % was achieved

when feed temperature is increased from 20 to 50 °C (given an applied pressure difference of 7.5 bar).

Results also show that heating feed solution improves performance much more than heating draw. For example, heating feed to 40 °C yields almost 40 % higher power than does heating draw to the same temperature. To explain this difference, theoretical transport dynamics were analyzed with the help of a detailed finite element transport model which was developed. Analysis of temperature and concentration gradients across the membrane and its boundary layers confirm the following:

Thermally-enhanced osmosis occurs primarily as a function of the warmer active membrane temperatures.

Membrane permeability increases with temperature, not because of any thermally-induced changes to the membrane morphology itself, but rather because warmer fluid in this critical region will have lower viscosity and therefore face less resistance in permeating across the membrane.

During PRO, hot feed solution will tend to produce a warmer membrane than hot draw, because the feed side boundary layer offers relatively little thermal resistance. This is attributed to the presence of a spacer in the feed channel, and the compression of the feed channel due to applied pressure, both of which will tend to increase mixing, reduce the thickness of the boundary layer, and increase the convective heat transfer coefficient. These conditions are unique to PRO, which helps to explain why FO results are less consistent, with certain studies instead showing a preference for heating draw.

Analysis was also done to compare the effectiveness of operating at different temperatures. A new metric was introduced which normalizes change in power density

over change in feed and draw solution temperatures. A maximum effectiveness of 5.8 % W/m^2 / °C was achieved at low feed solution temperatures of 30 °C. This analysis provides some insight into how thermal energy input can be optimized, and suggests that low temperatures may provide the greatest benefit to power for only a small amount of heat.

To further clarify the preferred operating temperatures of thermally enhanced PRO, we suggest that future work consider the energy balance between thermal energy input and PRO power output. This energy balance should be analyzed in not only thermodynamic terms, but also economic terms, with consideration for the fact that thermal energy is often of lesser value than mechanical or electrical power output. In addition, one of the important distinctions that should be considered in future work, is that thermal energy input will be a function of not only temperature but also of circulation flow rates (i.e. $\dot{Q} = \dot{m}\, c_p\, \Delta T$). For example, circulating high temperature fluid at low flow rates may require the same thermal energy input as circulating low temperature fluid at high flow rates, and yet some combination of these operating parameters may optimize efficiency. In our previous work on PRO, we showed that careful adjustment of feed flow rate, draw flow rate, and applied pressure is necessary to optimize the net power output of a PRO system [186,224]. Likewise, we expect that careful control of these three variables, in addition now to the feed and draw temperatures, is needed to optimize the net power output and efficiency of thermally-enhanced PRO.

It is hoped that abundant and cheap sources of thermal energy can be integrated into osmotic processes to improve the sustainability of future water and power systems and infrastructure.

4.7 Nomenclature

A	water permeability (m^3 s^{-1} m^{-2} Pa^{-1})
a	membrane area (m^2)
B	salt permeability (m^3 s^{-1} m^{-2})
c	concentration (kg m^{-3})
c_p	specific heat capacity (J kg^{-1} K^{-1})
D	diffusivity (m^2 s^{-1})
d	depth (m)
d_h	hydraulic diameter (m)
h	convection coefficient (W m^{-2} K^{-1})
i	number of ions
J_w	water flux (m^3 s^{-1} m^{-2})
J_s	salt flux (kg s^{-1} m^{-2})
K	mass transfer coefficient (m s^{-1})
k	thermal conductivity (W m^{-1} K^{-1})
l	length (m)
M	molar mass (kg mol^{-1})
m	mass (kg)
$\dot{m}$	mass flow rate
N	number of elements
n	normal position (m)
Nu	Nusselt number
p	pressure (Pa)
Pr	Prandtl number
$\dot{Q}$	heat transfer rate (W)
$\dot{q}$	heat flux (W m^{-2})

R	gas constant (J mol^{-1} K^{-1})
Re	Reynolds number
S	structure parameter (m)
Sc	Schmidt number
Sh	Sherwood number
T	temperature (K)
t	thickness (m)
u	velocity (m s^{-1})
V	volume (m^3)
$\dot{W}$	power (W)
w	width (m)

Greek symbols:

δ	concentration boundary thickness (m)
δ_t	thermal boundary thickness (m)
ε	porosity
η	effectiveness
μ	dynamic viscosity (Pa s)
π	osmotic pressure (Pa)
ρ	density (kg m^{-3})

Subscripts:

D	draw
F	feed
m	membrane
p	permeate
S	support structure
s	salt
w	water

4.8 Supplementary Notes

4.8.1 Supplementary Note 4.1: Membrane Salt Permeability as a Function of Salt Diffusivity

Adding heat to the PRO process will increase the membrane's apparent permeability to salt [71,144,151,154,155,157,169,171,172,174,175,181]. Importantly, most of the observed increase in salt permeability will be due to changes in the fluid properties, rather than any thermally induced changes in the membrane structure itself [172,175]. It has previously been suggested that salt permeability B is directly proportional to temperature T and inversely proportional to viscosity μ, as described in equation (S4.1) [152]. Since salt diffusivity D is proportional to T / μ [154,178,225], the membrane salt permeability can also be described as a function of salt diffusivity D, as described in equation (S4.3).

$$B = B_o \frac{T}{T_o} \frac{\mu_o}{\mu} \tag{S4.1}$$

$$D \propto \frac{T}{\mu} \tag{S4.2}$$

$$B = B_o \frac{D}{D_o} \tag{S4.3}$$

Figure S4.1 shows a collection of salt permeability results at a range of temperatures, as collected from the literature. Equations (S4.1) and (S4.3) are also plotted and show similar agreement with experimental data.

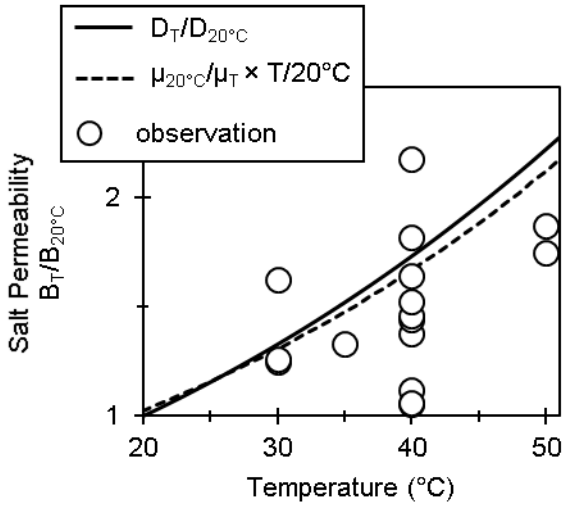

Figure S4.1 Membrane salt permeability as a function of temperature can be predicted from the proportional change in solution viscosity as described in equation (S4.1), or from the proportional change in salt diffusivity as described in equation (S4.3). Both models for membrane salt permeability are compared against experimental data from the literature [71,144,154,171,172,174,175,181].

4.8.2 Supplementary Note 4.2: Membrane Water Permeability

Membrane characterization followed standard test procedures [186,206]. To find the membrane's water permeability *A*, a reverse osmosis test was conducted with deionized feed water, and the rate of observed water permeate was normalized over the applied pressure. Figure S4.2 shows the raw data collected and Table S4.1 provides an outline of how raw data is analyzed, including how experimental uncertainty propagates throughout the analysis.

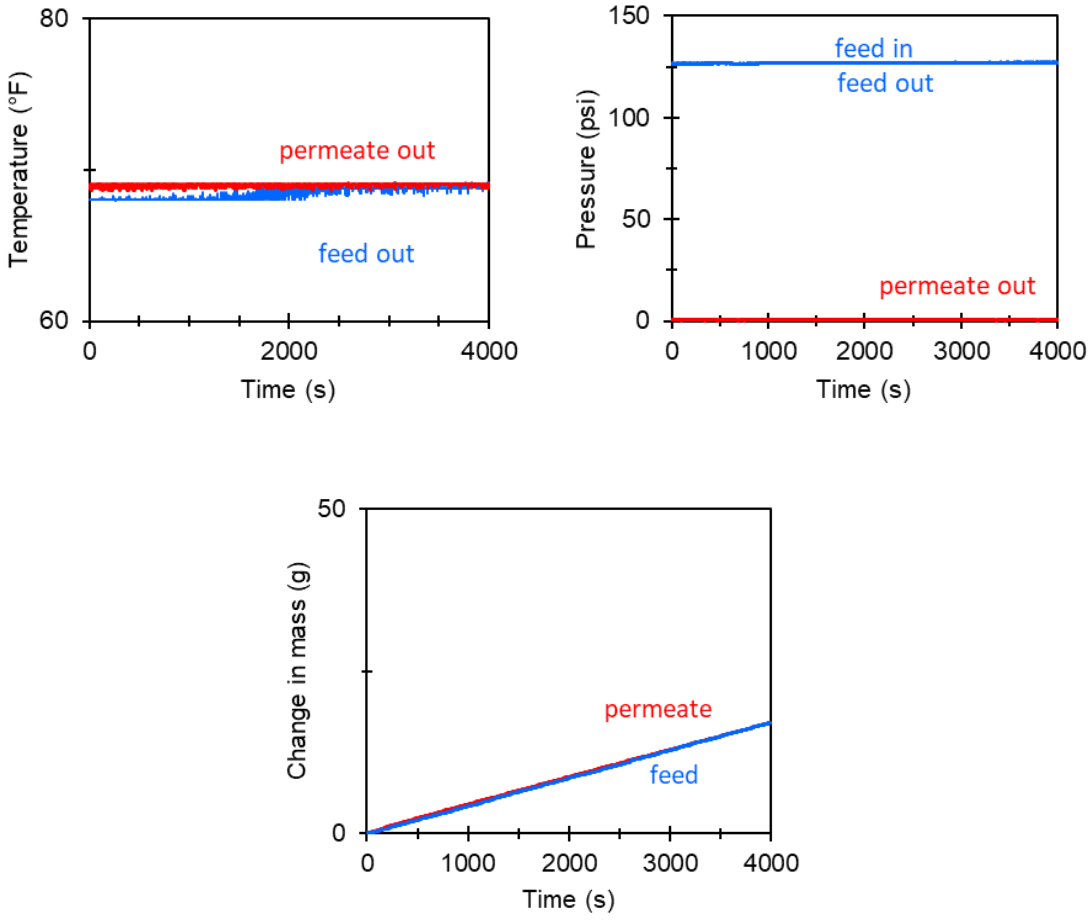

Figure S4.2 Raw test data for characterization of membrane water permeability. (a) Temperature measured by transmitters (800-200-1-1-8-8-040-6 RTD, Noshok (Berea, OH), 200 ± 0.837 °F). (b) Pressure measured by transmitters (EW-68075-50, Cole-Parmer (Vernon Hills, IL), 250 ± 0.625 psi). (c) Change in mass measured by scales (AX8201, Ohaus (Parsippany, NJ), 8000 ± 0.2 g).

Table S4.1 Analysis of test results for characterization of membrane water permeability.

Parameter	Value	Measurement or Analysis
Preparation of feed solution		
Feed water mass m_F	3000 ± 0.2 g	Mass balance, AX8201, Ohaus (Parsippany, NJ), 8000 ± 0.2 g

Table S4.1—Continued

Calibration of feed flow rate		
Change in feed mass Δm	1142.6 ± 0.282 g	Mass balance, AX8201, Ohaus (Parsippany, NJ), 8000 ± 0.2 g
Change in time Δt	204 ± 1 s	Stopwatch
Feed flow rate $\dot{V}_F$	0.336 ± 0.004 lpm	$\dot{V}_F = \frac{\Delta m}{\Delta t\, \rho}$, $\frac{\delta \dot{V}_F}{\dot{V}_F} = \sqrt{\left(\frac{\delta \Delta m}{\Delta m}\right)^2 + \left(\frac{\delta \Delta t}{\Delta t}\right)^2}$ ρ = 998.7 kg/m^3
Average trial measurements		
Feed temperature T_F	20.23 ± 0.465 °C	Temperature transmitter, 800-200-1-1-8-8-040-6 RTD, Noshok (Berea, OH), 200 ± 0.837 °F
Permeate temperature T_P	20.55 ± 0.465 °C	Temperature transmitter, 800-200-1-1-8-8-040-6 RTD, Noshok (Berea, OH), 200 ± 0.837 °F
Feed pressure at inlet $p_{F,in}$	8.769 ± 0.043 bar	Pressure transmitter, EW-68075-50, Cole-Parmer (Vernon Hills, IL), 250 ± 0.625 psi
Feed pressure at outlet $p_{F,out}$	8.725 ± 0.043 bar	Pressure transmitter, EW-68075-50, Cole-Parmer (Vernon Hills, IL), 250 ± 0.625 psi
Feed pressure p_F	8.748 ± 0.061 bar	$p_F = \frac{p_{F,in} + p_{F,out}}{2}$, $\frac{\delta p_F}{p_F} = \sqrt{\left(\frac{\delta p_{F,in}}{p_{F,in}}\right)^2 + \left(\frac{\delta p_{F,out}}{p_{F,out}}\right)^2}$
Permeate pressure p_P	0.031 ± 0.043 bar	Pressure transmitter, EW-68075-50, Cole-Parmer (Vernon Hills, IL), 250 ± 0.625 psi
Pressure difference Δp	8.716 ± 0.075 bar	$\Delta p = p_F - p_P$, $\delta \Delta p = \sqrt{\delta p_F{}^2 + \delta p_P{}^2}$
Water permeate analysis		
Change in feed mass Δm_F	17 ± 0.2 g	Mass balance, AX8201, Ohaus (Parsippany, NJ), 8000 ± 0.2 g
Change in permeate mass Δm_P	17.1 ± 0.2 g	Mass balance, AX8201, Ohaus (Parsippany, NJ), 8000 ± 0.2 g
Change in mass Δm	17.05 ± 0.282 g	$\Delta m = \frac{\Delta m_F + \Delta m_P}{2}$, $\frac{\delta \Delta m}{\Delta m} = \sqrt{\left(\frac{\delta \Delta m_F}{\Delta m_F}\right)^2 + \left(\frac{\delta \Delta m_P}{\Delta m_P}\right)^2}$

Table S4.1—Continued

Water permeate analysis		
Parameter	Value	Measurement or Analysis
Change in time Δt	4000 ± 1 s	Stopwatch
Water permeate flux J_w	3.66 ± 0.06 lmh	$J_w = \frac{\Delta m}{a\,\rho\,\Delta t}$, $\frac{\delta J_w}{J_w} = \sqrt{\left(\frac{\delta \Delta m}{\Delta m}\right)^2 + \left(\frac{\delta \Delta t}{\Delta t}\right)^2}$ a =0.0042 m^2 , ρ = 998.7 kg/m^3
Water permeability A	0.42 ± 0.01 lmh/bar	$A = \frac{J_w}{\Delta p}$, $\frac{\delta A}{A} = \frac{\delta \Delta p}{\Delta p} + \frac{\delta J_w}{J_w}$

4.8.3 Supplementary Note 4.3: Membrane Salt Permeability

Membrane characterization followed standard test procedures [186,206]. To find the membrane's salt permeability *B*, a reverse osmosis test was conducted with low concentration feed solution, and the resulting permeate concentration was observed. Figure S4.3 shows the raw data collected and Table S4.2 provides an outline of how raw data is analyzed, including how experimental uncertainty propagates throughout the analysis.

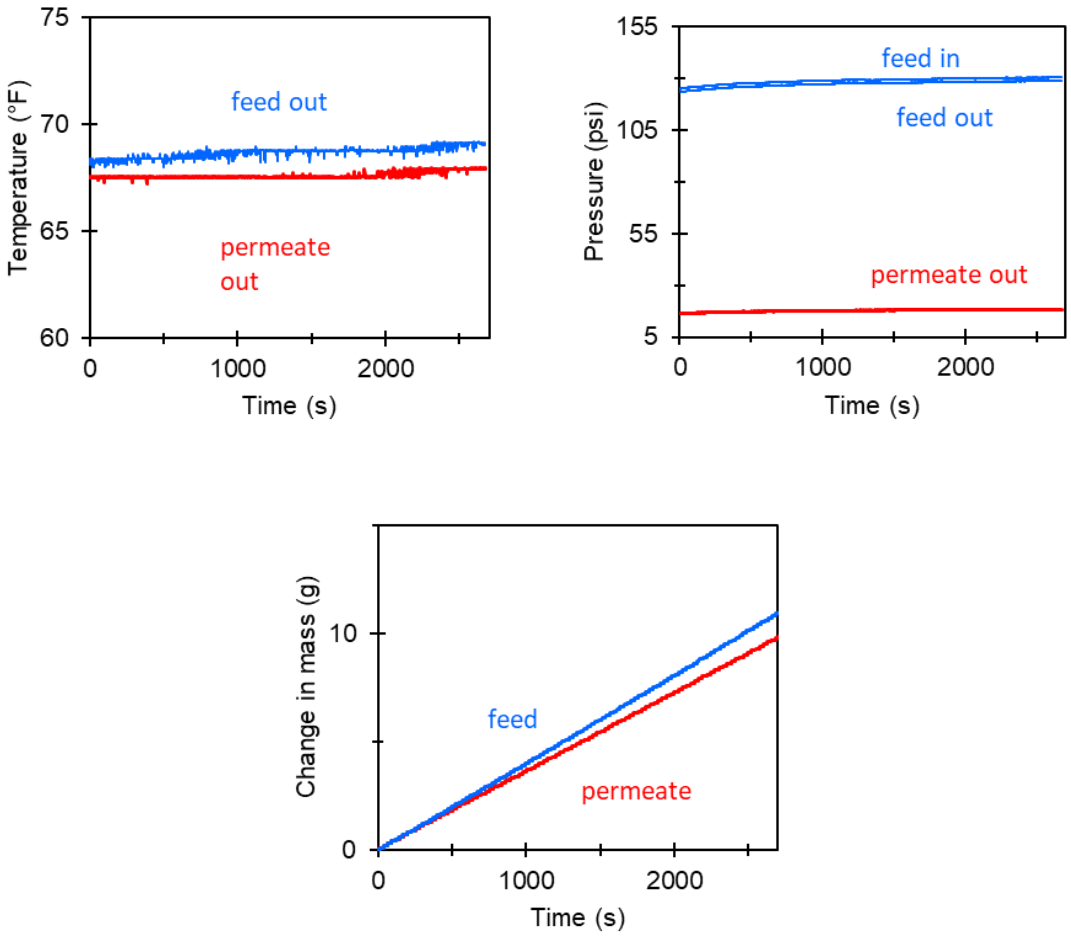

Figure S4.3 Raw test data for characterization of membrane salt permeability. (a) Temperature measured by transmitters (800-200-1-1-8-8-040-6 RTD, Noshok (Berea, OH), 200 ± 0.837 °F). (b) Pressure measured by transmitters (EW-68075-50, Cole-Parmer (Vernon Hills, IL), 250 ± 0.625 psi). (c) Change in mass measured by scales (AX8201, Ohaus (Parsippany, NJ), 8000 ± 0.2 g).

Table S4.2 Analysis of test results for characterization of membrane salt permeability.

Parameter	Value	Measurement or Analysis
Preparation of feed solution		
Feed water mass $m_{F,w}$	4563.6 ± 0.2 g	Mass balance, AX8201, Ohaus (Parsippany, NJ), 8000 ± 0.2 g
Feed salt mass $m_{F,s}$	9.2 ± 0.2 g	Mass balance, AX8201, Ohaus (Parsippany, NJ), 8000 ± 0.2 g
Feed concentration c_F	2 ± 0.04 g/l	$c_F = \frac{m_{F,s}}{m_{F,w}} \rho$, $\frac{\delta c_F}{c_F} = \sqrt{\left(\frac{\delta m_{F,w}}{m_{F,w}}\right)^2 + \left(\frac{\delta m_{F,s}}{m_{F,s}}\right)^2}$ ρ = 1000 kg/m^3
Calibration of feed flow rate		
Change in feed mass Δm	1081.9 ± 0.282 g	Mass balance, AX8201, Ohaus (Parsippany, NJ), 8000 ± 0.2 g
Change in time Δt	193 ± 1 s	Stopwatch
Feed flow rate $\dot{V}_F$	0.336 ± 0.002 lpm	$\dot{V}_F = \frac{\Delta m}{\Delta t \rho}$, $\frac{\delta \dot{V}_F}{\dot{V}_F} = \sqrt{\left(\frac{\delta \Delta m}{\Delta m}\right)^2 + \left(\frac{\delta \Delta t}{\Delta t}\right)^2}$ ρ = 1000 kg/m^3
Average trial measurements		
Feed temperature T_F	20.378 ± 0.465 °C	Temperature transmitter, 800-200-1-1-8-8-040-6 RTD, Noshok (Berea, OH), 200 ± 0.837 °F
Permeate temperature T_P	19.781 ± 0.465 °C	Temperature transmitter, 800-200-1-1-8-8-040-6 RTD, Noshok (Berea, OH), 200 ± 0.837 °F
Feed pressure at inlet pF,in	8.894 ± 0.043 bar	Pressure transmitter, EW-68075-50, Cole-Parmer (Vernon Hills, IL), 250 ± 0.625 psi
Feed pressure at outlet pF,out	8.781 ± 0.043 bar	Pressure transmitter, EW-68075-50, Cole-Parmer (Vernon Hills, IL), 250 ± 0.625 psi
Feed pressure p_F	8.838 ± 0.061 bar	$p_F = \frac{p_{F,in} + p_{F,out}}{2}$, $\frac{\delta p_F}{p_F} = \sqrt{\left(\frac{\delta p_{F,in}}{p_{F,in}}\right)^2 + \left(\frac{\delta p_{F,out}}{p_{F,out}}\right)^2}$

Table S4.2—Continued

Parameter	Value	Measurement or Analysis
Permeate pressure p_P	1.221 ± 0.043 bar	Pressure transmitter, EW-68075-50, Cole-Parmer (Vernon Hills, IL), 250 ± 0.625 psi
Pressure difference Δp	7.617 ± 0.075 bar	$\Delta p = p_F - p_P$, $\delta\Delta p = \sqrt{\delta {p_F}^2 + \delta {p_P}^2}$
Water permeate analysis		
Change in feed mass Δm_F	25.6 ± 0.2 g	Mass balance, AX8201, Ohaus (Parsippany, NJ), 8000 ± 0.2 g
Change in permeate mass Δm_P	23.2 ± 0.2 g	Mass balance, AX8201, Ohaus (Parsippany, NJ), 8000 ± 0.2 g
Change in mass Δm	24.4 ± 0.282 g	$\Delta m = \frac{\Delta m_F + \Delta m_P}{2}$, $\frac{\delta \Delta m}{\Delta m} = \sqrt{\left(\frac{\delta \Delta m_F}{\Delta m_F}\right)^2 + \left(\frac{\delta \Delta m_P}{\Delta m_P}\right)^2}$
Change in time Δt	6291 ± 1 s	Stopwatch
Water permeate flux J_w	3.32 ± 0.04 lmh	$J_w = \frac{\Delta m}{a\, \rho\, \Delta t}$, $\frac{\delta J_w}{J_w} = \sqrt{\left(\frac{\delta \Delta m}{\Delta m}\right)^2 + \left(\frac{\delta \Delta t}{\Delta t}\right)^2}$ a = 0.0042 m^2 , ρ = 1000 kg/m^3
Salt permeate analysis		
Permeate conductivity σ_P	497.5 ± 20 µS/cm	Conductivity probe, CDCE-90-1 Omega, (Norwalk, CT), 10000 ± 20µS
Permeate concentration c_p	0.23 ± 0.02 g/l	$c_P = f\, \sigma_P$, $\frac{\delta c_P}{c_P} = \sqrt{\left(\frac{\delta \sigma_P}{\sigma_P}\right)^2 + \left(\frac{\delta f}{f}\right)^2}$ f = 0.000452 ± 0.0000278 by linear interpolation of Table S4.3
Salt rejection R	0.89 ± 0.07	$R = 1 - \frac{c_P}{c_F}$, $\frac{\delta R}{R} = \sqrt{\left(\frac{\delta c_P}{c_P}\right)^2 + \left(\frac{\delta c_F}{c_F}\right)^2}$

Table S4.2—Continued

Parameter	Value	Measurement or Analysis
Salt permeability B	0.40 ± 0.05 lmh	$B = J_w \left(\frac{1-R}{R}\right) \exp\left(-\frac{J_w}{K}\right)$, $\delta B = \left\lvert \frac{1-R}{R}\left(-\exp\left(-\frac{J_w}{K}\right)\frac{J_w}{K}\right) - \frac{1-R}{R}\exp\left(-\frac{J_w}{K}\right)\right\rvert \delta J_w + \left\lvert \frac{-1}{R^2} J_w \exp\left(-\frac{J_w}{K}\right)\right\rvert \delta R$ $K = 0.0000201$ m/s

Table S4.3 Calibration of conductivity versus concentration.

Parameter	Value	Measurement or Analysis
Sample 1		
Salt mass m_s	10 ± 0.2 g	Mass balance, AX8201, Ohaus (Parsippany, NJ), 8000 ± 0.2 g
Water mass m_w	50000 ± 0.2 g	Mass balance, AX8201, Ohaus (Parsippany, NJ), 8000 ± 0.2 g
Concentration c	0.2 ± 0.004 g/l	$c = \frac{m_s}{m_w}\rho$, $\frac{\delta c}{c} = \sqrt{\left(\frac{\delta m_s}{m_s}\right)^2 + \left(\frac{\delta m_w}{m_w}\right)^2}$
Conductivity σ	441.2 ± 20 µS/cm	Conductivity probe, CDCE-90-1 Omega, (Norwalk, CT), 10000 ± 20µS
Conversion factor f	0.000453 ± 0.0000296	$f = \frac{c_P}{\sigma_P}$, $\frac{\delta f}{f} = \sqrt{\left(\frac{\delta c_P}{c_P}\right)^2 + \left(\frac{\delta \sigma_P}{\sigma_P}\right)^2}$
Sample 2		
Salt mass m_s	10 ± 0.2 g	Mass balance, AX8201, Ohaus (Parsippany, NJ), 8000 ± 0.2 g
Water mass m_w	33330 ± 0.2 g	Mass balance, AX8201, Ohaus (Parsippany, NJ), 8000 ± 0.2 g

Table S4.3—Continued

Parameter	Value	Measurement or Analysis
Concentration c	0.3 ± 0.0006 g/l	$c = \frac{m_s}{m_w}\rho$, $\frac{\delta c}{c} = \sqrt{\left(\frac{\delta m_s}{m_s}\right)^2 + \left(\frac{\delta m_w}{m_w}\right)^2}$
Conductivity σ	667.7 ± 20 μS/cm	Conductivity probe, CDCE-90-1 Omega, (Norwalk, CT), 10000 ± 20 μS
Conductivity σ	0.000449 ± 0.0000224	$f = \frac{c_P}{\sigma_P}$, $\frac{\delta f}{f} = \sqrt{\left(\frac{\delta c_P}{c_P}\right)^2 + \left(\frac{\delta \sigma_P}{\sigma_P}\right)^2}$

4.8.4 Supplementary Note 4.4: Membrane Structure Parameter

Membrane characterization followed standard test procedures [186,206]. To find the membrane's structure parameter *S*, a forward osmosis test was conducted, and the resulting permeate concentration was observed. Figure S3.4 shows the raw data collected and Table S4.4 provides an outline of how raw data is analyzed, including how experimental uncertainty propagates throughout the analysis.

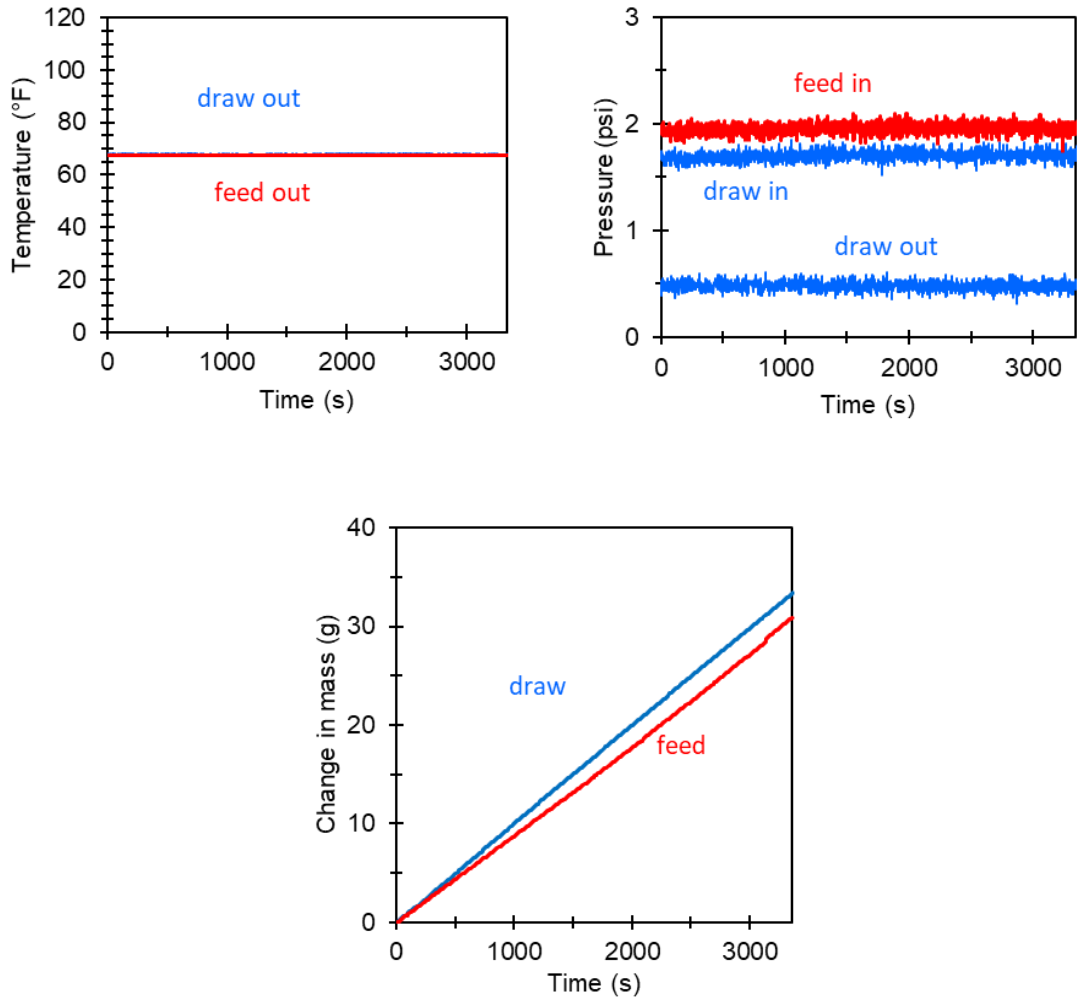

Figure S4.4 Raw test data for characterization of membrane structure parameter. (a) Temperature measured by transmitters (800-200-1-1-8-8-040-6 RTD, Noshok (Berea, OH), 200 ± 0.837 °F). (b) Pressure measured by transmitters (EW-68075-50, Cole-Parmer (Vernon Hills, IL), 250 ± 0.625 psi). (c) Change in mass measured by scales (AX8201, Ohaus (Parsippany, NJ), 8000 ± 0.2 g).

Table S4.4 Analysis of test results for characterization of membrane structure parameter.

Parameter	Value	Measurement or Analysis
Preparation of feed solution and draw solution		
Feed water mass $m_{F,w}$	3343.3 ± 0.2 g	Mass balance, AX8201, Ohaus (Parsippany, NJ), 8000 ± 0.2 g
Feed salt mass $m_{F,s}$	0	Mass balance, AX8201, Ohaus (Parsippany, NJ), 8000 ± 0.2 g
Feed concentration c_F	0	$c_F = \frac{m_{F,s}}{m_{F,w}}\rho$, $\frac{\delta c_F}{c_F} = \sqrt{\left(\frac{\delta m_{F,w}}{m_{F,w}}\right)^2 + \left(\frac{\delta m_{F,s}}{m_{F,s}}\right)^2}$ ρ = 998.7 kg/m^3
Draw water mass $m_{D,w}$	3115.3 ± 0.2 g	Mass balance, AX8201, Ohaus (Parsippany, NJ), 8000 ± 0.2 g
Draw salt mass $m_{D,s}$	175.4 ± 0.2 g	Mass balance, AX8201, Ohaus (Parsippany, NJ), 8000 ± 0.2 g
Draw concentration c_D	58.44 ± 0.001 g/l	$c_D = \frac{m_{D,s}}{m_{D,w}}\rho$, $\frac{\delta c_D}{c_D} = \sqrt{\left(\frac{\delta m_{D,w}}{m_{D,w}}\right)^2 + \left(\frac{\delta m_{D,s}}{m_{D,s}}\right)^2}$ ρ = 1037.7 kg/m^3
Calibration of feed flow rate and draw flow rate		
Change in feed mass Δm_F	229.8 ± 0.282 g	Mass balance, AX8201, Ohaus (Parsippany, NJ), 8000 ± 0.2 g
Change in time Δt	47 ± 1 s	Stopwatch
Feed flow rate $\dot{V}_F$	0.293 ± 0.02 lpm	$\dot{V}_F = \frac{\Delta m_F}{\Delta t\,\rho}$, $\frac{\delta \dot{V}_F}{\dot{V}_F} = \sqrt{\left(\frac{\delta \Delta m_F}{\Delta m_F}\right)^2 + \left(\frac{\delta \Delta t}{\Delta t}\right)^2}$ ρ = 998.7 kg/m^3
Change in draw mass Δm_D	451.2 ± 0.282 g	Mass balance, AX8201, Ohaus (Parsippany, NJ), 8000 ± 0.2 g
Change in time Δt	100 ± 1 s	Stopwatch

Table S4.4—Continued

Parameter	Value	Measurement or Analysis
Draw flow rate $\dot{V}_D$	0.260 ± 0.01 lpm	$\dot{V}_D = \frac{\Delta m_D}{\Delta t\, \rho}$, $\frac{\delta \dot{V}_D}{\dot{V}_D} = \sqrt{\left(\frac{\delta \Delta m_D}{\Delta m_D}\right)^2 + \left(\frac{\delta \Delta t}{\Delta t}\right)^2}$ ρ = 1037.7 kg/m^3
Average trial measurements		
Feed temperature T_F	19.87 ± 0.465 °C	Temperature transmitter, 800-200-1-1-8-8-040-6 RTD , Noshok (Berea, OH), 200 ± 0.837 °F
Draw temperature T_D	19.74 ± 0.465 °C	Temperature transmitter, 800-200-1-1-8-8-040-6 RTD , Noshok (Berea, OH), 200 ± 0.837 °F
Feed pressure at inlet p_F	0.134 ± 0.043 bar	Pressure transmitter, EW-68075-50, Cole-Parmer (Vernon Hills, IL), 250 ± 0.625 psi
Draw pressure at inlet $p_{D,in}$	0.117 ± 0.043 bar	Pressure transmitter, EW-68075-50, Cole-Parmer (Vernon Hills, IL), 250 ± 0.625 psi
Draw pressure at outlet $p_{D,out}$	0.033 ± 0.043 bar	Pressure transmitter, EW-68075-50, Cole-Parmer (Vernon Hills, IL), 250 ± 0.625 psi
Draw pressure p_D	0.075 ± 0.061 bar	$p_D = \frac{p_{D,in} + p_{D,out}}{2}$, $\frac{\delta p_D}{p_D} = \sqrt{\left(\frac{\delta p_{D,in}}{p_{D,in}}\right)^2 + \left(\frac{\delta p_{D,out}}{p_{D,out}}\right)^2}$
Pressure difference Δp	- 0.059 ± 0.074 bar	$\Delta p = p_F - p_P$, $\delta \Delta p = \sqrt{\delta p_F{}^2 + \delta p_D{}^2}$
Water permeate analysis		
Change in feed mass Δm_F	30.9± 0.2 g	Mass balance, AX8201, Ohaus (Parsippany, NJ), 8000 ± 0.2 g
Change in draw mass Δm_D	33.4 ± 0.2 g	Mass balance, AX8201, Ohaus (Parsippany, NJ), 8000 ± 0.2 g
Change in mass Δm	32.15 ± 0.282 g	$\Delta m = \frac{\Delta m_F + \Delta m_D}{2}$, $\frac{\delta \Delta m}{\Delta m} = \sqrt{\delta \Delta m_F{}^2 + \delta \Delta m_D{}^2}$
Change in time Δt	3364 ± 1 s	Stopwatch

Table S4.4—Continued

Parameter	Value	Measurement or Analysis
Water permeate flux J_w	8.04 ± 0.05 lmh	$J_w = \frac{\Delta m}{a\,\rho\,\Delta t}$, $\frac{\delta J_w}{J_w} = \sqrt{\left(\frac{\delta \Delta m}{\Delta m}\right)^2 + \left(\frac{\delta \Delta t}{\Delta t}\right)^2}$ $a = 0.042\ m^2$, $\rho = 1018.2\ kg/m^3$
Structure parameter analysis		
Feed osmotic pressure π_F	0	$\pi_F = i_F\,R\,T_F\,c_F$, $\frac{\delta \pi_F}{\pi_F} = \sqrt{\left(\frac{\delta T_F}{T_P}\right)^2 + \left(\frac{\delta c_F}{c_F}\right)^2}$ $i_F = 2$, $R = 8.314\ J/kg/mol$
Draw osmotic pressure π_D	48.7 ± 1.1 bar	$\pi_D = i_D\,R\,T_D\,c_D$, $\frac{\delta \pi_D}{\pi_D} = \sqrt{\left(\frac{\delta T_D}{T_D}\right)^2 + \left(\frac{\delta c_D}{c_D}\right)^2}$ $i_D = 2$, $R = 8.314\ J/kg/mol$
Structure parameter S	607 ± 83.2 μm	$S = \frac{D}{J_w} \ln\left(\frac{B + A\,\pi_D}{B + J_w + A\,\pi_F}\right)$, $\delta S = \frac{D}{J_w}\left(\left\lvert\frac{1}{B + J_w + A\,\pi_F}\right\rvert \delta J_w + \left\lvert\frac{1}{J_w}\,\frac{B + A\,\pi_D}{B + J_w + A\,\pi_F}\right\rvert \delta J_w + \left\lvert\frac{J_w + A\,(\pi_F - \pi_D)}{(B + J_w + A\,\pi_F)^2}\right\rvert \delta B + \left\lvert\frac{J_w\,\pi_D + B\,(\pi_F - \pi_D)}{(B + J_w + A\,\pi_F)^2}\right\rvert \delta A + \left\lvert\frac{A}{B + J_w + A\,\pi_F}\right\rvert \delta \pi_D + \left\lvert\left(\Delta\Gamma_{F,b}.\frac{J_w + A\,(B + A\,\pi_D)}{(B + J_w + A\,\pi_F)^2}\right)\right\rvert \delta \pi_F\right)$ $D = 1.5\times10^{-9}\ m^2/s$

4.8.5 Supplementary Note 4.5: Sample PRO Test

PRO water flux and power density was evaluated by measuring the change in feed and draw volume over time in response to a range of applied pressures and temperatures. Figure S4.5 shows the raw data collected and Table S4.5 provides an outline of how raw data is analyzed, including how experimental uncertainty propagates throughout the analysis.

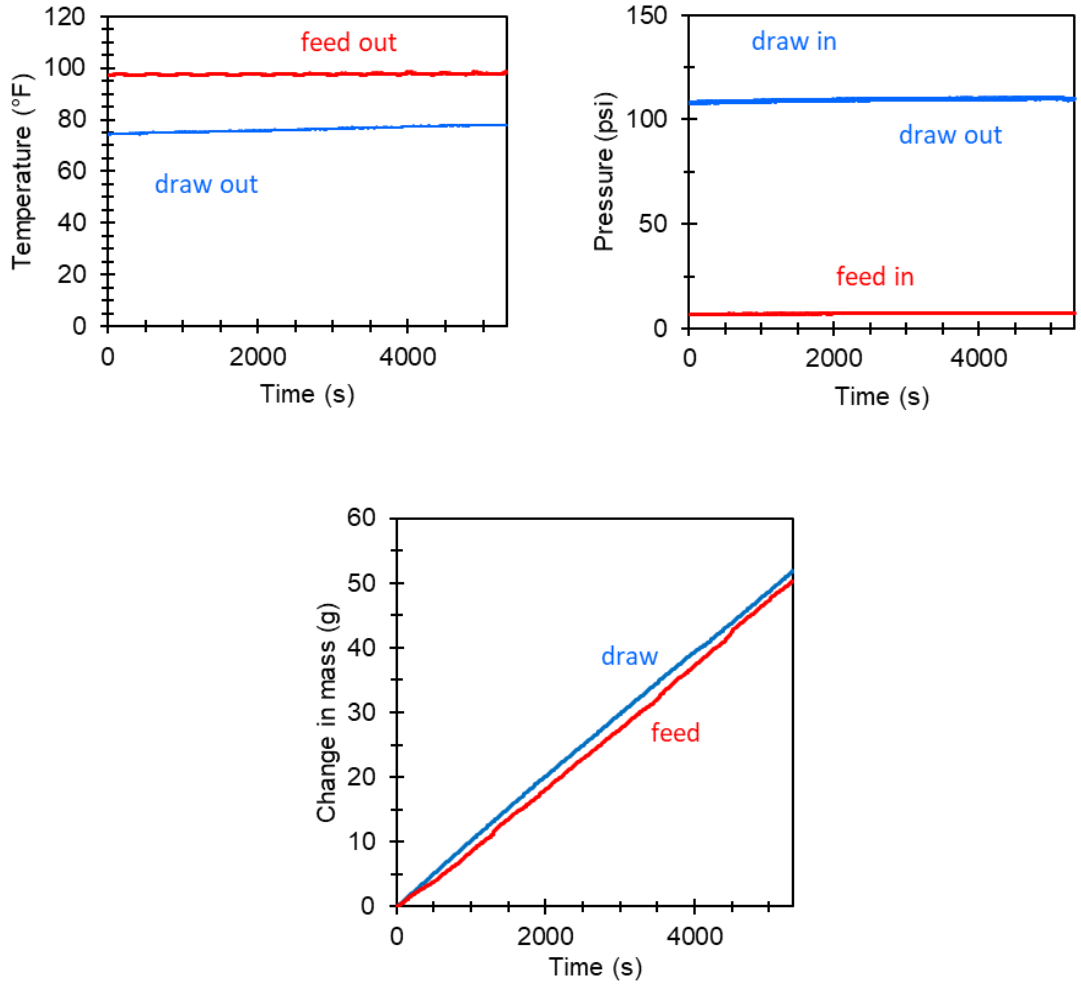

Figure S4.5 Raw test data for a PRO test. (a) Temperature measured by transmitters (800-200-1-1-8-8-040-6 RTD, Noshok (Berea, OH), 200 ± 0.837 °F). (b) Pressure measured by transmitters (EW-68075-50, Cole-Parmer (Vernon Hills, IL), 250 ± 0.625 psi). (c) Change in mass measured by scales (AX8201, Ohaus (Parsippany, NJ), 8000 ± 0.2 g).

Table S4.5 Analysis of test results for PRO test

Parameter	Value	Measurement or Analysis
Preparation of feed solution and draw solution		
Feed water mass $m_{F,w}$	7066.3 ± 0.2 g	Mass balance, AX8201, Ohaus (Parsippany, NJ), 8000 ± 0.2 g
Feed salt mass $m_{F,s}$	0.7 ± 0.2 g	Mass balance, AX8201, Ohaus (Parsippany, NJ), 8000 ± 0.2 g
Feed concentration c_F	0.1 ± 0.03g/l	$c_F = \frac{m_{F,s}}{m_{F,w}}\rho$, $\frac{\delta c_F}{c_F} = \sqrt{\left(\frac{\delta m_{F,w}}{m_{F,w}}\right)^2 + \left(\frac{\delta m_{F,s}}{m_{F,s}}\right)^2}$ ρ = 992.4 kg/m^3
Draw water mass $m_{D,w}$	6901.2 ± 0.2 g	Mass balance, AX8201, Ohaus (Parsippany, NJ), 8000 ± 0.2 g
Draw salt mass $m_{D,s}$	241.5 ± 0.2 g	Mass balance, AX8201, Ohaus (Parsippany, NJ), 8000 ± 0.2 g
Draw concentration c_D	35.8 ± 0.03 g/l	$c_D = \frac{m_{D,s}}{m_{D,w}}\rho$, $\frac{\delta c_D}{c_D} = \sqrt{\left(\frac{\delta m_{D,w}}{m_{D,w}}\right)^2 + \left(\frac{\delta m_{D,s}}{m_{D,s}}\right)^2}$ ρ = 1022.4 kg/m^3
Calibration of feed flow rate and draw flow rate		
Change in feed mass Δm_F	627.3 ± 0.2 g	Mass balance, AX8201, Ohaus (Parsippany, NJ), 8000 ± 0.2 g
Change in time Δt	125 ± 1 s	Stopwatch
Feed flow rate $\dot{V}_F$	0.303 ± 0.002 lpm	$\dot{V}_F = \frac{\Delta m_F}{\Delta t\,\rho}$, $\frac{\delta \dot{V}_F}{\dot{V}_F} = \sqrt{\left(\frac{\delta \Delta m_F}{\Delta m_F}\right)^2 + \left(\frac{\delta \Delta t}{\Delta t}\right)^2}$ ρ = 992.4 kg/m^3
Change in draw mass Δm_D	425.1 ± 0.2 g	Mass balance, AX8201, Ohaus (Parsippany, NJ), 8000 ± 0.2 g
Change in time Δt	90 ± 1 s	Stopwatch

Table S4.5—Continued

Parameter	Value	Measurement or Analysis
Draw flow rate $\dot{V}_D$	0.277 ± 0.01 lpm	$\dot{V}_D = \frac{\Delta m_D}{\Delta t\, \rho}$, $\frac{\delta \dot{V}_D}{\dot{V}_D} = \sqrt{\left(\frac{\delta \Delta m_D}{\Delta m_D}\right)^2 + \left(\frac{\delta \Delta t}{\Delta t}\right)^2}$ ρ = 1022.4 kg/m^3
Average trial measurements		
Feed temperature T_F	36.155 ± 0.465 °C	Temperature transmitter, 800-200-1-1-8-8-040-6 RTD, Noshok (Berea, OH), 200 ± 0.837 °F
Draw temperature T_D	23.494 ± 0.465 °C	Temperature transmitter, 800-200-1-1-8-8-040-6 RTD, Noshok (Berea, OH), 200 ± 0.837 °F
Feed pressure at inlet p_F	0.491 ± 0.043 bar	Pressure transmitter, EW-68075-50, Cole-Parmer (Vernon Hills, IL), 250 ± 0.625 psi
Draw pressure at inlet $p_{D,in}$	7.566 ± 0.043 bar	Pressure transmitter, EW-68075-50, Cole-Parmer (Vernon Hills, IL), 250 ± 0.625 psi
Draw pressure at outlet $p_{D,out}$	7.504 ± 0.043 bar	Pressure transmitter, EW-68075-50, Cole-Parmer (Vernon Hills, IL), 250 ± 0.625 psi
Draw pressure p_D	7.535 ± 0.061 bar	$p_D = \frac{p_{D,in} + p_{D,out}}{2}$, $\frac{\delta p_D}{p_D} = \sqrt{\left(\frac{\delta p_{D,in}}{p_{D,in}}\right)^2 + \left(\frac{\delta p_{D,out}}{p_{D,out}}\right)^2}$
Pressure difference Δp	7.044 ± 0.074 bar	$\Delta p = p_F - p_P$, $\delta \Delta p = \sqrt{\delta p_F{}^2 + \delta p_D{}^2}$
Water permeate analysis		
Change in feed mass Δm_F	50.3 ± 0.2 g	Mass balance, AX8201, Ohaus (Parsippany, NJ), 8000 ± 0.2 g
Change in draw mass Δm_D	51.8 ± 0.2 g	Mass balance, AX8201, Ohaus (Parsippany, NJ), 8000 ± 0.2 g
Change in mass Δm	51.05 ± 0.282 g	$\Delta m = \frac{\Delta m_F + \Delta m_D}{2}$, $\frac{\delta \Delta m}{\Delta m} = \sqrt{\delta \Delta m_F{}^2 + \delta \Delta m_D{}^2}$
Change in time Δt	3364 ± 1 s	Stopwatch

Table S4.5—Continued

Parameter	Value	Measurement or Analysis
Water permeate flux J_w	8.16 ± 0.05 lmh	$J_w = \frac{\Delta m}{a\,\rho\,\Delta t}$, $\frac{\delta J_w}{J_w} = \sqrt{\left(\frac{\delta \Delta m}{\Delta m}\right)^2 + \left(\frac{\delta \Delta t}{\Delta t}\right)^2}$ a =0.0042 m^2, ρ = 1007.35 kg/m^3
Power density $\dot{W}$	1.58 ± 0.01 W/m^2	$\dot{W} = J_w\,\Delta p$, $\frac{\delta \dot{W}}{\dot{W}} = \sqrt{\left(\frac{\delta J_w}{J_w}\right)^2 + \left(\frac{\delta \Delta p}{\Delta p}\right)^2}$

4.8.6 Supplementary Note 4.6: Numerical Model Validation

Experimental data from our test trials of thermally-enhanced PRO is used to verify the accuracy of the proposed numerical transport model. Figure S4.6 shows the comparison between predicted and observed water vapor flux for a total of 24 data points. Agreement is satisfactory with a shown to be satisfactory with a coefficient of determination R^2 = 0.88, as defined in equation (S4.4).

$$R^2 = \left(\frac{24.\Sigma(xy) - (\Sigma x.\Sigma y)}{\sqrt{(24.\Sigma x^2 - (\Sigma x)^2) \times (24.\Sigma y^2 - (\Sigma y)^2)}}\right)^2 \quad \text{(S4.4)}$$

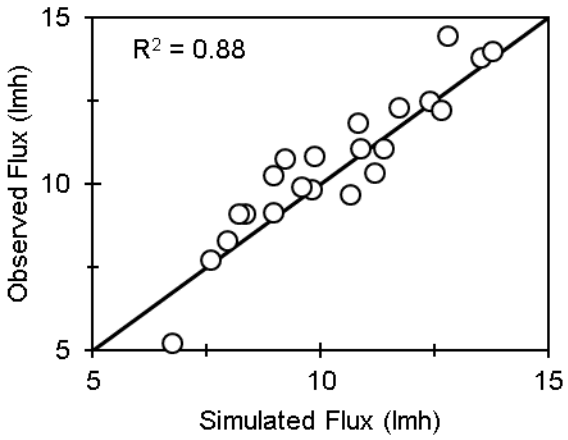

Figure S4.6 Comparison between water vapor flux that is experimentally observed from test trials of thermally-enhanced pressure retarded osmosis, and that is predicted by numerical simulation with the developed transport model

4.8.7 Supplementary Note 4.7: Effectiveness

Effectiveness introduced in Section 4.3.2, equation (4.13), can be expressed using a different approach as shown in equation (S4.5). Here the effectiveness is calculated as the increase in power density with respect to amount of heat added with respect to baseline case.

$$\eta = \frac{\dot{W} - \dot{W}_{20\,^{\circ}C}}{\dot{m}_F\, cp_F \left(T_F - T_{F,20\,^{\circ}C}\right) + \dot{m}_D\, cp_D \left(T_D - T_{D,20\,^{\circ}C}\right)} \tag{S4.5}$$

Where c_{pF} and c_{pD} are the specific heat capacity of feed solution and draw solution respectively.

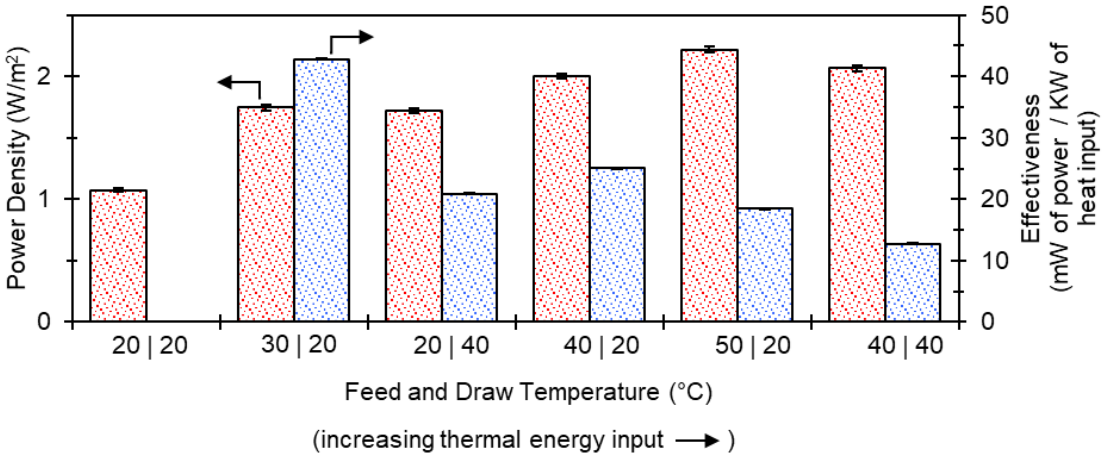

Figure S4.7 PRO power density (left axis) and effectiveness (right axis) at a variety of feed and draw, given an applied pressure difference of 7.5 bar. Effectiveness is a measure of the improvement in power measured in mW with respect to amount of heat added in KW calculated using equation (S4.5). Experimental test conditions are specified in Table 4.2 and simulation input parameters are specified in Table 4.4.

The effectiveness introduced in Section 4.3.2, equation (4.13)) can be expressed using a different approach, as shown in equation (S4.5). Here, the effectiveness is calculated as the increase in power density divided by the amount of heat added with respect to the baseline case.

The results from this approach agree with the findings in Section 4.5.2. Heating feed to 40 ℃ is 20% more effective than heating draw to the same temperature. It is also more effective compared to heating both solutions to 40 ℃. Heating the feed to 50 ℃ is 45% more effective than heating both solutions to 40 ℃ with hot feed having an effectiveness of 25.1 mW/KW and the latter having an effectiveness value of 12.7 mW/KW.

When comparing the hot feed at 50 °C to the hot feed at 30 °C, it is observed that lower temperatures are more effective, which is in agreement with the previous findings. Hot feed at 30 °C is 57% more effective than hot feed at 50 °C.

Comparing the hot draw with the case when both solutions were heated, the hot draw was 39% more effective than the latter.

The magnitude of the effectiveness results are quite low because of the high mass flow rates used. Circulating high temperature fluid at low flow rates may require the same thermal energy input as circulating low temperature fluid at high flow rates. This is discussed in Section 4.6. Optimizing the mass flow rate along with the operating temperature is necessary to effectively use the heat. In addition, the experimental bench used in this study does not have a heat recovery device that can recycle heat from the outlet streams of the feed and draw and return it to the inlets. Incorporating a heat recovery device can reduce the need to supply heat to the inlet and thereby greatly increase the effectiveness. Depending on the efficiency of the heat recovery device, the required heat input can become negligible.

CHAPTER FIVE
REDUCING THE SPECIFIC ENERGY USE OF SEAWATER DESALINATION WITH THERMALLY ENHANCED REVERSE OSMOSIS

5.1 Introduction

In recent years, there has been renewed interest in harnessing thermal energy for water desalination [226]. Thermal energy from sources such as solar radiation, ocean thermal gradients, geothermal, and power plant waste heat is abundant and represents a tremendous resource for improving the sustainability of water infrastructure. This has led to advances and innovation in a number of thermally-driven desalination technologies, such as membrane distillation [227], multi-flash distillation [228], and thermally-driven RO [44]. In all such technologies, heat is used as the primary energy source and driver. Alternatively, the possibility of using heat to thermally enhance RO has also been considered, wherein small amounts of heat could be used to pre-heat RO feed water in order to improve RO performance [73,229].

The concept of thermally-enhanced RO is largely motivated by the fact that warmer feed water permeates more quickly across a RO membrane [130,180,230,231], making it possible to produce more water with a given unit of mechanical work. For example, some studies have shown mechanical energy savings of up to 12 % when seawater feed is heated from 15 to 45 °C, and up to 45 % when brackish water feed is heated from 15 to

---

Chapter Five is based primarily on a paper that was published in the Desalination Journal.

S. Yagnambhatt, S. Khanmohammaddi, J. Maisonneuve, "Reducing the Specific Energy Use of Seawater Desalination with Thermally Enhanced Reverse Osmosis," Desalination, Vol. 573: 117163, 2024. DOI: 10.1016/j.desal.2023.117163.

45 °C [73,231]. This is mostly the result of an apparent increase in the membrane permeability that is caused by lower feed viscosity as a function of temperature [152,180]. The other advantage of warm feed is that high permeability facilitates operation at lower applied pressures, which is helpful for mitigating the risks of membrane mechanical failure and membrane fouling [230,232]. For these reasons, it is generally agreed that RO operation in warm climates is favorable [231,233] . However, it is less clear whether it is advantageous to use an external source of thermal energy to pre-heat RO feed water. In such a case, the energy savings from reduced pumping work (and associated cost savings) would need to outweigh the thermal energy input (and associated costs). To date, this balance between thermal energy input and mechanical pump savings for thermally-enhanced RO has not yet been considered in the literature. Also unclear is whether the energy saving benefits of thermally-enhanced RO outweigh the disadvantages, including increased reverse salt flux and permeate concentration, loss of membrane structural integrity, and increased scaling [230,231].

In this chapter, we investigate the process of thermally-enhanced RO and analyze the tradeoff between thermal energy input and mechanical pump savings. A transport model is developed and used to establish the energy balance of both conventional RO and thermally-enhanced RO. This is the first time that thermal energy input has been included in the overall energy balance analysis of thermally-enhanced RO. Parametric analysis is conducted across a range of conditions to identify under what circumstances the resulting energy balance is favorable. RO application to a number of different feed water sources is considered, including seawater, brackish water, and oil and gas produced water. Other variables include different membrane properties (permeability and selectivity), different

operating targets (water permeate rates and feed recovery ratios), different equipment specifications (thermal and mechanical efficiencies), and different environmental conditions (ambient temperatures). Recommendations are provided for future applications of thermally-enhanced RO.

5.2 Theory

5.2.1 Energy Balance of Reverse Osmosis

In a standard RO system, concentrated feed solution is introduced to a membrane module and then pressurized (above the osmotic pressure) to drive clean water permeate across the membrane for collection. A standard RO system is illustrated in Figure 5.1. The energy consumption of RO is related to the pumping power that is required to pressurize feed solution above its osmotic pressure potential. To reduce this pumping load and improve energy efficiency, pressure from the super-concentrated waste brine is typically recycled back to the incoming feed via a mechanical pressure exchanger.

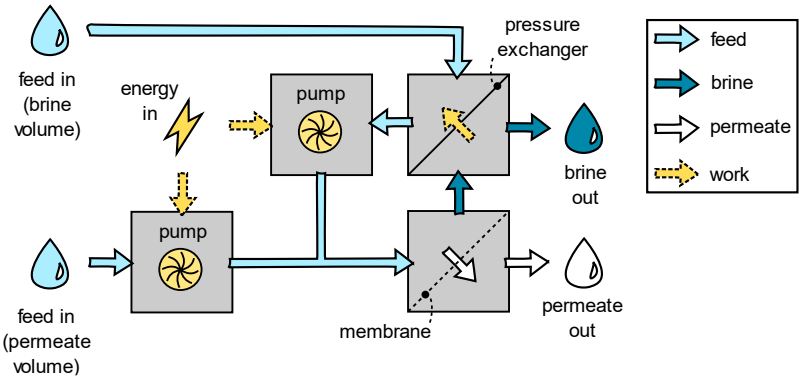

Figure 5.1 Schematic of a standard reverse osmosis (RO) desalination plant. Energy is supplied for mechanical pumping to pressurize feed solution above its osmotic potential, and thereby drive clean water permeate across the membrane.

The energy efficiency of RO can be conveniently expressed in terms of specific energy e_{RO}, which is defined as the energy use E_{RO} per unit volume of water permeate that is collected V_P. As described in equation (5.1) and as illustrated in Figure 5.1, the pumping load can be distributed between two pumps, with one to handle a portion of the feed equal to the permeate volume, and another to handle a portion equal to the brine volume. This configuration facilitates integration of the pressure exchanger for recovering mechanical energy from the pressurized brine solution and recycling it back to the incoming feed. The energy requirements of both of these pumps, e_P and e_B, are defined in equations (5.2) and (5.3), and a detailed derivation of both expressions is provided in Supplementary Note 5.1.

$$\mathrm{e_{RO}} = \frac{\mathrm{E_{RO}}}{\mathrm{V_P}} = \mathrm{e_P} + \mathrm{e_B} \tag{5.1}$$

$$\mathrm{e_P} = \frac{1}{\eta_{\mathrm{pump}}} \Delta \mathrm{p} \tag{5.2}$$

$$\mathrm{e_B} = \frac{1}{\eta_{\mathrm{pump}}} \left(\frac{1}{\mathrm{r}} - 1\right) \Delta \mathrm{p} \left(1 - \eta_{\mathrm{pex}}\right) \tag{5.3}$$

Where η_{pump} is the pump efficiency, and η_{pex} is the efficiency of the pressure exchanger, R is the recovery ratio, which is the ratio of the permeate volume relative to the feed volume (i.e. $r = V_P / V_F$), and Δp is the applied pressure.

Applied pressure Δp is an operating parameter that can be controlled to achieve certain targets for the RO plant. For example, it may be desirable for the RO plant to achieve a high recovery ratio so that excessive volumes of feed are not handled, although this will increase the specific energy use, as shown later on. Or it may be desirable for the RO

plant to maintain a certain rate of water permeate production per unit of membrane surface area, which will be proportional to the plant's return on investment, also shown later on. The relationship between applied pressure and these targets is defined in equation (5.4), and an expanded derivation is provided Supplementary Note 5.2.

$$\Delta p = \frac{\dot{V}_P}{a} A^{-1} + \Delta\pi \tag{5.4}$$

Where $\dot{V}_P / a$ is the rate of permeate water production per unit membrane surface area, A is the membrane water permeability, and $\Delta\pi$ is the osmotic pressure difference across the membrane, which can be approximated with the Van't Hoff equation.

$$\Delta\pi = i R T \Delta c \tag{5.5}$$

Where i is the number of ions, R is the gas constant, T is the absolute temperature, and Δc is the concentration difference across the membrane.

Importantly, concentration difference Δc will vary along the length of the membrane as water permeate is recovered from the feed and as salt leaks through the imperfect membrane. It will also be a function of polarization, as non-linear concentration gradients will develop normal to the membrane surface due to limited diffusivity. To account for these dynamics, a variety of 2D and 3D finite element models have been proposed in the literature [234–236]. A simplified expression is used here to describe concentration difference Δc as a function of the logarithmic mean of the concentration from inlet to outlet, and as a function of an exponential polarization factor [237–239].

$$\Delta c = \exp\left(\frac{\dot{V}_P}{a} k^{-1}\right)\left(\frac{c_B - c_F}{\ln c_B - \ln c_F}\right) - c_P \tag{5.6}$$

Where k is the mass transfer coefficient, and c_F, c_B, and c_P are concentrations of the feed, brine, and permeate respectively. While the inlet concentration c_F is set by the seawater feed source, the outlet concentrations for brine c_B and permeate c_P will be a function of the balance between water and salt permeate. Expressions for these can be developed by taking a mass balance of salt and water permeate, and by considering the diffusion mechanism by which salt leaks towards the permeate. Expressions for both c_B and c_P are provided below, and a detailed derivation is provided in Supplementary Note 5.3.

$$\mathrm{c_B} = \frac{\mathrm{c_F} - \mathrm{r\,c_P}}{1 - \mathrm{r}} \tag{5.7}$$

$$\mathrm{c_P} = \frac{\mathrm{a}}{\dot{\mathrm{V}}_\mathrm{P}}\,\mathrm{B}\,\Delta\mathrm{c} \tag{5.8}$$

Where B is the membrane salt permeability.

Together, equations (5.1)-(5.8) describe the energy efficiency of a reverse osmosis system e_{RO} as a function of (i) the properties of the feed solution including concentration c_F and temperature T, (ii) the properties of the membrane including water and salt permeability A and B, (iii) the severity of polarization, which is related to the mass transfer coefficient k, and (iv) the target recovery ratio and permeate flux, r and $\dot{V}_P / a$. For reference, the thermodynamic limit of RO can be obtained from equations (5.1)-(5.8) by assuming no losses $p_{loss} = 0$, perfect pump and pressure exchanger efficiency $\eta_{pump} = \eta_{pex} = 1$, no reverse salt leakage $B = 0$, no polarization $\mathrm{k} \to \infty$, and a target recovery ratio and permeate rate of zero, $r \to 0$ and $\dot{V}_P / a \to 0$.

5.2.2 Energy Balance of Thermally-Enhanced Reverse Osmosis

In a thermally-enhanced RO system, concentrated feed solution is heated prior to being introduced to the membrane module. This decreases fluid viscosity, allowing clean water to permeate across the membrane more rapidly. Energy savings are thus achieved as lower applied pressures (and hence less pumping work) are needed to achieve the target water permeate rates. Pumping work is therefore partially displaced by thermal energy. A thermally-enhanced RO system is illustrated in Figure 5.2. As shown, thermal energy can be efficiently managed by recovering it from the brine and permeate volumes, and then recycling it back to the incoming feed via heat exchangers.

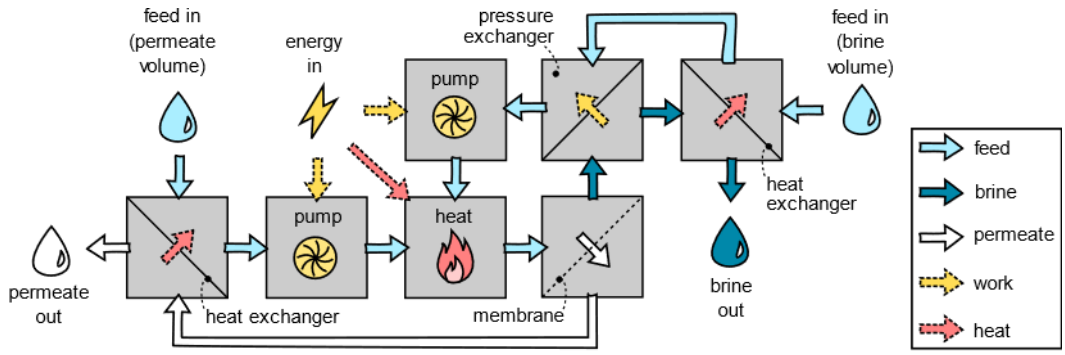

Figure 5.2 Schematic of a thermally-enhanced RO plant designed to use heat to reduce the required mechanical pump work. Other configurations are also possible so that incoming feed can either be heated first or pressurized first.

The overall energy balance of thermally-enhanced RO, is therefore the sum of the reduced mechanical pumping work and the added thermal energy. This is expressed in equation (5.9) which shows the overall specific energy balance of thermally-enhanced RO $e_{TE\text{-}RO}$ as a function of the coefficient of performance *cop*, used to relate the specific

thermal energy q to the mechanical work of RO e_{RO}. The specific thermal energy input q is defined in equation (5.10) as a function of the temperature to which feed is heated ΔT and the efficiency with which heat is recycled η_{Tex}. A detailed derivation of this energy balance is provided in Supplementary Note 5.4.

$$e_{TE-RO} = e_{RO} + \frac{q}{cop} \tag{5.9}$$

$$q = \frac{\dot{Q}}{\dot{V}_P} = \frac{1}{r}\, \rho\, c_p \Delta T\, (1 - \eta_{hex}) \tag{5.10}$$

Where ρ and c_p are the density and specific heat capacity of the feed. Note that the coefficient of performance for an ideal heat pump operating at its thermodynamic limit, $cop = T / \Delta T$. Also note that in the ideal case, where ambient heat loss is eliminated considering heat is completely recycled $\eta_{hex} \rightarrow 1$, the thermal energy input is reduced to zero $q \rightarrow 0$.

The energy balance of thermally-enhanced RO is affected by several competing dynamics as illustrated in Figure 5.3, including (a) the apparent increase in membrane water permeability caused by changes in the fluid viscosity, (b) the decrease in concentration polarization caused by higher salt diffusivity, (c) the increase in osmotic pressure, and (d) the apparent increase in membrane salt permeability caused by higher salt diffusivity.

The energy savings from a thermally-enhanced RO system are achieved primarily from an increase in the apparent water permeability of the membrane that is observed in the presence of warm feed. This dynamic has been studied extensively throughout the literature, and it is generally agreed that much of the observed increase is the result of

reduced fluid viscosity, rather than because of any significant change in the membrane structure [149,152,180]. Equations (5.11) and (5.12) approximate the relationship between membrane water permeability A, feed viscosity μ, and feed temperature T [73,152,172]. The relationship is also illustrated in Figure 5.3 (a) which shows a near doubling of the membrane's apparent water permeability as feed is heated from 20 to 50 °C. Supplementary Note 5.5 provides additional supporting information about equation (5.11).

$$\mathrm{A} = \mathrm{A}_{20\,^{\circ}\mathrm{C}}\,\frac{\mu_{20\,^{\circ}\mathrm{C}}}{\mu} \tag{5.11}$$

$$\mu = 0.4599\,\exp(1.796 \times 10^{3}\,\mathrm{c} - 0.021\,\mathrm{T}) \tag{5.12}$$

To a lesser extent, thermally-enhanced RO also benefits from reduced concentration polarization. As shown in equations (5.13) and (5.14), the salt mass transfer coefficient k is directly proportional to the salt diffusivity D, which increases with temperature T [125,153,240]. Figure 5.3 (b) shows that k increases by almost 70 % from 20 to 50 °C. This helps to reduce the concentration difference across the membrane because the polarization factor is proportional to the exponent of k-1, as described previously in equation (5.6). This enables energy savings as target permeate flux can be achieved with lower applied pressures. It also reduces the driving force for undesirable salt leakage, which may assist in producing a lower concentration permeate water product, although other dynamics mitigate this benefit, as explained below.

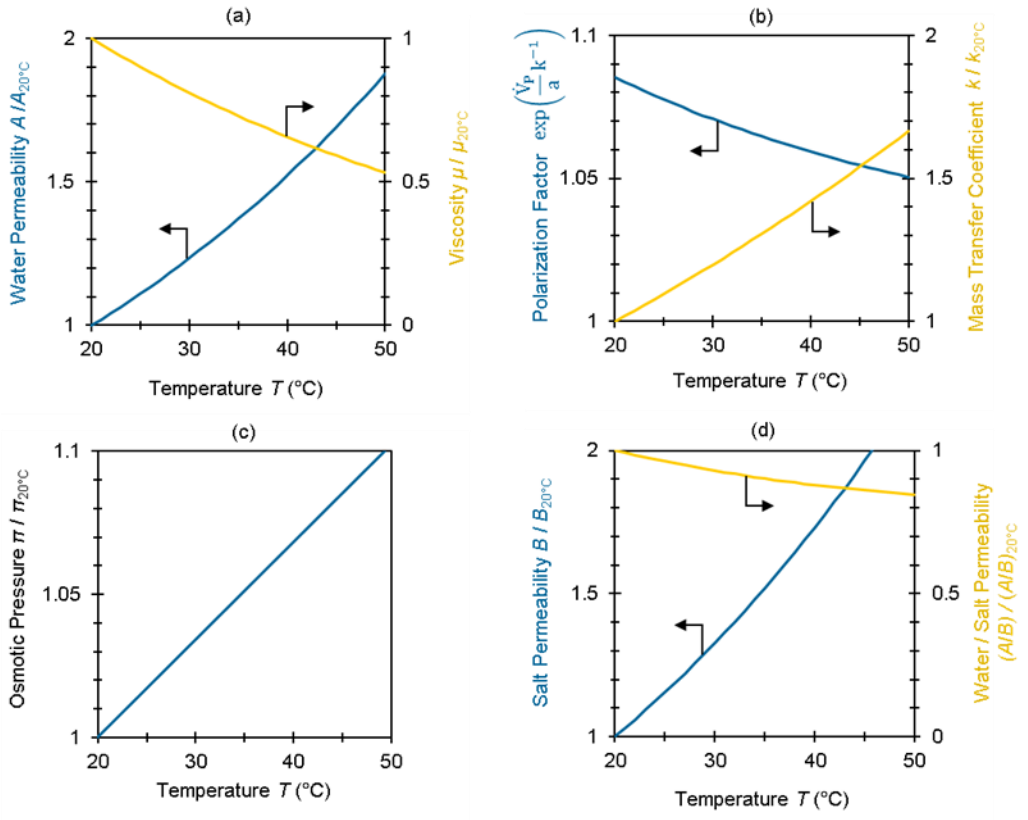

Figure 5.3 a) Membrane water permeability is inversely proportional to viscosity, as described in equations (11) and (12). (b) Concentration polarization factor exp ($\dot{V}_P/a\ k^{-1}$) and mass transfer coefficient as a function of temperature, as described in equation (5.13). (c) Osmotic pressure of feed as a function of temperature calculated using equation (5.5). (d) Membrane salt permeability as a function of temperature can be predicted from the proportional change in salt diffusivity, as described in equation (5.16). Input parameters and assumptions include feed concentration c = 35 g/l, feed flow velocity u = 0.1 m/s, hydraulic diameter d = 0.001 m, and water permeate flux $\dot{V}_P/a$ = 25 lmh.

$$k = D\,\frac{Sh}{d} \tag{5.13}$$

$$D = 6.725 \times 10^{-6} \exp\left(9.034 \times 10^{-3}\, c - \frac{2513}{T}\right) \tag{5.14}$$

$$\mathrm{Sh} = 0.46\,\mathrm{Re}^{0.36}\,\mathrm{Sc}^{0.36} \tag{5.15}$$

Where *Sh* is the Sherwood number and *d* is the hydraulic diameter. Various empirical equations have been proposed to described the Sherwood number in different RO membrane configurations, but it is generally described as a function of the Reynolds number *Re* and the Schmidt number *Sc* [209–211].

The benefits of thermally-enhanced RO are lessened by (i) an increase in the osmotic pressure difference as a function of feed temperature, and (ii) an increase in the salt permeability of the membrane. As described previously in equation (5.5), osmotic pressure is proportional to the absolute temperature of the feed. For example, Figure 5.3 (c) shows a 10 % increase in osmotic pressure as feed is heated from 20 to 50 °C. This increases the pumping pressure, and hence mechanical work, that must be applied in order to achieve the target water permeate rates, and therefore mitigates the energy savings of thermally-enhanced RO. Interestingly, there is some temperature that optimizes this tradeoff and yields the minimum specific energy of RO.

The second drawback of thermally-enhanced RO is the increase in membrane salt permeability that is associated with heat. This dynamic is well studied in the literature, and it is generally agreed that much of the perceived increase in salt permeability is due to the increase in salt diffusivity rather than any change in the membrane structure itself [148,149,151]. For this reason, the change in the apparent membrane salt permeability *B* can be approximated by the proportional change in salt diffusivity *D*, as expressed in equations (5.14) and (5.16). As illustrated in Figure 5.3 (d) salt diffusivity and hence salt permeability more than double as feed is heated from 20 to 50 °C. Because this increase

in salt permeability is greater than the increase in water permeability (reported previously in Figure 5.3 (a)), the ratio of water to salt permeability A/B drops by almost 20 % from 20 to 50 °C. This increase in B and this drop in A/B are certainly not desirable, but their significance can only be properly evaluated by considering their net effect on specific energy consumption and levelized cost of water. For example, it is very possible that a small change in A can be more significant than a large change in B. Supplementary Note 5.5 provides additional supporting information about equation (5.16).

$$\mathrm{B} = \mathrm{B}_{20\,^{\circ}\mathrm{C}}\ \frac{\mathrm{D}}{\mathrm{D}_{20\,^{\circ}\mathrm{C}}} \tag{5.16}$$

5.3 Methods

To evaluate the performance of thermally-enhanced RO an analytical model was developed in Excel 2019 software (Microsoft, Redmond WA) to solve the system of equations described in Section 5.1. This includes a simple numerical guess and check algorithm used to solve equations (5.6)-(5.8) to within < 0.01 % convergence error.

Performance was evaluated in terms of the specific work of RO e_{RO} and the overall specific energy balance of thermally-enhanced RO $e_{TE\text{-}RO}$ (given a certain heat pump coefficient of performance cop) as a function of operating temperature. For most commercial membranes, maximum recommended operating temperatures typically range from 35-40 °C, but recent publications have shown promising materials advances for high temperature operation well above typical values [232]. Therefore, a temperature range of 20 to 50 °C is considered here to provide a view of performance across both current and possible future operating conditions.

In general, the minimum specific energy was identified as a function of operating temperature, while respecting targets for recovery ratio r and permeate flux $\dot{V}_P / a$, and limits for permeate concentration c_P and applied pressure Δp. Performance was evaluated across a range of conditions including for a variety of common feed sources (brackish water, seawater, and oil and gas produced water, each approximated with NaCl concentrations of c_F = 10, 35, and 70 g/l respectively) and for a variety of membrane water permeabilities and salt selectivities (A = 0.5, 1, and 2 lmh/bar, and A/B = 5, 10, and 20 /bar). Table 5.1 defines the default modelling input conditions. Efficiency of mechanical equipment were assumed to be constant, although empirical expressions for efficiency as a function of temperature are available in the literature and can be included for more detailed analysis [73].

Table 5.1 Default case study conditions unless otherwise specified.

Operating Targets	
Permeate flux $\dot{V}_P / a$	25 lmh
Recovery ratio r	0.5
Operating Limits	
Applied pressure Δp	< 100 bar
Permeate concentration c_P	< 0.5 g/l
Feed Properties	
Solute	NaCl
Concentration c_F	35 g/l
Temperature T	20 °C
Velocity	0.1 m/s
Viscosity μ [185]	$0.4599 \exp(1.796\ \mathrm{c} - 0.021\ \mathrm{T})$

Table S4.5—Continued

Density ρ [130,182]	$1005 + 7.062 \times 10^5\ \mathrm{c} - 0.3148\ (\mathrm{T} - 273.15) - 824.3\ (\mathrm{T} - 273.15)\ \mathrm{c} - 3.783 \times 10^8\ \mathrm{c}^2$
Salt diffusivity D [125]	$6.725 \times 10^{-6} \exp\left(1.546 \times 10^{-4}\ \mathrm{c\ M} - 2513 / T\right)$
Membrane Properties	
Water permeability A	1 lmh/bar
Salt permeability B	0.1 lmh
Hydraulic diameter d	0.001 m
Equipment Efficiency	
Pump η_{pump}	0.8
Pressure exchanger η_{pex}	0.9
Heat exchanger η_{hex}	0.9
Coefficient of performance *cop*	$T / \Delta T$

5.4 Results

5.4.1 Energy Use of Reverse Osmosis for Seawater Desalination

Figure 5.4 shows the specific energy of RO e_{RO} for a common application of seawater desalination operated at ambient baseline temperature of T_o = 20 °C (input parameters and assumptions are provided in Table 5.1). As shown, specific energy can be minimized by balancing the recovery ratio. When recovery ratio is too high, feed water becomes very concentrated and as a result very large applied pressure (i.e. more energy) is required to maintain the target permeate rate. On the other hand, when the recovery ratio is too low, large volumes of brine need to be handled, and therefore any inefficiencies in the pressure exchanger are exacerbated and quickly lead to high energy use. When these competing dynamics are balanced, the minimum specific energy is obtained. For the scenarios shown, this is achieved at recovery between r = 0.3–0.5.

Energy efficiency is also shown to improve at low permeate flux because this allows for low applied pressures to be used. For example, the minimum specific energy in Figure 5.4, e_{RO} = 2.0 kWh/m^3 is achieved when the process is operated at low permeate rates of $\dot{V}_P / a$ = 10 lmh. Operation at even lower permeate flux would allow for even lower specific energy, and the thermodynamic limit of seawater desalination of 0.8 kWh/m^3 is achieved as permeate flux approaches zero, $\dot{V}_P / a \rightarrow 0$. On the other hand, operating at such low permeate flux requires oversizing the desalination plant, which is costly. There is a practical and economic requirement to maintain reasonably high flux in order for RO to be cost effective. Or in other words, lower specific energy associated with lower flux can only be justified if these energy cost savings are greater than the cost of building a larger plant. This illustrates that optimizing the specific energy of RO must be done while also respecting other performance targets and operating limits, including costs as well as the permeate quality and the membrane integrity, as explained next.

Figure 5.4 also shows the concentration of the permeate c_P that is produced from the RO desalination process. This permeate concentration is important because it is a measure of the quality of the water permeate. As shown, operating at low recovery ratios and with high permeate flux will tend to produce lower concentration water permeate.

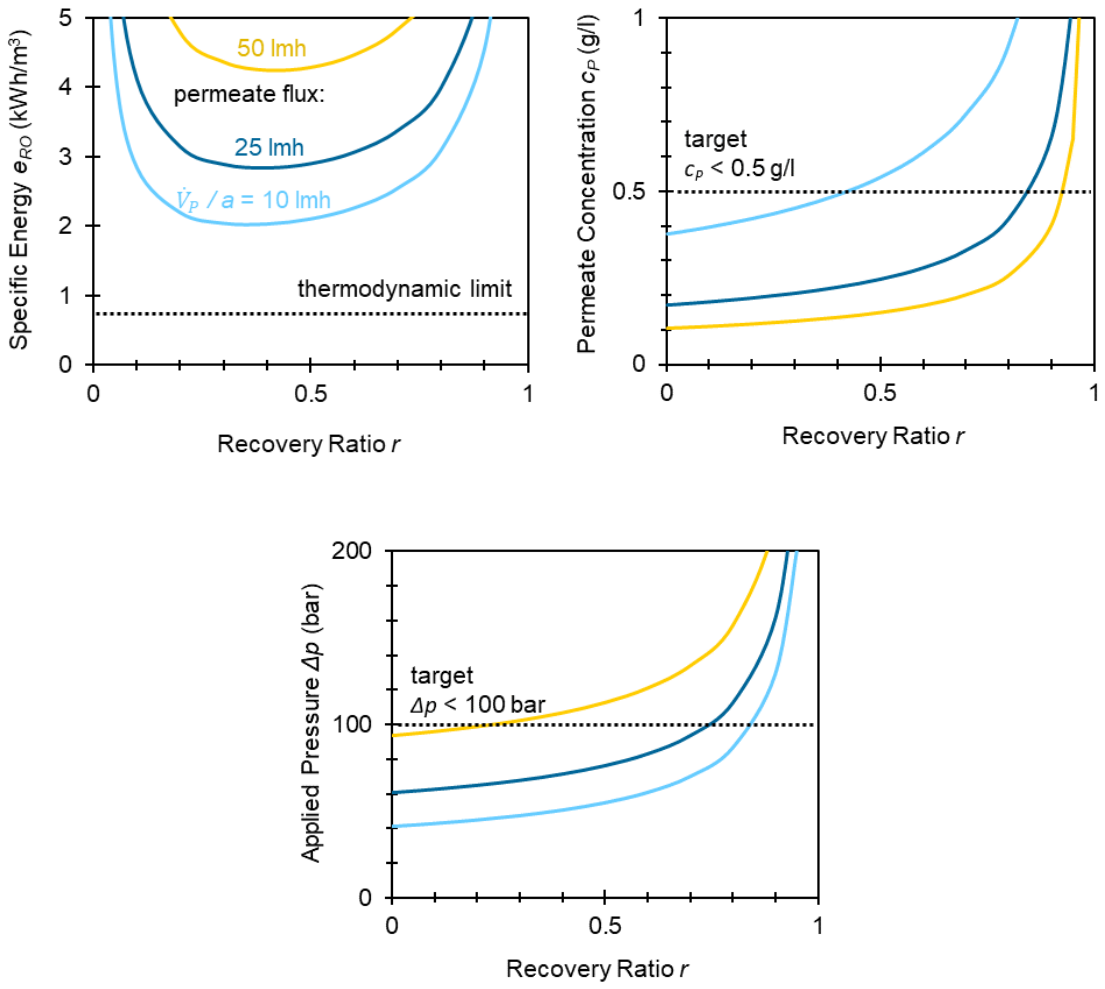

Figure 5.4 Specific energy use e_{RO}, concentration of permeate c_P, and applied pressure Δp for reverse osmosis desalination of seawater given a range of recovery ratios r and a range of normalized permeate rates $\dot{V}_P / a$. Default input parameters and assumptions are provided in Table 5.1.

This is because (i) low recovery ratios minimize the accumulation of salts in the feed, and hence lower the concentration driving force for salt diffusion, and (ii) higher permeate flux dilutes the permeating salts, lowering the permeate concentration. A water quality target of c_P < 0.5 g/l is provided for reference [241,242].

Figure 5.4 also shows the applied pressure Δp that drives RO and that is necessary to achieve the targets for recovery ratio and permeate flux. The applied pressure scales with both of these targets and may exceed the mechanical limits of the membrane unless care is taken to avoid such failure. For example, if high permeate flux $\dot{V}_P / a = 50$ lmh is desired, then recovery must be limited to $r < 0.25$ so as to avoid exceeding the membrane burst pressure. A RO membrane burst pressure of 100 bar is shown here for reference [12].

5.4.2 Advantages of Using Heat to Thermally-Enhance Reverse Osmosis

To illustrate the advantages of using heat to thermally enhance RO, consider again the application to seawater desalination. Figure 5.5 shows the specific energy of RO e_{RO} as feed temperature is increased above the ambient baseline of 20 °C (other input parameters and assumptions are provided in Table 5.1). As shown, specific energy reduces as feed is heated. The improvement is especially marked in cases where either high water permeate flux or a high recovery ratio is targeted, or both. For example, for the case where flux is maintained at $\dot{V}_P / a = 50$ lmh with a recovery ratio $r = 0.5$, specific energy is reduced by 24 % as feed is heated to $T = 50$ °C. Such improvements are consistent with what has been reported elsewhere in the literature [12,73,231,243]. On the other hand, an increase in permeate concentration is also observed. For the same example, the permeate concentration almost doubles from $c_P = 0.15$ to 0.28 g/l, although importantly it still remains below the water quality limit of 0.5 g/l.

These energy savings are the result of thermally-enhanced transport dynamics previously described in Section 5.1 (i.e. higher apparent membrane permeability and reduced polarization), which allow for target flux and recovery ratios to be achieved with

lower applied pressures. Operating at lower applied pressure not only reduces pump energy use, it also reduces the mechanical force applied to the membrane and thereby reduces the risks of membrane failure. For example, for the same case where flux is maintained at $\dot{V}_P / a$ = 50 lmh with recovery ratio r = 0.5, applied pressure at T = 20 °C initially exceeds the specified membrane burst pressure of 100 bar. But as feed is heated to T = 50 °C the applied pressure is reduced to a much lower and acceptable pressure of Δp = 86 bar. This suggests that thermally-enhanced RO can provide an energy efficient means of achieving high water permeate flux and high recovery ratios while mitigating the risks of membrane failure. Other advantages of operating at lower applied pressures have also been reported in the literature, including less fouling and crystallization at the membrane surface [180,244].

Analysis of the energy balance is incomplete however without consideration for the thermal energy input during thermally-enhanced RO. This depends largely on the efficiency of the thermal energy system, including the heat source's coefficient of performance and the heat recovery efficiency. Both of these variables are explored further in Section 5.2, but here the energy balance is shown assuming an ideal heat pump operating at its thermodynamic limit $cop = T / \Delta T$ and assuming heat exchanger efficiency of η_{Tex} = 0.9. As shown, the energy balance remains favorable even with consideration for the thermal energy input. Again, the most significant energy savings are observed when high flux and high recovery ratios are targeted. Referring to the same example as previously, where flux is maintained at $\dot{V}_P / a$ = 50 lmh and recovery ratio r = 0.5, the overall specific energy balance of thermally-enhanced RO is reduced from $e_{TE\text{-}RO}$

= 4.3 kWh/m^3 at ambient temperatures of T = 20 °C down to a minimum of $e_{TE\text{-}RO}$ = 3.8 kWh/m^3 at T = 41 °C , for a reduction of almost 12 %.

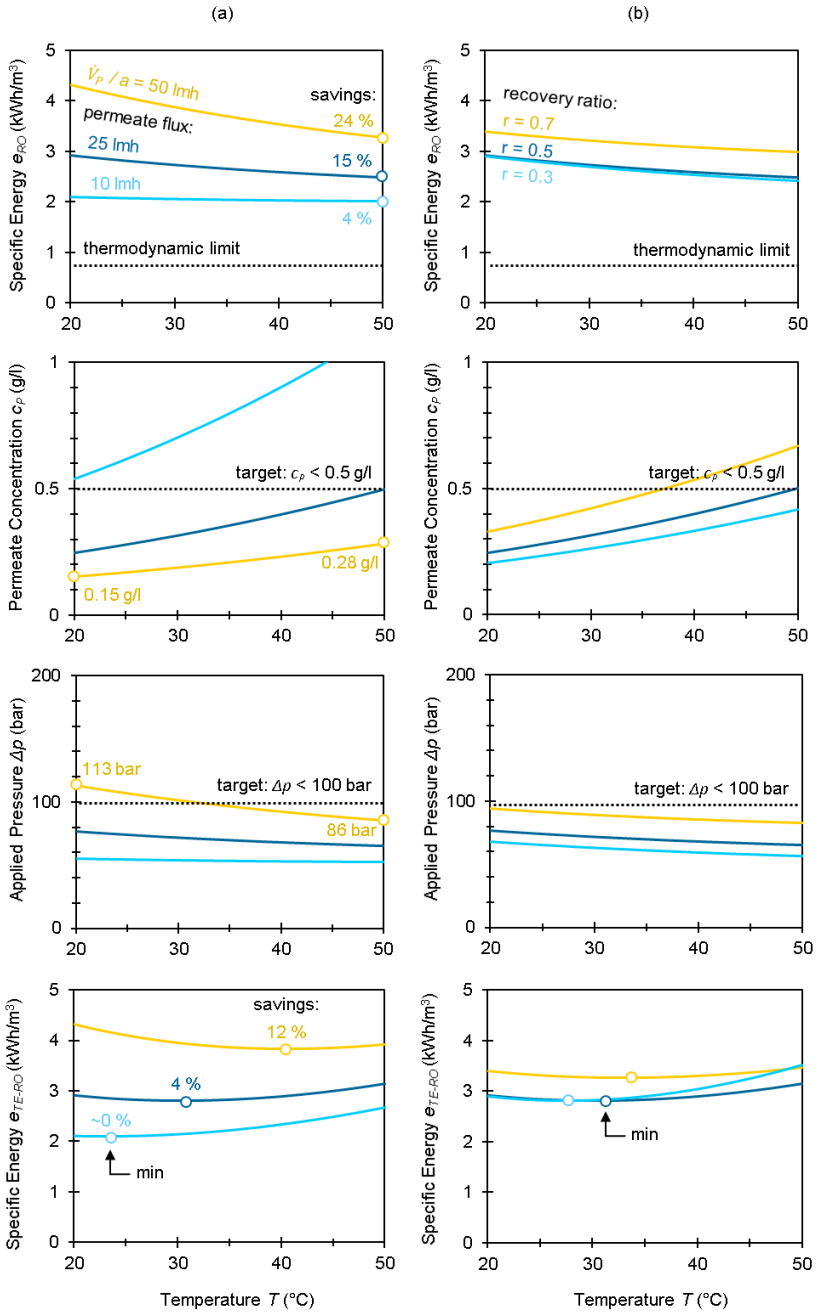

Figure 5.5 Specific energy of RO e_{RO}, concentration of permeate c_P, applied pressure Δp, and overall specific energy of thermally-enhanced RO $e_{TE\text{-}RO}$ for desalination of seawater at (a) several different rates of water permeate flux $\dot{V}_P / a$ and (b) several different recovery ratios r. Default input parameters and assumptions are provided in Table 5.1.

5.4.3 Importance of High Thermal Efficiency and of an Abundant Source of Heat

The overall energy balance of thermally-enhanced RO depends largely on the efficiency with which heat can be delivered to and recycled within the system. Figure 5.6 shows the specific energy of thermally-enhanced RO $e_{TE\text{-}RO}$ in response to a range of different heat source coefficients of performance *cop* and different heat exchanger efficiencies η_{Tex}. As shown, the overall energy balance can be favorable and produce savings if thermal efficiency is high. For example, with an ideal heat pump operating at its thermodynamic limit $cop = T / \Delta T$ and assuming heat exchanger efficiency of $\eta_{Tex} = 0.9$, the given scenario shows a minimum specific energy of $e_{TE\text{-}RO} = 2.8$ kWh/m^3 at $T = 31$ °C, equal to energy savings of 4 % relative to baseline temperature. On the other hand, when less optimistic thermal efficiencies are considered, the energy balance becomes unfavorable. For example, given $cop = 1$ or even 5, heating the feed actually increases the overall energy use. Similarly, a reduction in the heat exchanger efficiency also shows less favorable results. This suggests that for thermally-enhanced RO to yield energy savings, very efficient thermal energy systems are required. Note that a perfect heat exchanger essentially eliminates the need for thermal energy input as heat is recycled from the brine and permeate volumes and returned to the incoming feed.

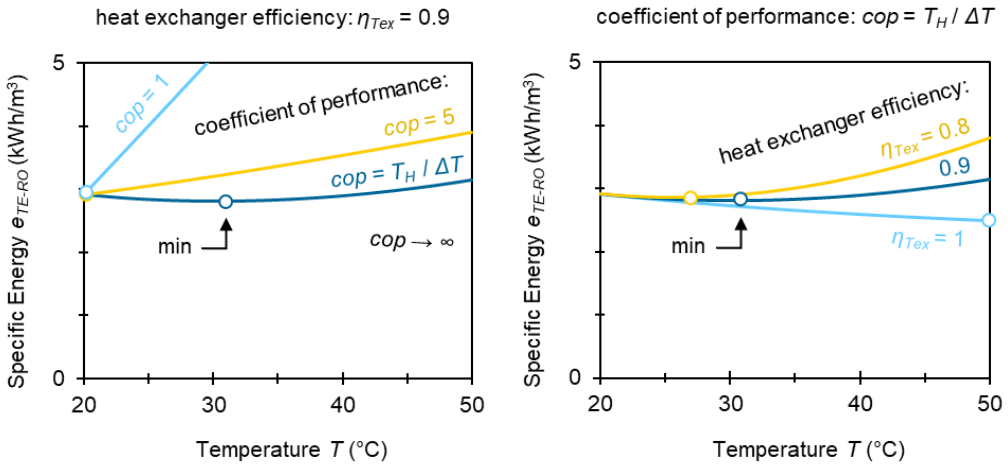

Figure 5.6 Specific energy of thermally-enhanced RO $e_{TE\text{-}RO}$ for desalination of seawater at a range of different feed temperatures T and for several different coefficients of performance cop and several different heat exchanger efficiencies η_{Tex}. Default input parameters and assumptions are provided in Table 5.1.

In analyzing the overall energy balance of thermally-enhanced RO, it is important to also consider that two different forms of energy are included: (i) mechanical work for pumping, and (ii) thermal energy for heating feed. The coefficient of performance previously introduced in equation (4.9) and analyzed above implies that mechanical work would be used to generate heat, but there are of course many alternatives such as solar thermal energy or waste heat from a power plant. In such cases, it is more appropriate to consider the energy balance of work and heat separately, as they each have their own distinct value [245]. Figure 5.7 shows the specific energy balance of work and heat for the default scenario from Table 5.1. As shown, the thermal energy input clearly exceeds the savings in mechanical pumping work (by a factor of between 11-16), and yet such a tradeoff may be acceptable in certain applications. For example, if waste heat is abundant and free, the investment of the necessary heat exchangers could be justified by the

electricity savings associated with less mechanical pumping work. Such a determination would require further techno-economic analysis in future work, but it does suggest another avenue forward for the proposed concept.

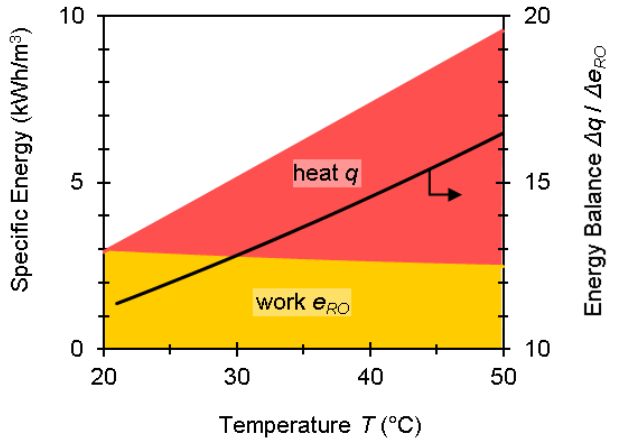

Figure 5.7 Energy balance of thermally-enhanced RO in terms of mechanical pumping work e_{RO} and thermal energy input q for desalination of seawater at a range of different feed temperatures T. The right-axis shows the ratio between thermal energy input and savings in mechanical work q / e_{RO} relative to baseline temperature. Default input parameters and assumptions are provided in Table 5.1.

5.4.4 Suitability of Thermally-Enhanced RO for a Variety of Feed Sources

Figure 5.8 shows the performance of thermally-enhanced RO when applied to different feed water sources. Several scenarios are considered including desalination of (i) seawater with concentration c_F = 35 g/l, (ii) brackish water with c_F = 10 g/l, and (iii) produced wastewater from oil and gas production with c_F = 70 g/l. In each case, the targets for water permeate flux and recovery ratio are adjusted so as to be consistent with conditions typical for treatment of these different sources. For (i) seawater, the water permeate flux and recovery ratio are set to the default targets, $\dot{V}_P$ / a = 25 lmh and r = 0.5.

For (ii) brackish water, the targets are set to $\dot{V}_P / a = 50$ lmh and $r = 0.75$. And for (iii) produced wastewater, the targets are set to $\dot{V}_P / a = 10$ lmh and $r = 0.25$.

As the results show, the advantages of thermally-enhanced RO are much more pronounced in applications with high water flux and recovery targets, which are typically associated with low concentration feed sources. For example, in the case of brackish water desalination, energy savings from reduced mechanical pumping reach up to 33 % when feed is heated to $T_F = 50$ °C. And even when thermal energy input is considered, the overall specific energy savings from thermally-enhanced RO reach up to 18 % when feed is heated from $T_F = 20$ to 46 °C. This is much more than the 4 % savings observed for the base case of seawater desalination. For produced water, the energy savings are negligible, mostly due to the fact that a low water permeate flux of only $\dot{V}_P / a = 10$ lmh is targeted, which tends to mitigate the benefits of heating feed. The low flux and recovery targets for produced wastewater are selected so as to moderate the very high applied pressures that are associated with RO of such a high concentration feed source. For this reason, several publications have suggested alternative RO cycles or membrane distillation for such feed [246,247].

Figure 5.8 also shows the significance of the ambient water temperature of the feed source. As shown, heating feed from a baseline temperature of either $T_o = 10$, 20, or 30 °C can be advantageous as it reduces energy use and applied pressure. Similar plots are shown for the specific work e_{RO}, permeate concentration c_P, and applied pressure Δp which confirms that transport dynamics are a function of feed temperature but not the baseline reference temperature. But the overall energy balance of the three cases does show some difference, because thermal efficiency of the theoretical heat pump is slightly higher if the

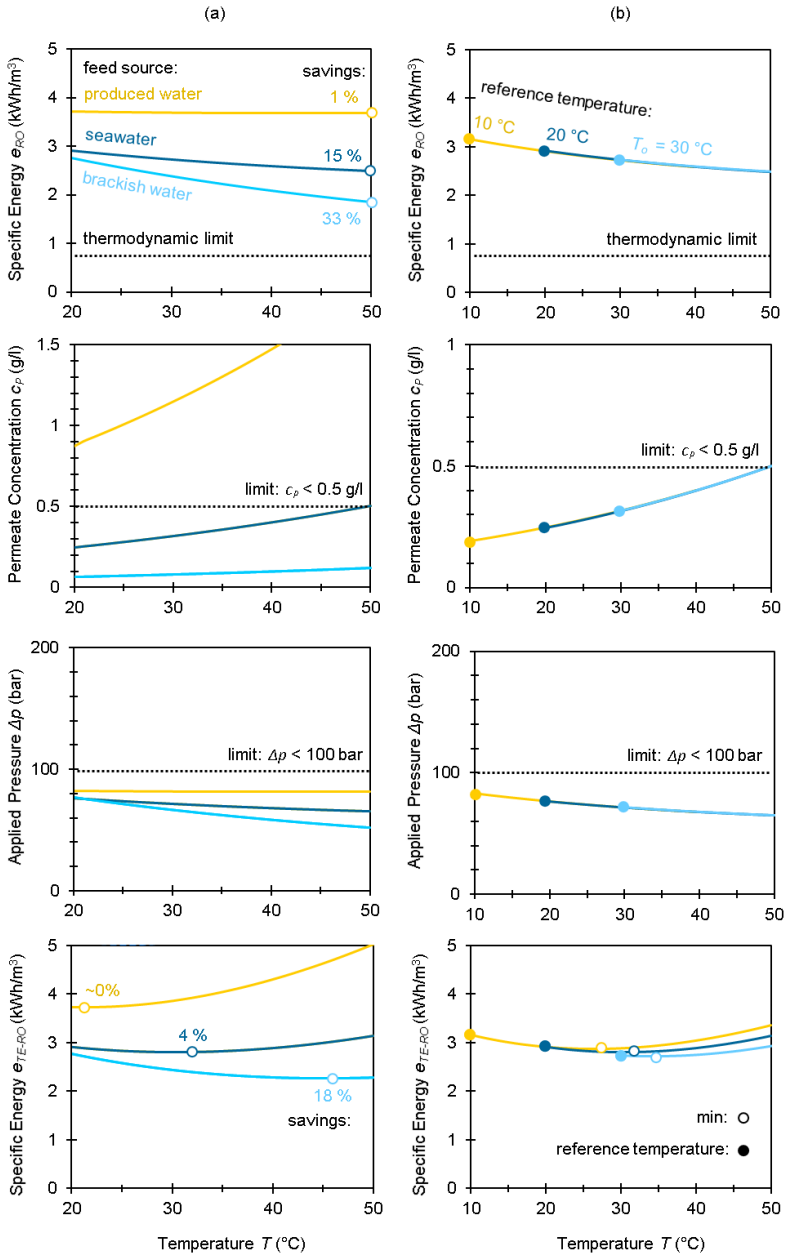

Figure 5.8 Specific energy of RO e_{RO}, concentration of permeate c_P, applied pressure Δp, and specific energy of thermally-enhanced RO $e_{TE\text{-}RO}$ for (a) desalination of several different feed sources, and for (b) desalination of seawater at a several different ambient temperatures T_o. Feed sources include seawater, brackish water, and produced wastewater with concentrations of c_F = 35, 10, and 70 g/l respectively, water flux targets of $\dot{V}_P$ / a = 25, 50, and 10 lmh, and water recovery targets of r = 0.5, 0.75, and 0.25, respectively. Other input parameters and assumptions are provided in Table 5.1.

reference temperature is lower. This confirms that higher thermal energy inputs can be justified when the feed has a cooler ambient reference temperature.

5.4.5 Suitability of Thermally-Enhanced RO to a Variety of Membranes

Figure 5.9 shows the significance of thermally-enhanced RO on the performance of different membranes with a variety of water and salt permeabilities A and B. Three membranes are defined to provide a sample of common membrane parameters across the permeability / selectivity limits established for RO membranes (similar to the Robeson limits for gas membranes) [248–250].The defined membranes include (i) a low permeability / high selectivity membrane with A = 0.5 lmh/bar and A/B = 20 / bar, (ii) a high permeability / low selectivity membrane with A = 2 lmh/bar and A/B = 5, and (iii) the default membrane with A = 1 lmh/bar and A/B = 10 / bar. While heat is beneficial in all three membranes, the energy savings $e_{TE\text{-}RO}$ and reductions in applied pressure Δp are most significant with the low permeability membrane. For example, in the defined low permeability membrane, overall specific energy savings of thermally-enhanced RO reach 9 % when feed is heated to 39 °C. This is to be expected since higher applied pressures are needed to achieve target flux with low permeability membranes, and hence additional energy savings can be obtained. This is also consistent with the previous observation that thermally-enhanced RO is most beneficial in high flux applications, since here a particular target flux would be relatively greater for a low permeability membrane. Interestingly, the drawback of higher permeate salt concentration c_P is also largely mitigated with the low permeability / high selectivity membrane. This suggests that thermally-enhanced RO may be particularly suited for systems involving low permeability / high selectivity membranes.

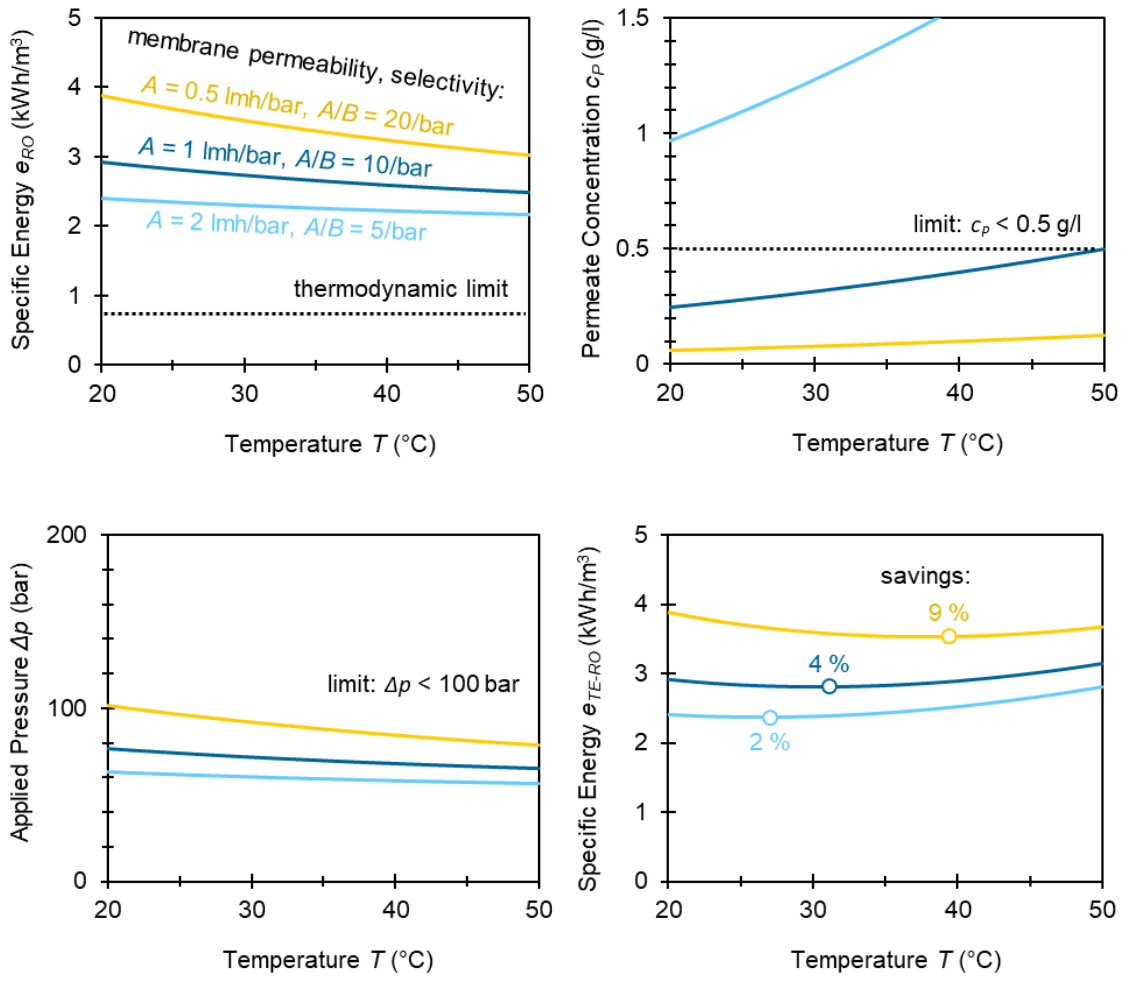

Figure 5.9 Specific energy of RO e_{RO}, concentration of permeate c_P, applied pressure Δp, and specific energy of thermally-enhanced RO $e_{TE\text{-}RO}$ for desalination of seawater with several different membranes, including different water permeabilities A and different water/salt selectivity A/B. Default input parameters and assumptions are provided in Table 5.1.

5.5 Conclusions

In In this study the potential for using low-grade heat to thermally-enhance RO desalination was evaluated using a theoretical thermodynamic analysis. In general, adding thermal energy to increase the temperature of RO feed was shown to significantly improve water permeate flux leading to important savings in mechanical work.

Reductions in specific energy of up to 24 % were observed for high flux seawater desalination and up to 33 % for brackish water, when feed temperature was increased from 20 to 50 °C. Such improvements are consistent with what has been reported elsewhere in the literature [12,73,231,251], however until now the thermal energy input required to heat feed has been mostly unaccounted for.

For the first time, an overall energy balance of thermally-enhanced RO was considered to evaluate the tradeoff between savings in mechanical pump work and input of thermal energy. Results suggest that this tradeoff can be favorable under the right conditions. In particular, there is a need for high thermal efficiencies including both a very high heat pump coefficient of performance (if work is used to supply heat), and very high heat exchanger efficiency for recycling thermal energy within the system. Under these conditions, overall energy savings of up to 12 % were observed for seawater desalination when feed temperature was increased from 20 to 41 °C, and up to 18 % for brackish water desalination with feed heated to 46 °C.

Other key variables were also identified. The energy balance was found to be particularly favorable in applications where high water flux is desired, such as in desalination of brackish water, and in applications where membrane water permeability is low and represents a limiting factor. Thermally-enhanced RO is also recommended for applications where high feed concentrations typically require elevated applied pressures. In such cases, thermally-enhanced RO can provide a means of reducing the mechanical force applied to the membrane and thereby reduce the risks of membrane failure. On the other hand, additional consideration should be given to the thermal stability of membranes when exposed to high temperatures for sustained periods of time.

Encouragingly, recent publications suggest that advanced membranes show stable operation at elevated temperatures [232].

Other important drawbacks should also be considered in future work. A significant increase in salt leakage was observed throughout the analysis, resulting in increased permeate concentrations. For example, for the case of seawater desalination where 12 % overall energy savings were reported, permeate concentration increased from 0.15 to 0.23 g/l when feed temperature was increased from 20 to 41 °C. Similar increases were observed across the various scenarios considered. Although this particular case remained below our target of 0.5 g/l, other scenarios may be more significant and for certain applications tolerances may be lesser, possibly necessitating an additional RO pass of the permeate. For example, of particular concern is leakage of boron, for which permeate concentrations of less than 0.5 mg/l are often targeted [252]. Boron leakage is likely to be exacerbated at high temperatures, although recent studies have managed to achieve promising boron selectivity even at high temperatures [232]. Also, of concern is the precipitation of calcium nitrate and other scaling agents that are typically exacerbated at high temperatures [253]. Chemical and mechanical cleaning can mitigate such scaling, but at a cost.

To further clarify the potential of thermally-enhanced RO we suggest that future work consider the techno-economic balance between the cost savings of reduced mechanical pumping work and the cost of adding thermal energy, including additional operating and capital costs. In such an analysis, the levelized cost of water can be optimized based on the cost of electricity and the cost of thermal energy. There are several abundant sources of low-grade heat such as solar radiation and power plant waste heat that can be

considered, thereby avoiding the need for using electricity or fuel to generate heat, but even in such cases the capital cost of the heat recovery systems would need to be justified. Therefore, while this study suggests that the concept of thermally-enhanced RO has thermodynamic merit, with a favorable energy balance under the right conditions, it remains to be seen whether an economic and practical case can be made for the concept. If future work confirms this, then thermally-enhanced RO may represent a means of improving the sustainability of water infrastructure and increasing global access to freshwater.

5.6 Nomenclature

A	membrane water permeability (m^3 s^{-1} Pa^{-1} m^{-2})
a	area (m^2)
B	membrane salt permeability (m^3 s^{-1} m^{-2})
c	concentration (mol m^{-3})
c_p	specific heat capacity (J kg^{-1} K^{-1})
cop	coefficient of performance
D	diffusivity (m^2 s^{-1})
d	hydraulic diameter (m)
E	energy (W)
e	specific energy (J m^{-3})
i	number of ions
k	mass transfer coefficient (m s^{-1})
p	pressure (Pa)
$\dot{Q}$	heat transfer rate (W)
q	specific heat (J m^{-3})
R	gas constant (J mol^{-1} K^{-1})
Re	Reynolds number

r	recovery ratio
Sc	Schmidt number
Sh	Sherwood number
T	temperature (K)
V	Volume (m^3)
$\dot{V}$	volume rate ($m^3\ s^{-1}$)

Greek Symbols:

π	osmotic pressure (Pa)
ρ	density ($kg\ m^{-3}$)
η	efficiency
μ	absolute viscosity (Pa s)

Subscripts:

B	brine
F	feed
hex	heat exchanger
loss	loss
P	permeate
pex	pressure exchanger
pump	pump
RO	reverse osmosis
TE-RO	thermally enhanced reverse osmosis

5.7 Supplementary Notes

5.7.1 Supplementary Note 5.1: RO Energy Use by Pumps

The energy consumption of RO is related to the pumping power that is required to pressurize feed solution above its osmotic pressure potential. As described in equation (5.1), the pumping load can be distributed between two pumps, with one to handle a portion of the feed equal to the permeate volume, and another to handle a portion equal to

the brine volume. This configuration facilitates integration of a pressure exchanger capable of recovering mechanical energy from the pressurized brine solution and recycling it back to the incoming feed. A simple derivation of the energy requirements of both of these pumps is provided below.

$$e_{RO} = \frac{E_{RO}}{V_P} = e_P + e_B \tag{5.1}$$

The energy use of the first pump E_P is simply the product of the applied pressure Δp, the volume through it (which is equal to the permeate volume V_P), and the inverse of the pump efficiency η_{pump}. When normalized per unit volume of permeate, it can be expressed as the specific energy e_P.

$$E_P = \frac{1}{\eta_{pump}} V_P \, \Delta p \tag{S5.2a}$$

$$e_P = \frac{E_P}{V_P} = \frac{1}{\eta_{pump}} \Delta p \tag{5.2}$$

The energy use of the second pump E_B is the product of the brine volume (which is equal to the brine volume V_B), the pressure that is needed to make up for losses in the pressure exchanger, and the inverse of the pump efficiency. Note that in an ideal system, with a perfect pressure exchanger $\eta_{pex} \rightarrow 1$, the load on this brine pump would be reduced to zero $E_B \rightarrow 0$. When normalized per unit volume of permeate, it can be expressed as the specific energy e_B.

$$E_B = \frac{1}{\eta_{pump}} V_B \, \Delta p \left(1 - \eta_{p\,ex}\right) \tag{S5.3a}$$

$$E_B = \frac{1}{\eta_{pump}} V_P \left(\frac{1}{r} - 1\right) \Delta p \left(1 - \eta_{p\,ex}\right) \quad \text{(S5.3b)}$$

$$e_B = \frac{E_B}{V_P} = \frac{1}{\eta_{pump}} \left(\frac{1}{r} - 1\right) \Delta p \left(1 - \eta_{p\,ex}\right) \quad \text{(5.3)}$$

Where *r* is the recovery ratio. Pressure losses due to friction in the system are neglected.

5.7.2 Supplementary Note 5.2: Applied Pressure

Applied pressure is an operating parameter that can be controlled to achieve target rates of water permeate recovery. The relationship between applied pressure Δp and water permeate rate $\dot{V}_P$ is described by the solution-diffusion model [254–256].

$$\dot{V}_P = a\,A\,(\Delta p - \Delta\pi) \quad \text{(S5.4a)}$$

$$\Delta p = \frac{\dot{V}_P}{a} A^{-1} + \Delta\pi \quad \text{(5.4)}$$

Where *a* is the membrane surface area, *A* is the membrane water permeability, and $\Delta\pi$ is the osmotic pressure difference across the membrane.

5.7.3 Supplementary Note 5.3: Permeate and Brine Concentrations

Concentration will vary along the length of the membrane as water permeate is recovered from the feed and as salt leaks through the imperfect membrane. To account for this variation and its important effect on osmotic pressure, the concentration difference is defined in equation (5.6) as a function of the logarithmic mean between the inlet c_F and the outlet c_B. Alternatively, the feed side concentration could be simplified with just the arithmetic mean as in equation (S5.6a).

$$\Delta c = \exp\left(\frac{\dot{V}_P}{a} k^{-1}\right)\left(\frac{c_B - c_F}{\ln c_B - \ln c_F}\right) - c_P \tag{5.6}$$

$$\Delta c = \exp\left(\frac{\dot{V}_P}{a} k^{-1}\right)\left(\frac{c_B + c_F}{2}\right) - c_P \tag{S5.6a}$$

The concentration of the brine c_B can be defined by taking a simple mass flow balance of the salt that is present in the feed, permeate, and brine, respectively $\dot{m}_F$, $\dot{m}_P$,and $\dot{m}_B$. This is shown in equation (5.7). Note that for low recovery ratios $r \rightarrow 0$, the concentration of the outlet brine approaches that of the inlet feed, $c_B \rightarrow c_F$.

$$\dot{m}_F = \dot{m}_P + \dot{m}_B \tag{S5.7a}$$

$$\dot{V}_F\, c_F = \dot{V}_P\, c_P + \dot{V}_B\, c_B \tag{S5.7b}$$

$$c_F = \frac{\dot{V}_p}{\dot{V}_F} c_P + \frac{\dot{V}_B}{\dot{V}_F} c_B \tag{S5.7c}$$

$$c_F = r\, c_P + (1 - r)\, c_B \tag{S5.7d}$$

$$c_B = \frac{c_F - r\, c_P}{1 - r} \tag{5.7}$$

The concentration of the permeate c_P, can be defined by considering the mechanism by which salt is transported across the membrane. Equation (S5.8a) defines the mass permeate rate of salt $\dot{m}_P$ as a function of diffusion driven by the concentration difference across the membrane Δc, where B is the membrane's salt permeability. This can be reorganized to obtain an expression for permeate concentration c_P as provided in equation

(5.8). Note that for an ideal membrane that is impermeable to salt $B \rightarrow 0$, the concentration of the permeate is negligible $c_P \rightarrow 0$.

$$\dot{m}_P = a\ B\ \Delta c \tag{S5.8a}$$

$$\dot{V}_P\ c_P = a\ B\ \Delta c \tag{S5.8b}$$

$$c_P = \frac{a}{\dot{V}_P}\ B\ \Delta c \tag{5.8}$$

Together, equations (S5.6)-(S5.8) describe the salt mass balance between feed, brine, and permeate. To solve for the resulting concentration difference Δc, the system of equations presented here requires a numerical approach to solve, such as an iterative guess and check method. Alternatively, it may be of interest in certain cases to approximate the feed concentration with a simple arithmetic mean, as shown previously in equation (S5.6a). This makes it possible to obtain an analytical solution for Δc, as shown below, but it also introduces additional error to the analaysis, which is why it is not employed here.

$$\Delta c = \exp\left(\frac{\dot{V}_P}{a} k^{-1}\right)\left(\frac{c_F + c_B}{2}\right) - c_P \tag{S5.6a}$$

$$\Delta c = \exp\left(\frac{\dot{V}_P}{a} k^{-1}\right)\left(\frac{c_F + \left(\frac{c_F - r\ c_P}{1 - r}\right)}{2}\right) - \frac{a}{\dot{V}_P}\ B\ \Delta c \tag{S5.6b}$$

$$\Delta c = \exp\left(\frac{\dot{V}_P}{a} k^{-1}\right)\left(\frac{c_F + \left(\frac{c_F - r\,\frac{a}{\dot{V}_P}\,B\,\Delta c}{1-r}\right)}{2}\right) - \frac{a}{\dot{V}_P}\,B\,\Delta c \qquad \text{(S5.6c)}$$

$$\Delta c = c_F \frac{\left(1 + \frac{1}{1-r}\right)}{\left(2\frac{1 + \frac{a}{\dot{V}_P}\,B}{\exp\left(\frac{\dot{V}_P}{a}\,k^{-1}\right)} + \left(\frac{r}{1-r}\right)\frac{a}{\dot{V}_P}\,B\right)} \qquad \text{(S5.6d)}$$

5.7.4 Supplementary Note 5.4: Thermal Energy Use

Thermal specific energy consumption is a measure of the thermal energy required to raise the feed temperature, considering the recovered heat by heat exchangers from the brine and permeate flows. We also have considered the efficiency of heater which shows the performance of heater in converting the electrical power to thermal energy. The following lines provide a detailed derivation of thermal specific consumption equations.

Rate of heat transfer to the system $\dot{Q}$ is the balance between rate at which heat is supplied to the feed $\dot{Q}_F$ and rate of heat recovery from the brine $\dot{Q}_B$ and from the permeate $\dot{Q}_P$.

$$\dot{Q} = \dot{Q}_F - \dot{Q}_B - \dot{Q}_P \qquad \text{(S5.10a)}$$

Rate of heat transfer is defined here as the product of rate of volume $\dot{V}$, density ρ, specific heat c_p, and temperature T (since neglecting any changes to pressure and volume reduces enthalpy to only internal energy).

$$\dot{Q}_F = \rho\, c_p\, \dot{V}_F\, \Delta T \qquad \text{(S5.10b)}$$

$$\dot{Q}_B = \rho\, c_p\, \dot{V}_B\, \Delta T_B \tag{S5.10c}$$

$$\dot{Q}_P = \rho\, c_p\, \dot{V}_P\, \Delta T_P \tag{S5.10d}$$

The change in temperature across either the brine or permeate heat exchangers ΔT_B and ΔT_P can be written as a fraction of the change in feed temperature ΔT and as a function of heat exchanger efficiency η_{hex}. Figure S5.1 shows the boundary conditions of heat exchangers used at the brine and permeate to recover heat and recycle to feed inlet. Additional heat required to heat the feed to desired temperature after recovering heat from brine and permeate is supplied using a heat pump.

$$\dot{Q}_B = \rho\, c_p\, \dot{V}_B\, \eta_{hex}\, \Delta T \tag{S5.10e}$$

$$\dot{Q}_P = \rho\, c_p\, \dot{V}_P\, \eta_{hex}\, \Delta T \tag{S5.10f}$$

Then substituting into equation (5.10) and treating density and specific heat as constant across all three terms, we can rearrange to obtain an expression for the specific thermal energy input q.

$$\dot{Q} = \rho\, c_p \Delta T \left(\dot{V}_F - \dot{V}_B\, \eta_{hex} - \dot{V}_P\, \eta_{hex}\right) \tag{S5.10g}$$

$$\dot{Q} = \rho\, c_p\, \dot{V}_F\, \Delta T(1 - \eta_{hex}) \tag{S5.10h}$$

$$\dot{Q} = \rho\, c_p\, \frac{\dot{V}_P}{r}\, \Delta T(1 - \eta_{hex}) \tag{S5.10i}$$

$$q = \frac{\dot{Q}}{\dot{V}_P} = \frac{1}{r}\, \rho\, c_p \Delta T\, (1 - \eta_{hex}) \tag{5.10}$$

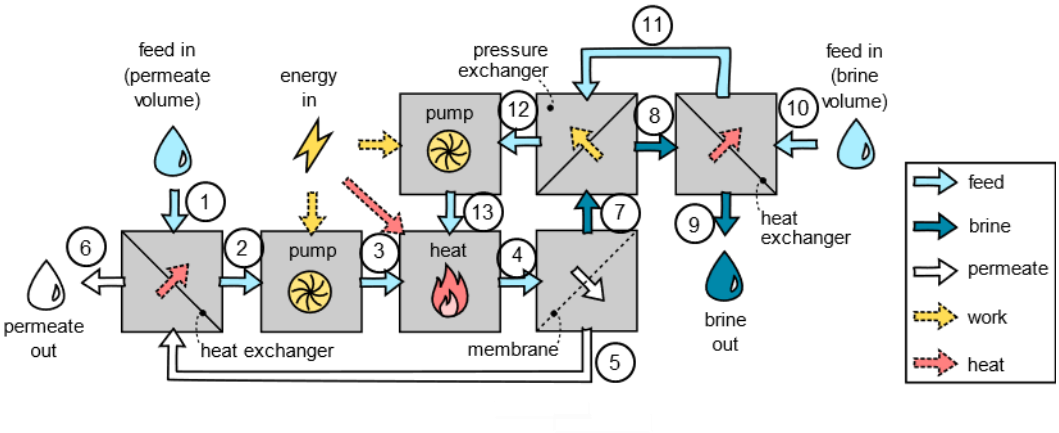

Position	Flow Rate	Pressure	Temperature
1	$\dot{V}_P$	0	T_F
2	$\dot{V}_P$	0	$T_F + \Delta T\ \eta_{hex}$
3	$\dot{V}_P$	Δp	$T_F + \Delta T\ \eta_{hex}$
4	$\dot{V}_F$	Δp	$T_F + \Delta T$
5	$\dot{V}_P$	0	$T_F + \Delta T$
6	$\dot{V}_p$	0	$T_F + \Delta T\ (1- \eta_{hex})$
7	$\dot{V}_B$	Δp	$T_F + \Delta T$
8	$\dot{V}_B$	$\Delta p\ (1- \eta_{pex})$	$T_F + \Delta T$
9	$\dot{V}_B$	$\Delta p\ (1- \eta_{pex})$	$T_F + \Delta T\ (1- \eta_{hex})$
10	$\dot{V}_B$	0	T_F
11	$\dot{V}_B$	0	$T_F + \Delta T\ \eta_{hex}$
12	$\dot{V}_B$	$\Delta p\ \eta_{pex}$	$T_F + \Delta T\ \eta_{hex}$
13	$\dot{V}_B$	Δp	$T_F + \Delta T\ \eta_{hex}$

Figure S5.1 Flowrate, pressure and temperature at different points of the thermally enhanced RO system.

5.7.5 Supplementary Note 5.5: Membrane Permeability as a Function of Temperature

Adding heat to the RO process will increase the membrane's apparent permeability to salt [71,144,151,154,155,157,169,171,172,174,175,181]. Importantly, most of the observed increase in salt permeability will be due to changes in the fluid properties,

rather than any thermally induced changes in the membrane structure itself [172,175]. It has previously been suggested that salt permeability B is directly proportional to temperature T and inversely proportional to viscosity μ, as described in equation (S4.16a) [152]. Since salt diffusivity D is proportional to T / μ [154,178,225], the membrane salt permeability can also be described as a function of salt diffusivity D, as described in equation (5.16).

$$B = B_o \frac{T}{T_o} \frac{\mu_o}{\mu} \tag{S5.16a}$$

$$D \propto \frac{T}{\mu} \tag{S5.16b}$$

$$B = B_o \frac{D}{D_o} \tag{5.16}$$

Figure S5.1 shows a collection of salt permeability results at a range of temperatures, as collected from the literature. Equation (5.16) is also plotted and shows agreement with experimental data.

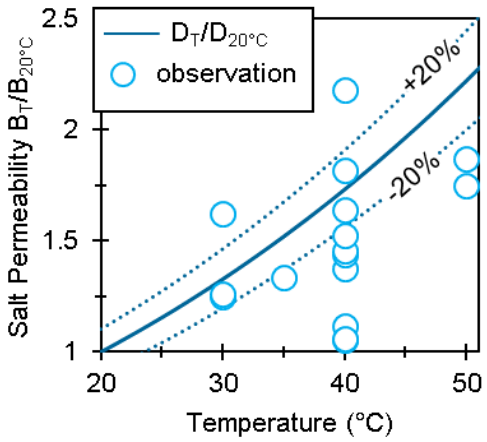

Figure S5.2 Membrane salt permeability as a function of temperature can be predicted from the proportional change in salt diffusivity as described in equation (5.16). This simple model for membrane salt permeability is compared against experimental data from the literature [71,144,154,171,172,174,175,181].

CHAPTER SIX
CONCLUSIONS

6.1 Contributions

This dissertation proposes two potential approaches for reducing the energy consumption of the desalination process. Moving towards a fully renewable powered desalination process could take time owing to the ease of implementing the current established conventional process and the added capital costs to employ renewable energy systems in a desalination plant. This suggests that improving the energy efficiency of the desalination process itself and optimizing and process improvement of the existing energy recovery processes to reduce the costs associated with their commercialization should be given importance. This will help reduce the environmental impact associated with the high-energy demands of the desalination process. This would also promote the sustainability of processes while preparing the water purification industry for increasing water demands.

6.1.1 Improving Energy Efficiency of Pressure Retarded Osmosis for Energy Recovery from RO Brine Using Maximum Power Point Tracking Control Strategy

Chapter Two addresses the influence that operating conditions have on net power of a PRO system and how a particular set of operating conditions can help balance non-ideal factors and improve PRO performance. A feedback controller is introduced for the coordinated control of supply flowrates, and applied pressure loading. A simple perturb and observe (P&O) algorithm is developed and used for both maximum power point tracking (MPPT) and maximum specific energy tracking. A mathematical model was

described and used to simulate the performance of the controller for different changes in the operating conditions considered. This is the first system that has been developed for real-time control of not only applied pressure but also supply flow rates. In the case of stand-alone PRO with river water and seawater, the best inlet velocities ranged from 4 to 15 cm/s depending on membrane properties. For combined RO-PRO systems that use RO brine and brackish water, the best inlet velocities ranged from 6 to 20 cm/s. In all cases, the applied pressure was less than half the osmotic pressure difference, which is the theoretical maximum power point. The results are case-specific and change with membrane properties, module geometry, source chemistry, equipment efficiencies, pre-treatment systems, and many other factors.

The tradeoff between high power production and energy production was clearly demonstrated. When MPPT was employed under RO-PRO conditions, a maximum power of 12.9 W/m^2 was achieved, whereas the specific energy was only 0.07 kWh/m^3. Whereas, implementing maximum specific energy tracking strategy led to maximum specific energy of 0.30 kWh/m^3 and only 3.5 W/m^2 net power density. This tradeoff suggests that while high power densities (i.e. $\dot{W} > 5$ W/m^2) can be successfully obtained by application of the proper operating conditions, osmotic power systems still must overcome the hurdle of low specific energy densities in order to be a viable technology.

Chapter Three introduces a laboratory-scale PRO test bench designed to demonstrate the effectiveness of the proposed MPPT control strategy. To date, no experimental demonstration has been conducted to identify the maximum power point of PRO systems. Through extensive testing, the performance of the MPPT system for PRO applications in both energy recovery from RO brine and stand-alone power generation was evaluated.

Implementation of the MPPT control strategy on the RO-PRO case increases power density by over threefold, from 0.6 W/ m^2 to 2 W/ m^2. In the standalone PRO case, the system achieves close to the maximum net power output of 0.19 W/ m^2, a significant improvement from its initial negative value of -0.36 W/ m^2. This chapter also highlights methods to optimize the MPPT algorithm to further enhance performance by reducing the interval between steps and reducing the perturbation signal size.

6.1.2 Improving Energy Savings of RO Desalination Using Low Grade Heat

In Chapter Four, the concept of using heat to thermally-enhance osmotic power from pressure retarded osmosis process was demonstrated. A finite-element transport model was developed to understand the theoretical transport dynamics behind the improved performance at elevated temperatures. Results show that heating feed solution improves performance much more than heating draw. Based on the experimental and analytical investigation, the reason for the improved performance at elevated temperatures is concluded to be a warmer membrane active layer, which is hotter when the feed is heated compared to when draw is heated because the feed side boundary layer offers relatively little thermal resistance. A new metric called effectiveness was introduced, which normalizes the change in power density over the change in the feed and draw solution temperatures. A maximum effectiveness of 5.8 % W/m^2 / °C was achieved at low feed solution temperatures of 30 °C. This analysis suggests that lower temperatures can potentially lead to more effective use of heat.

In Chapter Five, the potential of using low-grade heat to thermally enhance RO desalination is evaluated. Reductions in the specific energy of up to 24 % were observed for seawater desalination and up to 33 % for brackish water when the feed temperature

was increased from 20 to 50 °C. For the first time, the overall energy balance of thermally enhanced RO was considered to evaluate the tradeoff between savings in electric energy consumption and heat energy input. Results suggest that for this trade off to become favorable, there is a need for high thermal efficiencies including both a very high heat pump coefficient of performance and very high heat exchanger efficiency for recycling thermal energy within the system. Under these optimal conditions, overall energy savings of up to 12 % were observed for seawater desalination when the feed temperature was increased from 20 to 41 °C, and up to 18 % for brackish water desalination when the feed was heated to 46 °C.

6.2 Future Work

6.2.1 Experimental Implementation of P&O Algorithm to Find Minimum Specific Energy Point for Reverse Osmosis

The tradeoff between the savings in mechanical pump work and the input of thermal energy introduced in Chapter Five suggests that adding heat is beneficial only under certain conditions, such as when operating with high thermal efficiencies. In addition, the results suggest that the benefits do not necessarily increase with more heat, since the highest energy savings for the seawater case were achieved at 40 ℃. This suggests that the operating temperature must be optimized. The P&O algorithm introduced in Chapter Two can be used to develop a strategy to determine the operating temperature that leads to the minimum specific energy consumption of a thermally enhanced RO system, accounting for the tradeoff between electric energy savings and thermal energy input. This strategy can be implemented experimentally using the setup shown in Figure 3.6.

This work will be done in collaboration with other graduate students in our research group.

6.2.2 Economic Analysis of Thermally Enhanced Reverse Osmosis

The analytical model introduced in Chapter Four can be further developed to include economic analysis to find the levelized cost of water (LCOW) produced when thermal energy is added to an RO system. The LCOW is a measure of the cost per unit of water permeate produced by the system [257–259]. While specific energy is one of the critical variables in the feasibility of RO, other variables also affect the overall cost and financial viability of a project, and in many cases, cost-effective operation does not always align exactly with the minimum specific energy operating point of the system. Hence, this economic analysis would help to understand whether the reduced electric energy consumption due to the addition of heat to a desalination process is economically justifiable.

REFERENCES

[1] F. Harvey, F.H.E. editor, Global fresh water demand will outstrip supply by 40% by 2030, say experts, The Guardian (2023). https://www.theguardian.com/environment/2023/mar/17/global-fresh-water-demand-outstrip-supply-by-2030 (accessed August 24, 2023).

[2] Z. Khan, I. Thompson, C.R. Vernon, N.T. Graham, T.B. Wild, M. Chen, Global monthly sectoral water use for 2010–2100 at 0.5° resolution across alternative futures, Sci Data 10 (2023) 201. https://doi.org/10.1038/s41597-023-02086-2.

[3] A. Boretti, L. Rosa, Reassessing the projections of the World Water Development Report, Npj Clean Water 2 (2019) 1–6. https://doi.org/10.1038/s41545-019-0039-9.

[4] N. Dhakal, S.G. Salinas-Rodriguez, J. Hamdani, A. Abushaban, H. Sawalha, J.C. Schippers, M.D. Kennedy, Is Desalination a Solution to Freshwater Scarcity in Developing Countries?, Membranes (Basel) 12 (2022) 381. https://doi.org/10.3390/membranes12040381.

[5] E. Jones, M. Qadir, M.T.H. van Vliet, V. Smakhtin, S. Kang, The state of desalination and brine production: A global outlook, Science of The Total Environment 657 (2019) 1343–1356. https://doi.org/10.1016/j.scitotenv.2018.12.076.

[6] B.J. Feinberg, G.Z. Ramon, E.M.V. Hoek, Thermodynamic Analysis of Osmotic Energy Recovery at a Reverse Osmosis Desalination Plant, Environ. Sci. Technol. 47 (2013) 2982–2989. https://doi.org/10.1021/es304224b.

[7] F. Leon, A. Ramos-Martin, S.O. Perez-Baez, Study of the Ecological Footprint and Carbon Footprint in a Reverse Osmosis Sea Water Desalination Plant, Membranes 11 (2021) 377. https://doi.org/10.3390/membranes11060377.

[8] A. Tal, Addressing Desalination's Carbon Footprint: The Israeli Experience, Water 10 (2018) 197. https://doi.org/10.3390/w10020197.

[9] A.S. Stillwell, M.E. Webber, Predicting the Specific Energy Consumption of Reverse Osmosis Desalination, Water 8 (2016) 601. https://doi.org/10.3390/w8120601.

[10] M. Khayet, E. Aytaç, T. Matsuura, Bibliometric and sentiment analysis with machine learning on the scientific contribution of Professor Srinivasa Sourirajan, Desalination 543 (2022) 116095. https://doi.org/10.1016/j.desal.2022.116095.

[11] S. Loeb, Circumstances leading to the first municipal reverse osmosis desalination plant, Desalination 50 (1984) 53–58. https://doi.org/10.1016/0011-9164(84)85015-8.

[12] S.H. Aladwani, M.A. Al-Obaidi, I.M. Mujtaba, Performance of reverse osmosis based desalination process using spiral wound membrane: Sensitivity study of operating parameters under variable seawater conditions, Cleaner Engineering and Technology 5 (2021) 100284. https://doi.org/10.1016/j.clet.2021.100284.

[13] C.Z. Liang, M. Askari, L.T. (Simon) Choong, T.-S. Chung, Ultra-strong polymeric hollow fiber membranes for saline dewatering and desalination, Nat Commun 12 (2021) 2338. https://doi.org/10.1038/s41467-021-22684-1.

[14] Y.J. Lim, Y. Ma, J.W. Chew, R. Wang, Assessing the potential of highly permeable reverse osmosis membranes for desalination: Specific energy and footprint analysis, Desalination 533 (2022) 115771. https://doi.org/10.1016/j.desal.2022.115771.

[15] The Critical Need for Increased Selectivity, Not Increased Water Permeability, for Desalination Membranes | Environmental Science & Technology Letters, (n.d.). https://pubs.acs.org/doi/10.1021/acs.estlett.6b00050 (accessed December 11, 2022).

[16] A. Matin, T. Laoui, W. Falath, M. Farooque, Fouling control in reverse osmosis for water desalination & reuse: Current practices & emerging environment-friendly technologies, Science of The Total Environment 765 (2021) 142721. https://doi.org/10.1016/j.scitotenv.2020.142721.

[17] M.A. Ahmed, S. Amin, A.A. Mohamed, Fouling in reverse osmosis membranes: monitoring, characterization, mitigation strategies and future directions, Heliyon 9 (2023) e14908. https://doi.org/10.1016/j.heliyon.2023.e14908.

[18] E.M.V. Hoek, T.M. Weigand, A. Edalat, Reverse osmosis membrane biofouling: causes, consequences and countermeasures, Npj Clean Water 5 (2022) 1–16. https://doi.org/10.1038/s41545-022-00183-0.

[19] I. Levitsky, D. Tavor, V. Gitis, Microbubbles and organic fouling in flat sheet ultrafiltration membranes, Separation and Purification Technology 268 (2021) 118710. https://doi.org/10.1016/j.seppur.2021.118710.

[20] S. Jiang, Y. Li, B.P. Ladewig, A review of reverse osmosis membrane fouling and control strategies, Science of The Total Environment 595 (2017) 567–583. https://doi.org/10.1016/j.scitotenv.2017.03.235.

[21] P.K. Cornejo, M.V.E. Santana, D.R. Hokanson, J.R. Mihelcic, Q. Zhang, Carbon footprint of water reuse and desalination: a review of greenhouse gas emissions and estimation tools, Journal of Water Reuse and Desalination 4 (2014) 238–252. https://doi.org/10.2166/wrd.2014.058.

[22] H. Nassrullah, S.F. Anis, R. Hashaikeh, N. Hilal, Energy for desalination: A state-of-the-art review, Desalination 491 (2020) 114569. https://doi.org/10.1016/j.desal.2020.114569.

[23] A.J. Schunke, G.A. Hernandez Herrera, L. Padhye, T.-A. Berry, Energy Recovery in SWRO Desalination: Current Status and New Possibilities, Frontiers in Sustainable Cities 2 (2020). https://www.frontiersin.org/articles/10.3389/frsc.2020.00009 (accessed September 15, 2023).

[24] E. Kadaj, R. Bosleman, Chapter 11 - Energy Recovery Devices in Membrane Desalination Processes, in: V.G. Gude (Ed.), Renewable Energy Powered Desalination Handbook, Butterworth-Heinemann, 2018: pp. 415–444. https://doi.org/10.1016/B978-0-12-815244-7.00011-8.

[25] T.M. Mansour, T.M. Ismail, K. Ramzy, M. Abd El-Salam, Energy recovery system in small reverse osmosis desalination plant: Experimental and theoretical investigations, Alexandria Engineering Journal 59 (2020) 3741–3753. https://doi.org/10.1016/j.aej.2020.06.030.

[26] N.M. Eshoul, B. Agnew, M.A. Al-Weshahi, M.S. Atab, Exergy Analysis of a Two-Pass Reverse Osmosis (RO) Desalination Unit with and without an Energy Recovery Turbine (ERT) and Pressure Exchanger (PX), Energies 8 (2015) 6910–6925. https://doi.org/10.3390/en8076910.

[27] D.M. Warsinger, E.W. Tow, K.G. Nayar, L.A. Maswadeh, J.H. Lienhard V, Energy efficiency of batch and semi-batch (CCRO) reverse osmosis desalination, Water Research 106 (2016) 272–282. https://doi.org/10.1016/j.watres.2016.09.029.

[28] Staged reverse osmosis operation: Configurations, energy efficiency, and application potential, Desalination 366 (2015) 9–14. https://doi.org/10.1016/j.desal.2015.02.043.

[29] M.M. Rashidi, I. Mahariq, N. Murshid, S. Wongwises, O. Mahian, M. Alhuyi Nazari, Applying wind energy as a clean source for reverse osmosis desalination: A comprehensive review, Alexandria Engineering Journal 61 (2022) 12977–12989. https://doi.org/10.1016/j.aej.2022.06.056.

[30] F. Greco, S.G.J. Heijman, A. Jarquin-Laguna, Integration of Wind Energy and Desalination Systems: A Review Study, Processes 9 (2021) 2181. https://doi.org/10.3390/pr9122181.

[31] Z. Triki, M.N. Bouaziz, M. Boumaza, Techno-economic feasibility of wind-powered reverse osmosis brackish water desalination systems in southern Algeria, Desalination and Water Treatment 52 (2014) 1745–1760. https://doi.org/10.1080/19443994.2013.807040.

[32] A wind-driven reverse osmosis system for aquaculture wastewater reuse and nutrient recovery – UHM Water Resources Research Center, (n.d.). https://www.wrrc.hawaii.edu/publication/a-wind-driven-reverse-osmosis-system-for-aquaculture-wastewater-reuse-and-nutrient-recovery/ (accessed July 31, 2023).

[33] A. Shukla, S. Agarwal, K. Narwat, Solar-Powered Reverse Osmosis Desalination, J. Phys.: Conf. Ser. 2178 (2022) 012018. https://doi.org/10.1088/1742-6596/2178/1/012018.

[34] M.W. Saleem, A. Abbas, M. Asim, G.M. Uddin, T.N. Chaudhary, A. Ullah, Design and cost estimation of solar powered reverse osmosis desalination system, Advances in Mechanical Engineering 13 (2021) 16878140211029090. https://doi.org/10.1177/16878140211029090.

[35] B. Rahimi, H. Shirvani, A.A. Alamolhoda, F. Farhadi, M. Karimi, A feasibility study of solar-powered reverse osmosis processes, Desalination 500 (2021) 114885. https://doi.org/10.1016/j.desal.2020.114885.

[36] S. Cheah, Photovoltaic Reverse Osmosis Desalination System, 2004. https://doi.org/10.13140/RG.2.1.1559.4724.

[37] C.S. Turchi, S. Akar, T. Cath, J. Vanneste, M. Geza, Use of Low-Temperature Geothermal Energy for Desalination in the Western United States, National Renewable Energy Lab. (NREL), Golden, CO (United States), 2015. https://doi.org/10.2172/1227955.

[38] M. Tajik Mansouri, M. Amidpour, J.M. Ponce-Ortega, Optimal integration of organic Rankine cycle and desalination systems with industrial processes: Energy-water-environment nexus, Applied Thermal Engineering 158 (2019) 113740. https://doi.org/10.1016/j.applthermaleng.2019.113740.

[39] V. Eveloy, P. Rodgers, L. Qiu, Hybrid gas turbine–organic Rankine cycle for seawater desalination by reverse osmosis in a hydrocarbon production facility, Energy Conversion and Management 106 (2015) 1134–1148. https://doi.org/10.1016/j.enconman.2015.10.019.

[40] G. Xia, Q. Sun, J. Wang, X. Cao, Y. Yu, L. Wang, Theoretical analysis of a reverse osmosis desalination system driven by solar-powered organic Rankine cycle and wind energy, Desalination and Water Treatment 53 (2015) 876–886. https://doi.org/10.1080/19443994.2014.927185.

[41] A.M. Delgado-Torres, L. García-Rodríguez, Preliminary design of seawater and brackish water reverse osmosis desalination systems driven by low-temperature solar organic Rankine cycles (ORC), Energy Conversion and Management 51 (2010) 2913–2920. https://doi.org/10.1016/j.enconman.2010.06.032.

[42] A.M. Delgado-Torres, L. García-Rodríguez, Design recommendations for solar organic Rankine cycle (ORC)–powered reverse osmosis (RO) desalination, Renewable and Sustainable Energy Reviews 16 (2012) 44–53. https://doi.org/10.1016/j.rser.2011.07.135.

[43] A. Liponi, A. Baccioli, D. Vera, L. Ferrari, Seawater desalination through reverse osmosis driven by ocean thermal energy conversion plant: Thermodynamic and economic feasibility, Applied Thermal Engineering 213 (2022) 118694. https://doi.org/10.1016/j.applthermaleng.2022.118694.

[44] P. Godart, Heat-driven direct reverse osmosis for high-performance and robust ad hoc seawater desalination, Desalination 500 (2021) 114800. https://doi.org/10.1016/j.desal.2020.114800.

[45] P. Godart, Design and simulation of a heat-driven direct reverse osmosis device for seawater desalination powered by solar thermal energy, Applied Energy 284 (2021) 116039. https://doi.org/10.1016/j.apenergy.2020.116039.

[46] J. Nihill, A. Date, P. Lappas, J. Velardo, Investigating the prospects of water desalination using a thermal water pump coupled with reverse osmosis membrane, Desalination 445 (2018) 256–265. https://doi.org/10.1016/j.desal.2018.08.004.

[47] M. Omerspahic, H. Al-Jabri, S.A. Siddiqui, I. Saadaoui, Characteristics of Desalination Brine and Its Impacts on Marine Chemistry and Health, With Emphasis on the Persian/Arabian Gulf: A Review, Frontiers in Marine Science 9 (2022). https://www.frontiersin.org/articles/10.3389/fmars.2022.845113 (accessed July 4, 2023).

[48] F. Helfer, C. Lemckert, Y.G. Anissimov, Osmotic power with Pressure Retarded Osmosis: Theory, performance and trends – A review, Journal of Membrane Science 453 (2014) 337–358. https://doi.org/10.1016/j.memsci.2013.10.053.

[49] G.S. Park, S.-M. Yoon, K.-S. Park, Impact of desalination byproducts on marine organisms: A case study at Chuja Island Desalination Plant in Korea, Desalination and Water Treatment 33 (2011) 267–272. https://doi.org/10.5004/dwt.2011.2651.

[50] PECC - Desalination chemical impact on Oceans, (n.d.). https://www.pecc.org/resources/environment-1/1780-desalination-chemical-impact-on-oceans (accessed July 4, 2023).

[51] M. Tedesco, C. Scalici, D. Vaccari, A. Cipollina, A. Tamburini, G. Micale, Performance of the first reverse electrodialysis pilot plant for power production from saline waters and concentrated brines, Journal of Membrane Science 500 (2016) 33–45. https://doi.org/10.1016/j.memsci.2015.10.057.

[52] X. Song, Z. Liu, D.D. Sun, Energy recovery from concentrated seawater brine by thin-film nanofiber composite pressure retarded osmosis membranes with high power density, Energy Environ. Sci. 6 (2013) 1199–1210. https://doi.org/10.1039/C3EE23349A.

[53] N.Y. Yip, M. Elimelech, Comparison of Energy Efficiency and Power Density in Pressure Retarded Osmosis and Reverse Electrodialysis, Environ. Sci. Technol. 48 (2014) 11002–11012. https://doi.org/10.1021/es5029316.

[54] D. Attarde, M. Jain, P.K. Singh, S.K. Gupta, Energy-efficient seawater desalination and wastewater treatment using osmotically driven membrane processes, Desalination 413 (2017) 86–100. https://doi.org/10.1016/j.desal.2017.03.010.

[55] S.H. Chae, J.H. Kim, A forecast for the environmental effect of pressure-retarded osmosis on CO2 emissions from seawater reverse osmosis in Korea: a scenario-based study, in: DESALINATION AND WATER TREATMENT, 2021: pp. 405–412. https://doi.org/10.5004/dwt.2021.26962.

[56] S. Lee, T. Park, Y.-G. Park, W. Lee, S.-H. Kim, Toward scale-up of seawater reverse osmosis (SWRO) – pressure retarded osmosis (PRO) hybrid system: A case study of a 240 m3/day pilot plant, Desalination 491 (2020) 114429. https://doi.org/10.1016/j.desal.2020.114429.

[57] C. Lee, S.H. Chae, E. Yang, S. Kim, J.H. Kim, I.S. Kim, A comprehensive review of the feasibility of pressure retarded osmosis: Recent technological advances and industrial efforts towards commercialization, Desalination 491 (2020) 114501. https://doi.org/10.1016/j.desal.2020.114501.

[58] C.F. Wan, T.-S. Chung, Techno-economic evaluation of various RO+PRO and RO+FO integrated processes, Applied Energy 212 (2018) 1038–1050. https://doi.org/10.1016/j.apenergy.2017.12.124.

[59] S. S., S. S., Reverse Osmosis–Pressure Retarded Osmosis hybrid system: Modelling, simulation and optimization, Desalination 389 (2016) 78–97. https://doi.org/10.1016/j.desal.2016.01.027.

[60] R. Makabe, T. Ueyama, H. Sakai, A. Tanioka, Commercial Pressure Retarded Osmosis Systems for Seawater Desalination Plants, Membranes 11 (2021) 69. https://doi.org/10.3390/membranes11010069.

[61] F. Helfer, C. Lemckert, Y.G. Anissimov, Osmotic power with Pressure Retarded Osmosis: Theory, performance and trends – A review, Journal of Membrane Science 453 (2014) 337–358. https://doi.org/10.1016/j.memsci.2013.10.053.

[62] R. Kempener, F. Neumann, Salinity Gradient Energy Technology Brief, The International Renewable Energy Agency (n.d.). https://www.irena.org/-/media/Files/IRENA/Agency/Publication/2014/Jun/Salinity_Energy_v4_WEB.pdf (accessed September 8, 2023).

[63] H.W. Chung, L.D. Banchik, J. Swaminathan, J.H. Lienhard V, On the present and future economic viability of stand-alone pressure-retarded osmosis, Desalination 408 (2017) 133–144. https://doi.org/10.1016/j.desal.2017.01.001.

[64] Y. Chen, A.A. Alanezi, J. Zhou, A. Altaee, M.H. Shaheed, Optimization of module pressure retarded osmosis membrane for maximum energy extraction, Journal of Water Process Engineering 32 (2019) 100935. https://doi.org/10.1016/j.jwpe.2019.100935.

[65] W. He, X. Luo, O. Kiselychnyk, J. Wang, M.H. Shaheed, Maximum power point tracking (MPPT) control of pressure retarded osmosis (PRO) salinity power plant: Development and comparison of different techniques, Desalination 389 (2016) 187–196. https://doi.org/10.1016/j.desal.2016.01.022.

[66] W. He, Y. Wang, M.H. Shaheed, Maximum power point tracking (MPPT) of a scale-up pressure retarded osmosis (PRO) osmotic power plant, Applied Energy 158 (2015) 584–596. https://doi.org/10.1016/j.apenergy.2015.08.059.

[67] C. Olkis, G. Santori, S. Brandani, An Adsorption Reverse Electrodialysis system for the generation of electricity from low-grade heat, Applied Energy 231 (2018) 222–234. https://doi.org/10.1016/j.apenergy.2018.09.112.

[68] J. Hu, S. Xu, X. Wu, D. Wu, D. Jin, P. Wang, Q. Leng, Theoretical simulation and evaluation for the performance of the hybrid multi-effect distillation—reverse electrodialysis power generation system, Desalination 443 (2018) 172–183. https://doi.org/10.1016/j.desal.2018.06.001.

[69] M. Papapetrou, G. Kosmadakis, A. Cipollina, U. La Commare, G. Micale, Industrial waste heat: Estimation of the technically available resource in the EU per industrial sector, temperature level and country, Applied Thermal Engineering 138 (2018) 207–216. https://doi.org/10.1016/j.applthermaleng.2018.04.043.

[70] A.S. Rattner, S. Garimella, Energy harvesting, reuse and upgrade to reduce primary energy usage in the USA, Energy 36 (2011) 6172–6183. https://doi.org/10.1016/j.energy.2011.07.047.

[71] D.D. Anastasio, J.T. Arena, E.A. Cole, J.R. McCutcheon, Impact of temperature on power density in closed-loop pressure retarded osmosis for grid storage, Journal of Membrane Science 479 (2015) 240–245. https://doi.org/10.1016/j.memsci.2014.12.046.

[72] Q. Wang, Z. Zhou, J. Li, Q. Tang, Y. Hu, Investigation of the reduced specific energy consumption of the RO-PRO hybrid system based on temperature-enhanced pressure retarded osmosis, Journal of Membrane Science 581 (2019) 439–452. https://doi.org/10.1016/j.memsci.2019.03.079.

[73] C.P. Koutsou, E. Kritikos, A.J. Karabelas, M. Kostoglou, Analysis of temperature effects on the specific energy consumption in reverse osmosis desalination processes, Desalination 476 (2020) 114213. https://doi.org/10.1016/j.desal.2019.114213.

[74] R.E. Pattle, Production of Electric Power by mixing Fresh and Salt Water in the Hydroelectric Pile, Nature 174 (1954) 660.

[75] B.E. Logan, M. Elimelech, Membrane-based processes for sustainable power generation using water., Nature 488 (2012) 313–319. https://doi.org/10.1038/nature11477.

[76] A. Achilli, A.E. Childress, Pressure retarded osmosis: From the vision of Sidney Loeb to the first prototype installation — Review, Desalination 261 (2010) 205–211. https://doi.org/10.1016/j.desal.2010.06.017.

[77] S. Sarp, Z. Li, J. Saththasivam, Pressure Retarded Osmosis (PRO): Past experiences, current developments, and future prospects, Desalination 389 (2016) 2–14. https://doi.org/10.1016/j.desal.2015.12.008.

[78] G.Z. Ramon, B.J. Feinberg, E.M. V Hoek, Membrane-based production of salinity-gradient power, Energy & Environmental Science 4 (2011) 4423–4434. https://doi.org/10.1039/C1EE01913A.

[79] R.S. Norman, Water Salination: A Source of Energy, Science 186 (1974) 350 LP – 352.

[80] S. Loeb, Production of energy from concentrated brines by pressure-retarded osmosis: I. Preliminary technical and economic correlations, Journal of Membrane Science 1 (1976) 49–63. https://doi.org/10.1016/S0376-7388(00)82257-7.

[81] J. Maisonneuve, C.B. Laflamme, P. Pillay, Experimental investigation of pressure retarded osmosis for renewable energy conversion: Towards increased net power, Applied Energy 164 (2016) 425–435. https://doi.org/10.1016/j.apenergy.2015.12.007.

[82] Y. Xu, X. Peng, C.Y. Tang, Q.S. Fu, S. Nie, Effect of draw solution concentration and operating conditions on forward osmosis and pressure retarded osmosis performance in a spiral wound module, Journal of Membrane Science 348 (2010) 298–309. https://doi.org/10.1016/j.memsci.2009.11.013.

[83] Y.C. Kim, S. Lee, Critical impact of permeate-to-feed ratio and feed flow rate fraction on performance of pressure-retarded osmosis process, Desalination 399 (2016) 128–137. https://doi.org/10.1016/j.desal.2016.08.022.

[84] X. Li, T.-S. Chung, Thin-film composite P84 co-polyimide hollow fiber membranes for osmotic power generation, Applied Energy 114 (2014) 600–610. https://doi.org/10.1016/j.apenergy.2013.10.037.

[85] Y. Chen, R. Vepa, M.H. Shaheed, Enhanced and speedy energy extraction from a scaled-up pressure retarded osmosis process with a whale optimization based maximum power point tracking, Energy 153 (2018) 618–627. https://doi.org/10.1016/j.energy.2018.04.052.

[86] S. Lin, A.P. Straub, M. Elimelech, Thermodynamic limits of extractable energy by pressure retarded osmosis, Energy & Environmental Science 7 (2014) 2706–2714. https://doi.org/10.1039/C4EE01020E.

[87] A. Altaee, J. Zhou, A. Alhathal Alanezi, G. Zaragoza, Pressure retarded osmosis process for power generation: Feasibility, energy balance and controlling parameters, Applied Energy 206 (2017) 303–311. https://doi.org/10.1016/j.apenergy.2017.08.195.

[88] N.Y. Yip, M. Elimelech, Performance Limiting Effects in Power Generation from Salinity Gradients by Pressure Retarded Osmosis, Environmental Science & Technology 45 (2011) 10273–10282. https://doi.org/10.1021/es203197e.

[89] M.F. Naguib, J. Maisonneuve, C.B. Laflamme, P. Pillay, Modeling pressure-retarded osmotic power in commercial length membranes, Renewable Energy 76 (2015) 619–627. https://doi.org/10.1016/j.renene.2014.11.048.

[90] S. Saravanan, N. Ramesh Babu, Maximum power point tracking algorithms for photovoltaic system – A review, Renewable and Sustainable Energy Reviews 57 (2016) 192–204. https://doi.org/10.1016/j.rser.2015.12.105.

[91] R. Tang, Z. Wu, Y. Fang, Maximum power point tracking of large-scale photovoltaic array, Solar Energy 134 (2016) 503–514. https://doi.org/10.1016/j.solener.2016.05.026.

[92] C. Huang, F. Li, Z. Jin, Maximum Power Point Tracking Strategy for Large-Scale Wind Generation Systems Considering Wind Turbine Dynamics, IEEE Transactions on Industrial Electronics 62 (2015) 2530–2539. https://doi.org/10.1109/TIE.2015.2395384.

[93] J. Schwinge, P.R. Neal, D.E. Wiley, D.F. Fletcher, A.G. Fane, Spiral wound modules and spacers: Review and analysis, Journal of Membrane Science 242 (2004) 129–153. https://doi.org/10.1016/j.memsci.2003.09.031.

[94] G. Schock, A. Miquel, Mass transfer and pressure loss in spiral wound modules, Desalination 64 (1987) 339–352. https://doi.org/10.1016/0011-9164(87)90107-X.

[95] R.S. Kaarthik, J. Maisonneuve, P. Pillay, Real-Time Emulation of a Pressure-Retarded Osmotic Power Generation System, IEEE Transactions on Industry Applications 53 (2017) 5768–5776. https://doi.org/10.1109/TIA.2017.2732939.

[96] J. Maisonneuve, P. Pillay, Introduction to PRO for energy conversion applications including an electric equivalent circuit, IET Renewable Power Generation 11 (2017) 115–122. https://doi.org/10.1049/iet-rpg.2016.0173.

[97] K.L. Hickenbottom, J. Vanneste, M. Elimelech, T.Y. Cath, Assessing the current state of commercially available membranes and spacers for energy production with pressure retarded osmosis, Desalination 389 (2016) 108–118. https://doi.org/10.1016/j.desal.2015.09.029.

[98] G. O'Toole, L. Jones, C. Coutinho, C. Hayes, M. Napoles, A. Achilli, River-to-sea pressure retarded osmosis: Resource utilization in a full-scale facility, Desalination 389 (2016) 39–51. https://doi.org/10.1016/j.desal.2016.01.012.

[99] S. Loeb, Large-scale power production by pressure-retarded osmosis, using river water and sea water passing through spiral modules, Desalination 143 (2002) 115–122. https://doi.org/10.1016/S0011-9164(02)00233-3.

[100] Q. She, X. Jin, C.Y. Tang, Osmotic power production from salinity gradient resource by pressure retarded osmosis: Effects of operating conditions and reverse solute diffusion, Journal of Membrane Science 401–402 (2012) 262–273. https://doi.org/10.1016/j.memsci.2012.02.014.

[101] Y.C. Kim, M. Elimelech, Potential of osmotic power generation by pressure retarded osmosis using seawater as feed solution: Analysis and experiments, Journal of Membrane Science 429 (2013) 330–337. https://doi.org/10.1016/j.memsci.2012.11.039.

[102] J.R. McCutcheon, M. Elimelech, Influence of concentrative and dilutive internal concentration polarization on flux behavior in forward osmosis, Journal of Membrane Science 284 (2006) 237–247. https://doi.org/10.1016/j.memsci.2006.07.049.

[103] Y. Chen, C.H. Loh, L. Zhang, L. Setiawan, Q. She, W. Fang, X. Hu, R. Wang, Module scale-up and performance evaluation of thin film composite hollow fiber membranes for pressure retarded osmosis, Journal of Membrane Science 548 (2018) 398–407. https://doi.org/10.1016/j.memsci.2017.11.036.

[104] M. Kim, S. Kim, Practical limit of energy production from seawater by full-scale pressure retarded osmosis, Energy 158 (2018) 373–382. https://doi.org/10.1016/j.energy.2018.06.042.

[105] G. Han, S. Zhang, X. Li, T.-S. Chung, High performance thin film composite pressure retarded osmosis (PRO) membranes for renewable salinity-gradient energy generation, Journal of Membrane Science 440 (2013) 108–121. https://doi.org/10.1016/j.memsci.2013.04.001.

[106] A. Achilli, T.Y. Cath, A.E. Childress, Power generation with pressure retarded osmosis: An experimental and theoretical investigation, Journal of Membrane Science 343 (2009) 42–52. https://doi.org/10.1016/j.memsci.2009.07.006.

[107] N.Y. Yip, M. Elimelech, Influence of Natural Organic Matter Fouling and Osmotic Backwash on Pressure Retarded Osmosis Energy Production from Natural Salinity Gradients, Environmental Science & Technology 47 (2013) 12607–12616. https://doi.org/10.1021/es403207m.

[108] E. Abbasi-Garravand, C.N. Mulligan, C.B. Laflamme, G. Clairet, Investigation of the fouling effect on a commercial semi-permeable membrane in the pressure retarded osmosis (PRO) process, Separation and Purification Technology 193 (2018) 81–90. https://doi.org/10.1016/j.seppur.2017.10.053.

[109] Q. She, R. Wang, A.G. Fane, C.Y. Tang, Membrane fouling in osmotically driven membrane processes: A review, Journal of Membrane Science 499 (2016) 201–233. https://doi.org/10.1016/j.memsci.2015.10.040.

[110] G. Han, J. Zhou, C. Wan, T. Yang, T.-S. Chung, Investigations of inorganic and organic fouling behaviors, antifouling and cleaning strategies for pressure retarded osmosis (PRO) membrane using seawater desalination brine and wastewater, Water Research 103 (2016) 264–275. https://doi.org/10.1016/j.watres.2016.07.040.

[111] Y. Chun, D. Mulcahy, L. Zou, I.S. Kim, A Short Review of Membrane Fouling in Forward Osmosis Processes, Membranes 7 (2017) 30. https://doi.org/10.3390/membranes7020030.

[112] W. He, J. Wang, Feasibility study of energy storage by concentrating/desalinating water: Concentrated Water Energy Storage, Applied Energy 185 (2017) 872–884. https://doi.org/10.1016/j.apenergy.2016.10.077.

[113] K. Saito, M. Irie, S. Zaitsu, H. Sakai, H. Hayashi, A. Tanioka, Power generation with salinity gradient by pressure retarded osmosis using concentrated brine from SWRO system and treated sewage as pure water, Desalination and Water Treatment 41 (2012) 114–121. https://doi.org/10.1080/19443994.2012.664696.

[114] J.L. Prante, J.A. Ruskowitz, A.E. Childress, A. Achilli, RO-PRO desalination: An integrated low-energy approach to seawater desalination, Applied Energy 120 (2014) 104–114. https://doi.org/10.1016/j.apenergy.2014.01.013.

[115] Z. Wang, D. Hou, S. Lin, Gross vs. net energy: Towards a rational framework for assessing the practical viability of pressure retarded osmosis, Journal of Membrane Science 503 (2016) 132–147. https://doi.org/10.1016/j.memsci.2015.11.035.

[116] A.P. Straub, A. Deshmukh, M. Elimelech, Pressure-retarded osmosis for power generation from salinity gradients: is it viable?, Energy & Environmental Science 9 (2016) 31–48. https://doi.org/10.1039/C5EE02985F.

[117] C.F. Wan, T.-S. Chung, Energy recovery by pressure retarded osmosis (PRO) in SWRO–PRO integrated processes, Applied Energy 162 (2016) 687–698. https://doi.org/10.1016/j.apenergy.2015.10.067.

[118] N.Y. Yip, M. Elimelech, Thermodynamic and Energy Efficiency Analysis of Power Generation from Natural Salinity Gradients by Pressure Retarded Osmosis, Environmental Science & Technology 46 (2012) 5230–5239. https://doi.org/10.1021/es300060m.

[119] K.K. Reimund, J.R. McCutcheon, A.D. Wilson, Thermodynamic analysis of energy density in pressure retarded osmosis: The impact of solution volumes and costs, Journal of Membrane Science 487 (2015) 240–248. https://doi.org/10.1016/j.memsci.2015.03.076.

[120] W. He, Y. Wang, M.H. Shaheed, Maximum power point tracking (MPPT) of a scale-up pressure retarded osmosis (PRO) osmotic power plant, Applied Energy 158 (2015) 584–596. https://doi.org/10.1016/j.apenergy.2015.08.059.

[121] W. He, X. Luo, O. Kiselychnyk, J. Wang, M.H. Shaheed, Maximum power point tracking (MPPT) control of pressure retarded osmosis (PRO) salinity power plant: Development and comparison of different techniques, Desalination 389 (2016) 187–196. https://doi.org/10.1016/j.desal.2016.01.022.

[122] Y. Chen, R. Vepa, M.H. Shaheed, Enhanced and speedy energy extraction from a scaled-up pressure retarded osmosis process with a whale optimization based maximum power point tracking, Energy 153 (2018) 618–627. https://doi.org/10.1016/j.energy.2018.04.052.

[123] J. Maisonneuve, S. Chintalacheruvu, Increasing osmotic power and energy with maximum power point tracking, Applied Energy 238 (2019) 683–695. https://doi.org/10.1016/j.apenergy.2019.01.110.

[124] Y. Xu, X. Peng, C.Y. Tang, Q.S. Fu, S. Nie, Effect of draw solution concentration and operating conditions on forward osmosis and pressure retarded osmosis

performance in a spiral wound module, Journal of Membrane Science 348 (2010) 298–309. https://doi.org/10.1016/j.memsci.2009.11.013.

[125] J. Maisonneuve, P. Pillay, C.B. Laflamme, Pressure-retarded osmotic power system model considering non-ideal effects, Renewable Energy 75 (2015) 416–424. https://doi.org/10.1016/j.renene.2014.10.011.

[126] J. Wang, Y. Deng, W. Sun, X. Zheng, Z. Cui, Maximum power point tracking method based on impedance matching for a micro hydropower generator, Applied Energy 340 (2023) 121003. https://doi.org/10.1016/j.apenergy.2023.121003.

[127] S. Pei Ye, Y. Hua Liu, S. Chung Wang, H. Yu Pai, A novel global maximum power point tracking algorithm based on Nelder-Mead simplex technique for complex partial shading conditions, Applied Energy 321 (2022) 119380. https://doi.org/10.1016/j.apenergy.2022.119380.

[128] L. Peng, S. Zheng, X. Chai, L. Li, A novel tangent error maximum power point tracking algorithm for photovoltaic system under fast multi-changing solar irradiances, Applied Energy 210 (2018) 303–316. https://doi.org/10.1016/j.apenergy.2017.11.017.

[129] J. Prasanth Ram, N. Rajasekar, A new robust, mutated and fast tracking LPSO method for solar PV maximum power point tracking under partial shaded conditions, Applied Energy 201 (2017) 45–59. https://doi.org/10.1016/j.apenergy.2017.05.102.

[130] S. Chintalacheruvu, Y. Ren, J. Maisonneuve, Effectively using heat to thermally enhance pressure retarded osmosis, Desalination 556 (2023) 116570. https://doi.org/10.1016/j.desal.2023.116570.

[131] E. Abbasi-Garravand, C.N. Mulligan, Feasibility of Pressure-Retarded Osmosis for Electricity Generation at Low Temperatures, Membranes 11 (2021) 556. https://doi.org/10.3390/membranes11080556.

[132] Y. Chen, L. Setiawan, S. Chou, X. Hu, R. Wang, Identification of safe and stable operation conditions for pressure retarded osmosis with high performance hollow fiber membrane, Journal of Membrane Science 503 (2016) 90–100. https://doi.org/10.1016/j.memsci.2015.12.041.

[133] G. Han, Q. Ge, T.-S. Chung, Conceptual demonstration of novel closed-loop pressure retarded osmosis process for sustainable osmotic energy generation, Applied Energy 132 (2014) 383–393. https://doi.org/10.1016/j.apenergy.2014.07.029.

[134] N.Y. Yip, A. Tiraferri, W.A. Phillip, J.D. Schiffman, L.A. Hoover, Y.C. Kim, M. Elimelech, Thin-Film Composite Pressure Retarded Osmosis Membranes for

Sustainable Power Generation from Salinity Gradients, Environ. Sci. Technol. 45 (2011) 4360–4369. https://doi.org/10.1021/es104325z.

[135] Y. Chen, Z. Shi, B. Xu, M.H. Shaheed, Optimal design of a scaled-up PRO system using swarm intelligence approach, Sci. China Inf. Sci. 64 (2021) 222203. https://doi.org/10.1007/s11432-020-3110-x.

[136] American-Made Challenges: Solar Desalination Prize, Energy.Gov (n.d.). https://www.energy.gov/eere/solar/american-made-challenges-solar-desalination-prize (accessed March 21, 2021).

[137] Z. Wang, T. Horseman, A.P. Straub, N.Y. Yip, D. Li, M. Elimelech, S. Lin, Pathways and challenges for efficient solar-thermal desalination, Sci. Adv. 5 (2019) eaax0763. https://doi.org/10.1126/sciadv.aax0763.

[138] A. Deshmukh, C. Boo, V. Karanikola, S. Lin, A.P. Straub, T. Tong, D.M. Warsinger, M. Elimelech, Membrane distillation at the water-energy nexus: limits, opportunities, and challenges, Energy Environ. Sci. 11 (2018) 1177–1196. https://doi.org/10.1039/C8EE00291F.

[139] A. Ali, R.A. Tufa, F. Macedonio, E. Curcio, E. Drioli, Membrane technology in renewable-energy-driven desalination, Renewable and Sustainable Energy Reviews 81 (2018) 1–21. https://doi.org/10.1016/j.rser.2017.07.047.

[140] E. Drioli, A. Ali, F. Macedonio, Membrane distillation: Recent developments and perspectives, Desalination 356 (2015) 56–84. https://doi.org/10.1016/j.desal.2014.10.028.

[141] E. Chiavazzo, M. Morciano, F. Viglino, M. Fasano, Passive high-yield seawater desalination at below one sun by modular and low-cost distillation, (n.d.) 61.

[142] A.P. Straub, M. Elimelech, Energy Efficiency and Performance Limiting Effects in Thermo-Osmotic Energy Conversion from Low-Grade Heat, Environ. Sci. Technol. 51 (2017) 12925–12937. https://doi.org/10.1021/acs.est.7b02213.

[143] A.P. Straub, N.Y. Yip, S. Lin, J. Lee, M. Elimelech, Harvesting low-grade heat energy using thermo-osmotic vapour transport through nanoporous membranes, Nature Energy 1 (2016) 1–6. https://doi.org/10.1038/nenergy.2016.90.

[144] H. Gong, D.D. Anastasio, K. Wang, J.R. McCutcheon, Finding better draw solutes for osmotic heat engines: Understanding transport of ions during pressure retarded osmosis, Desalination 421 (2017) 32–39. https://doi.org/10.1016/j.desal.2017.03.030.

[145] K.L. Hickenbottom, J. Vanneste, T.Y. Cath, Assessment of alternative draw solutions for optimized performance of a closed-loop osmotic heat engine, Journal

of Membrane Science 504 (2016) 162–175. https://doi.org/10.1016/j.memsci.2016.01.001.

[146] S. Lin, N.Y. Yip, T.Y. Cath, C.O. Osuji, M. Elimelech, Hybrid Pressure Retarded Osmosis–Membrane Distillation System for Power Generation from Low-Grade Heat: Thermodynamic Analysis and Energy Efficiency, Environ. Sci. Technol. 48 (2014) 5306–5313. https://doi.org/10.1021/es405173b.

[147] R.L. McGinnis, J.R. McCutcheon, M. Elimelech, A novel ammonia–carbon dioxide osmotic heat engine for power generation, Journal of Membrane Science 305 (2007) 13–19. https://doi.org/10.1016/j.memsci.2007.08.027.

[148] S.J. Einarsson, B. Wu, Thermal associated pressure-retarded osmosis processes for energy production: A review, Science of The Total Environment 757 (2021) 143731. https://doi.org/10.1016/j.scitotenv.2020.143731.

[149] B.A. Abdelkader, M.H. Sharqawy, Temperature effects on salinity gradient energy harvesting and utilized membrane properties – Experimental and numerical investigation, Sustainable Energy Technologies and Assessments 48 (2021) 101666. https://doi.org/10.1016/j.seta.2021.101666.

[150] Q. Wang, H. Cheng, J. Wang, Z. Ma, Z. Liu, Z. Sun, D. Xu, J. Gao, X. Gao, Temperature-enhanced pressure retarded osmosis powered by solar energy: Experimental validation, economic consideration, and potential implication, Chemical Engineering Research and Design 170 (2021) 380–388. https://doi.org/10.1016/j.cherd.2021.04.024.

[151] S. Adhikary, Md.S. Islam, K. Touati, S. Sultana, A.S. Ramamurthy, Md.S. Rahaman, Increased power density with low salt flux using organic draw solutions for pressure-retarded osmosis at elevated temperatures, Desalination 484 (2020) 114420. https://doi.org/10.1016/j.desal.2020.114420.

[152] E. Sivertsen, T. Holt, W.R. Thelin, Concentration and Temperature Effects on Water and Salt Permeabilities in Osmosis and Implications in Pressure-Retarded Osmosis, Membranes 8 (2018) 39. https://doi.org/10.3390/membranes8030039.

[153] K. Touati, F. Tadeo, Study of the Reverse Salt Diffusion in pressure retarded osmosis: Influence on concentration polarization and effect of the operating conditions, Desalination 389 (2016) 171–186. https://doi.org/10.1016/j.desal.2016.02.014.

[154] K. Touati, F. Tadeo, C. Hänel, T. Schiestel, Effect of the operating temperature on hydrodynamics and membrane parameters in pressure retarded osmosis, Desalination and Water Treatment 57 (2016) 10477–10489. https://doi.org/10.1080/19443994.2015.1039600.

[155] K. Touati, C. Hänel, F. Tadeo, T. Schiestel, Effect of the feed and draw solution temperatures on PRO performance: Theoretical and experimental study, Desalination 365 (2015) 182–195. https://doi.org/10.1016/j.desal.2015.02.016.

[156] Y.C. Kim, M. Elimelech, Potential of osmotic power generation by pressure retarded osmosis using seawater as feed solution: Analysis and experiments, Journal of Membrane Science 429 (2013) 330–337. https://doi.org/10.1016/j.memsci.2012.11.039.

[157] Q. She, X. Jin, C.Y. Tang, Osmotic power production from salinity gradient resource by pressure retarded osmosis: Effects of operating conditions and reverse solute diffusion, Journal of Membrane Science 401–402 (2012) 262–273. https://doi.org/10.1016/j.memsci.2012.02.014.

[158] B.E. Logan, M. Elimelech, Membrane-based processes for sustainable power generation using water, Nature 488 (2012) 313–319. https://doi.org/10.1038/nature11477.

[159] S. Loeb, Production of energy from concentrated brines by pressure-retarded osmosis: I. Preliminary technical and economic correlations, Journal of Membrane Science 1 (1976) 49–63. https://doi.org/10.1016/S0376-7388(00)82257-7.

[160] R.S. Norman, Water Salination: A Source of Energy, Science 186 (1974) 350–352. https://doi.org/10.1126/science.186.4161.350.

[161] R.E. Pattle, Production of Electric Power by mixing Fresh and Salt Water in the Hydroelectric Pile, Nature 174 (1954) 660–660. https://doi.org/10.1038/174660a0.

[162] H.W. Chung, J. Swaminathan, L.D. Banchik, J.H. Lienhard, Economic framework for net power density and levelized cost of electricity in pressure-retarded osmosis, Desalination 448 (2018) 13–20. https://doi.org/10.1016/j.desal.2018.09.007.

[163] A.P. Straub, A. Deshmukh, M. Elimelech, Pressure-retarded osmosis for power generation from salinity gradients: is it viable?, Energy Environ. Sci. 9 (2016) 31–48. https://doi.org/10.1039/C5EE02985F.

[164] J. Maisonneuve, P. Pillay, C.B. Laflamme, Osmotic power potential in remote regions of Quebec, Renewable Energy 81 (2015) 62–70. https://doi.org/10.1016/j.renene.2015.03.015.

[165] R. Makabe, T. Ueyama, H. Sakai, A. Tanioka, Commercial Pressure Retarded Osmosis Systems for Seawater Desalination Plants, Membranes 11 (2021) 69. https://doi.org/10.3390/membranes11010069.

[166] C.F. Wan, T.-S. Chung, Techno-economic evaluation of various RO+PRO and RO+FO integrated processes, Applied Energy 212 (2018) 1038–1050. https://doi.org/10.1016/j.apenergy.2017.12.124.

[167] A. Achilli, J.L. Prante, N.T. Hancock, E.B. Maxwell, A.E. Childress, Experimental Results from RO-PRO: A Next Generation System for Low-Energy Desalination, Environ. Sci. Technol. 48 (2014) 6437–6443. https://doi.org/10.1021/es405556s.

[168] N. Asghar, H. Lee, D. Jang, A. Jang, Recovery of volatile fatty acids using forward osmosis: Influence of solution chemistry, temperature, and membrane orientation, Chemosphere 303 (2022) 134814. https://doi.org/10.1016/j.chemosphere.2022.134814.

[169] W.-J. Kim, O. Campanella, D.R. Heldman, A stepwise approach to predict the performance of forward osmosis operation: Effect of temperature and flow direction, Desalination 538 (2022) 115889. https://doi.org/10.1016/j.desal.2022.115889.

[170] M.S. Nawaz, T. Alamoudi, S. Soukane, M. Obaid, N. Ghaffour, Effect of colder stream temperature control on energy utilization, flux, RSF, and membrane integrity in asymmetric temperature FO systems, Process Safety and Environmental Protection 161 (2022) 67–77. https://doi.org/10.1016/j.psep.2022.02.070.

[171] Q. Wang, Z. Zhou, J. Li, Q. Tang, Y. Hu, Modeling and measurement of temperature and draw solution concentration induced water flux increment efficiencies in the forward osmosis membrane process, Desalination 452 (2019) 75–86. https://doi.org/10.1016/j.desal.2018.11.001.

[172] M.R. Chowdhury, J.R. McCutcheon, Elucidating the impact of temperature gradients across membranes during forward osmosis: Coupling heat and mass transfer models for better prediction of real osmotic systems, Journal of Membrane Science 553 (2018) 189–199. https://doi.org/10.1016/j.memsci.2018.01.004.

[173] A.H. Hawari, N. Kamal, A. Altaee, Combined influence of temperature and flow rate of feeds on the performance of forward osmosis, Desalination 398 (2016) 98–105. https://doi.org/10.1016/j.desal.2016.07.023.

[174] N.-N. Bui, J.T. Arena, J.R. McCutcheon, Proper accounting of mass transfer resistances in forward osmosis: Improving the accuracy of model predictions of structural parameter, Journal of Membrane Science 492 (2015) 289–302. https://doi.org/10.1016/j.memsci.2015.02.001.

[175] M. Xie, W. Price, L. Nghiem, M. Elimelech, Effects of feed and draw solution temperature and transmembrane temperature difference on the rejection of trace organic contaminants by forward osmosis, Faculty of Engineering and Information Sciences - Papers: Part A (2013) 57–64. https://doi.org/10.1016/j.memsci.2013.03.031.

[176] S. Phuntsho, S. Vigneswaran, J. Kandasamy, S. Hong, S. Lee, H.K. Shon, Influence of temperature and temperature difference in the performance of forward osmosis desalination process, Journal of Membrane Science 415–416 (2012) 734–744. https://doi.org/10.1016/j.memsci.2012.05.065.

[177] S.-J. You, X.-H. Wang, M. Zhong, Y.-J. Zhong, C. Yu, N.-Q. Ren, Temperature as a factor affecting transmembrane water flux in forward osmosis: Steady-state modeling and experimental validation, Chemical Engineering Journal 198–199 (2012) 52–60. https://doi.org/10.1016/j.cej.2012.05.087.

[178] S. Zhao, L. Zou, Effects of working temperature on separation performance, membrane scaling and cleaning in forward osmosis desalination, Desalination 278 (2011) 157–164. https://doi.org/10.1016/j.desal.2011.05.018.

[179] J. Kim, K. Park, S. Hong, Application of two-stage reverse osmosis system for desalination of high-salinity and high-temperature seawater with improved stability and performance, Desalination 492 (2020) 114645. https://doi.org/10.1016/j.desal.2020.114645.

[180] A. Jawor, E.M.V. Hoek, Effects of feed water temperature on inorganic fouling of brackish water RO membranes, Desalination 235 (2009) 44–57. https://doi.org/10.1016/j.desal.2008.07.004.

[181] L. Feng, L. Xie, G. Suo, X. Shao, T. Dong, Influence of Temperature on the Performance of Forward Osmosis Using Ammonium Bicarbonate as Draw Solute, Trans. Tianjin Univ. 24 (2018) 571–579. https://doi.org/10.1007/s12209-018-0159-1.

[182] J.F. Comesaña, J.J. Otero, E. Camesella, A. Correa, Densities and Viscosities of Ternary Systems of Water + Fructose + Sodium Chloride from 20 to 40 °C, J. Chem. Eng. Data 46 (2001) 1153–1155. https://doi.org/10.1021/je000265t.

[183] M. Mulder, Characterisation of Membranes, in: M. Mulder (Ed.), Basic Principles of Membrane Technology, Springer Netherlands, Dordrecht, 1996: pp. 157–209. https://doi.org/10.1007/978-94-009-1766-8_4.

[184] M.R. Chowdhury, J. Ren, K. Reimund, J.R. McCutcheon, A hybrid dead-end/cross-flow forward osmosis system for evaluating osmotic flux performance at high recovery of produced water, Desalination 421 (2017) 127–134. https://doi.org/10.1016/j.desal.2016.08.021.

[185] J. Ren, M.R. Chowdhury, L. Xia, C. Ma, G.M. Bollas, J.R. McCutcheon, A computational fluid dynamics model to predict performance of hollow fiber membrane modules in forward osmosis, Journal of Membrane Science 603 (2020) 117973. https://doi.org/10.1016/j.memsci.2020.117973.

[186] J. Maisonneuve, C.B. Laflamme, P. Pillay, Experimental investigation of pressure retarded osmosis for renewable energy conversion: Towards increased net power, Applied Energy 164 (2016) 425–435. https://doi.org/10.1016/j.apenergy.2015.12.007.

[187] J.R. McCutcheon, M. Elimelech, Influence of concentrative and dilutive internal concentration polarization on flux behavior in forward osmosis, Journal of Membrane Science 284 (2006) 237–247. https://doi.org/10.1016/j.memsci.2006.07.049.

[188] G.T. Gray, J.R. McCutcheon, M. Elimelech, Internal concentration polarization in forward osmosis: role of membrane orientation, Desalination 197 (2006) 1–8. https://doi.org/10.1016/j.desal.2006.02.003.

[189] G.D. Mehta, S. Loeb, Internal polarization in the porous substructure of a semipermeable membrane under pressure-retarded osmosis, Journal of Membrane Science 4 (1978) 261–265. https://doi.org/10.1016/S0376-7388(00)83301-3.

[190] J. Huang, T. Tang, Y. He, Coupling photothermal and Joule-heating conversion for self-heating membrane distillation enhancement, Applied Thermal Engineering 199 (2021) 117557. https://doi.org/10.1016/j.applthermaleng.2021.117557.

[191] A. Alabastri, P.D. Dongare, O. Neumann, J. Metz, I. Adebiyi, P. Nordlander, N.J. Halas, Resonant energy transfer enhances solar thermal desalination, Energy Environ. Sci. 13 (2020) 968–976. https://doi.org/10.1039/C9EE03256H.

[192] J. Huang, Y. Hu, Y. Bai, Y. He, J. Zhu, Novel solar membrane distillation enabled by a PDMS/CNT/PVDF membrane with localized heating, Desalination 489 (2020) 114529. https://doi.org/10.1016/j.desal.2020.114529.

[193] H. Ye, X. Li, L. Deng, P. Li, T. Zhang, X. Wang, B.S. Hsiao, Silver Nanoparticle-Enabled Photothermal Nanofibrous Membrane for Light-Driven Membrane Distillation, Ind. Eng. Chem. Res. 58 (2019) 3269–3281. https://doi.org/10.1021/acs.iecr.8b04708.

[194] A. Alsaati, A.M. Marconnet, Energy efficient membrane distillation through localized heating, Desalination 442 (2018) 99–107. https://doi.org/10.1016/j.desal.2018.05.009.

[195] C. Boo, M. Elimelech, Carbon nanotubes keep up the heat, Nature Nanotech 12 (2017) 501–503. https://doi.org/10.1038/nnano.2017.114.

[196] P.D. Dongare, A. Alabastri, S. Pedersen, K.R. Zodrow, N.J. Hogan, O. Neumann, J. Wu, T. Wang, A. Deshmukh, M. Elimelech, Q. Li, P. Nordlander, N.J. Halas, Nanophotonics-enabled solar membrane distillation for off-grid water purification,

Proceedings of the National Academy of Sciences 114 (2017) 6936–6941. https://doi.org/10.1073/pnas.1701835114.

[197] L. Hao, W. Xin, L. Jin, K. Weimin, C. Bowen, H. Lei, X. Yan, Fabrication and characterization of nano-SiC/ thermoplastic polyurethane hybrid heating membranes based on fine silver filaments, Journal of Applied Polymer Science 132 (2015). https://doi.org/10.1002/app.41498.

[198] E.K. Summers, J.H. Lienhard, Experimental study of thermal performance in air gap membrane distillation systems, including the direct solar heating of membranes, Desalination 330 (2013) 100–111. https://doi.org/10.1016/j.desal.2013.09.023.

[199] Y. Li, T. Verbiest, I. Vankelecom, Improving the flux of PDMS membranes via localized heating through incorporation of gold nanoparticles, Journal of Membrane Science 428 (2013) 63–69. https://doi.org/10.1016/j.memsci.2012.10.050.

[200] E.K. Summers, J.H. Lienhard V, A novel solar-driven air gap membrane distillation system, Desalination and Water Treatment 51 (2013) 1344–1351. https://doi.org/10.1080/19443994.2012.705096.

[201] N.-N. Bui, J.R. McCutcheon, Nanoparticle-embedded nanofibers in highly permselective thin-film nanocomposite membranes for forward osmosis, Journal of Membrane Science 518 (2016) 338–346. https://doi.org/10.1016/j.memsci.2016.06.024.

[202] M.C.Y. Wong, K. Martinez, G.Z. Ramon, E.M.V. Hoek, Impacts of operating conditions and solution chemistry on osmotic membrane structure and performance, (2012). https://doi.org/10.1016/j.desal.2011.10.013.

[203] A. Achilli, T.Y. Cath, A.E. Childress, Power generation with pressure retarded osmosis: An experimental and theoretical investigation, Journal of Membrane Science 343 (2009) 42–52. https://doi.org/10.1016/j.memsci.2009.07.006.

[204] C.R. Martinetti, A.E. Childress, T.Y. Cath, High recovery of concentrated RO brines using forward osmosis and membrane distillation, Journal of Membrane Science 331 (2009) 31–39. https://doi.org/10.1016/j.memsci.2009.01.003.

[205] J.R. McCutcheon, R.L. McGinnis, M. Elimelech, A novel ammonia—carbon dioxide forward (direct) osmosis desalination process, Desalination 174 (2005) 1–11. https://doi.org/10.1016/j.desal.2004.11.002.

[206] T.Y. Cath, M. Elimelech, J.R. McCutcheon, R.L. McGinnis, A. Achilli, D. Anastasio, A.R. Brady, A.E. Childress, I.V. Farr, N.T. Hancock, J. Lampi, L.D. Nghiem, M. Xie, N.Y. Yip, Standard Methodology for Evaluating Membrane

Performance in Osmotically Driven Membrane Processes, Desalination 312 (2013) 31–38. https://doi.org/10.1016/j.desal.2012.07.005.

[207] D.A. Nield, A. Bejan, Heat Transfer Through a Porous Medium, in: D.A. Nield, A. Bejan (Eds.), Convection in Porous Media, Springer, New York, NY, 2013: pp. 31–46. https://doi.org/10.1007/978-1-4614-5541-7_2.

[208] J. Maisonneuve, Osmotic Power for Remote Communities in Quebec, phd, Concordia University, 2015. https://spectrum.library.concordia.ca/id/eprint/980383/ (accessed August 20, 2022).

[209] A. Bhinder, S. Shabani, M. Sadrzadeh, Effect of Internal and External Concentration Polarizations on the Performance of Forward Osmosis Process, IntechOpen, 2017. https://doi.org/10.5772/intechopen.71343.

[210] J. Wang, D.S. Dlamini, A.K. Mishra, M.T.M. Pendergast, M.C.Y. Wong, B.B. Mamba, V. Freger, A.R.D. Verliefde, E.M.V. Hoek, A critical review of transport through osmotic membranes, Journal of Membrane Science 454 (2014) 516–537. https://doi.org/10.1016/j.memsci.2013.12.034.

[211] G. Guillen, E.M.V. Hoek, Modeling the impacts of feed spacer geometry on reverse osmosis and nanofiltration processes, Chemical Engineering Journal 149 (2009) 221–231. https://doi.org/10.1016/j.cej.2008.10.030.

[212] C.H. Tan, H.Y. Ng, Modified models to predict flux behavior in forward osmosis in consideration of external and internal concentration polarizations, Journal of Membrane Science 324 (2008) 209–219. https://doi.org/10.1016/j.memsci.2008.07.020.

[213] W.M.. Kays M.E.. Crawford B. Weigand, Convective Heat and Mass Transfer, Mc Graw Hill (2005).

[214] J.R. Welty, Fundamentals of momentum, heat, and mass transfer, 3rd ed., Wiley, New York, 1984.

[215] Q.L. Ve, K. Rahaoui, M. Bawahab, H. Faqeha, A. Date, A. Akbarzadeh, M.C. Do, Q.L. Nguyen, Experimental Investigation of Heat Transfer Correlation for Direct Contact Membrane Distillation, J. Heat Transfer 142 (2020). https://doi.org/10.1115/1.4044707.

[216] S.M.F. Hasani, A.S. Sowayan, M. Shakaib, The Effect of Spacer Orientations on Temperature Polarization in a Direct Contact Membrane Distillation Process Using 3-d CFD Modeling, Arabian Journal for Science & Engineering (Springer Science & Business Media B.V.) 44 (2019) 10269–10284. https://doi.org/10.1007/s13369-019-04089-x.

[217] B. Ravindra Babu, N.K. Rastogi, K.S.M.S. Raghavarao, Concentration and temperature polarization effects during osmotic membrane distillation, Journal of Membrane Science 322 (2008) 146–153. https://doi.org/10.1016/j.memsci.2008.05.041.

[218] M. Gryta, M. Tomaszewska, A.W. Morawski, Membrane distillation with laminar flow, Separation and Purification Technology 11 (1997) 93–101. https://doi.org/10.1016/S1383-5866(97)00002-6.

[219] L. Wen-Chien, J. Yi-Hsu, Conjugate Leveque solution for Newtonian fluid in a parallel plate channel, International Journal of Heat and Mass Transfer 29 (1986) 941–947. https://doi.org/10.1016/0017-9310(86)90189-4.

[220] R.G. Greenkorn, Chapter 7 Heat transfer models, Momentum, Heat, and Mass Transfer Fundamentals, (1999). https://web-p-ebscohost-com.huaryu.kl.oakland.edu/ehost/ebookviewer/ebook/bmxlYmtfXzEyODIwX19BTg2?sid=ac8bfc1a-f5fa-4d1b-83a3-33780856fd0d@redis&vid=4&format=EB&rid=1 (accessed August 31, 2022).

[221] J. Lee, N. Ghaffour, Predicting the performance of large-scale forward osmosis module using spatial variation model: Effect of operating parameters including temperature, Desalination 469 (2019) 114095. https://doi.org/10.1016/j.desal.2019.114095.

[222] Ó. Andrjesdóttir, C.L. Ong, M. Nabavi, S. Paredes, A.S.G. Khalil, B. Michel, D. Poulikakos, An experimentally optimized model for heat and mass transfer in direct contact membrane distillation, International Journal of Heat and Mass Transfer 66 (2013) 855–867. https://doi.org/10.1016/j.ijheatmasstransfer.2013.07.051.

[223] L. Martínez, F.J. Florido-Díaz, Theoretical and experimental studies on desalination using membrane distillation, Desalination 139 (2001) 373–379. https://doi.org/10.1016/S0011-9164(01)00335-6.

[224] J. Maisonneuve, S. Chintalacheruvu, Increasing osmotic power and energy with maximum power point tracking, Applied Energy 238 (2019) 683–695. https://doi.org/10.1016/j.apenergy.2019.01.110.

[225] A. Abdelrasoul, H. Doan, A. Lohi, C.-H. Cheng, Mass Transfer Mechanisms and Transport Resistances in Membrane Separation Process, IntechOpen, 2015. https://doi.org/10.5772/60866.

[226] Z. Wang, T. Horseman, A.P. Straub, N.Y. Yip, D. Li, M. Elimelech, S. Lin, Pathways and challenges for efficient solar-thermal desalination, Sci Adv 5 (2019) eaax0763. https://doi.org/10.1126/sciadv.aax0763.

[227] A. Deshmukh, C. Boo, V. Karanikola, S. Lin, A.P. Straub, T. Tong, D.M. Warsinger, M. Elimelech, Membrane distillation at the water-energy nexus: limits, opportunities, and challenges, Energy Environ. Sci. 11 (2018) 1177–1196. https://doi.org/10.1039/C8EE00291F.

[228] M. Alsehli, J.-K. Choi, M. Aljuhan, A novel design for a solar powered multistage flash desalination, Solar Energy 153 (2017) 348–359. https://doi.org/10.1016/j.solener.2017.05.082.

[229] S.P. Agashichev, K.N. Lootahb, Influence of temperature and permeate recovery on energy consumption of a reverse osmosis system, Desalination 154 (2003) 253–266. https://doi.org/10.1016/S0011-9164(03)80041-3.

[230] J. Kim, K. Park, S. Hong, Application of two-stage reverse osmosis system for desalination of high-salinity and high-temperature seawater with improved stability and performance, Desalination 492 (2020) 114645. https://doi.org/10.1016/j.desal.2020.114645.

[231] S. Shaaban, H. Yahya, Detailed analysis of reverse osmosis systems in hot climate conditions, Desalination 423 (2017) 41–51. https://doi.org/10.1016/j.desal.2017.09.002.

[232] C. Chen, X. Huang, P. Prakash, S. Chilekar, R. Franks, Produced water desalination using high temperature membranes, Desalination 513 (2021) 115144. https://doi.org/10.1016/j.desal.2021.115144.

[233] B. Moossa, P. Trivedi, H. Saleem, S.J. Zaidi, Desalination in the GCC countries- a review, Journal of Cleaner Production 357 (2022) 131717. https://doi.org/10.1016/j.jclepro.2022.131717.

[234] H. Sitaraman, I. Battiato, Impact of large-scale effects on mass transfer and concentration polarization in Reverse Osmosis membrane systems, Separation and Purification Technology 303 (2022) 122121. https://doi.org/10.1016/j.seppur.2022.122121.

[235] C.P. Koutsou, A.J. Karabelas, M. Kostoglou, Membrane desalination under constant water recovery – The effect of module design parameters on system performance, Separation and Purification Technology 147 (2015) 90–113. https://doi.org/10.1016/j.seppur.2015.04.012.

[236] S. Sundaramoorthy, G. Srinivasan, D.V.R. Murthy, An analytical model for spiral wound reverse osmosis membrane modules: Part I — Model development and parameter estimation, Desalination 280 (2011) 403–411. https://doi.org/10.1016/j.desal.2011.03.047.

[237] G.E. Dévora-Isiordia, C.A. Cásares-De la Torre, D.P. Morales-Mendívil, R. Montoya-Pizeno, N. Velázquez-Limón, J.A. Aguilar-Jiménez, J. Ríos-Arriola, Evaluation of Concentration Polarization Due to the Effect of Feed Water Temperature Change on Reverse Osmosis Membranes, Membranes (Basel) 13 (2022) 3. https://doi.org/10.3390/membranes13010003.

[238] S. Kim, E.M.V. Hoek, Modeling concentration polarization in reverse osmosis processes, Desalination 186 (2005) 111–128. https://doi.org/10.1016/j.desal.2005.05.017.

[239] A. Joseph, V. Damodaran, Dynamic simulation of the reverse osmosis process for seawater using LabVIEW and an analysis of the process performance, Computers & Chemical Engineering 121 (2019) 294–305. https://doi.org/10.1016/j.compchemeng.2018.11.001.

[240] J. Kim, S. Hong, Optimizing seawater reverse osmosis with internally staged design to improve product water quality and energy efficiency, Journal of Membrane Science 568 (2018) 76–86. https://doi.org/10.1016/j.memsci.2018.09.046.

[241] O. US EPA, Secondary Drinking Water Standards: Guidance for Nuisance Chemicals, (2015). https://www.epa.gov/sdwa/secondary-drinking-water-standards-guidance-nuisance-chemicals (accessed July 7, 2023).

[242] H. Canada, Guidelines for Canadian Drinking Water Quality: Guideline Technical Document – Total Dissolved Solids (TDS), (1997). https://www.canada.ca/en/health-canada/services/publications/healthy-living/guidelines-canadian-drinking-water-quality-guideline-technical-document-total-dissolved-solids-tds.html (accessed July 7, 2023).

[243] O.M.A. Al-hotmani, M.A. Al-Obaidi, Y.M. John, R. Patel, I.M. Mujtaba, Optimisation of hybrid MED-TVC and double reverse osmosis processes for producing different grades of water in a smart city, Desalination 534 (2022) 115776. https://doi.org/10.1016/j.desal.2022.115776.

[244] M. Xie, J. Lee, L.D. Nghiem, M. Elimelech, Role of pressure in organic fouling in forward osmosis and reverse osmosis, Journal of Membrane Science 493 (2015) 748–754. https://doi.org/10.1016/j.memsci.2015.07.033.

[245] Energy Conservation Program for Consumer Products: Representative Average Unit Costs of Energy, Office of Energy Efficiency and Renewable Energy, Department of Energy (n.d.). https://www.energy.gov/eere/buildings/articles/representatice-average-unit-cost-energy (accessed August 28, 2023).

[246] A.A. Atia, N.Y. Yip, V. Fthenakis, Pathways for minimal and zero liquid discharge with enhanced reverse osmosis technologies: Module-scale modeling and techno-economic assessment, Desalination 509 (2021) 115069. https://doi.org/10.1016/j.desal.2021.115069.

[247] A. Alkhudhiri, N. Darwish, N. Hilal, Membrane distillation: A comprehensive review, Desalination 287 (2012) 2–18. https://doi.org/10.1016/j.desal.2011.08.027.

[248] Z. Yang, H. Guo, C.Y. Tang, The upper bound of thin-film composite (TFC) polyamide membranes for desalination, Journal of Membrane Science 590 (2019) 117297. https://doi.org/10.1016/j.memsci.2019.117297.

[249] J.R. Werber, C.O. Osuji, M. Elimelech, Materials for next-generation desalination and water purification membranes, Nat Rev Mater 1 (2016) 1–15. https://doi.org/10.1038/natrevmats.2016.18.

[250] G.M. Geise, H.B. Park, A.C. Sagle, B.D. Freeman, J.E. McGrath, Water permeability and water/salt selectivity tradeoff in polymers for desalination, Journal of Membrane Science 369 (2011) 130–138. https://doi.org/10.1016/j.memsci.2010.11.054.

[251] The Unexpected Performance of Highly Permeable SWRO Membranes at High Temperatures, (n.d.). https://engage.awwa.org/PersonifyEbusiness/Store/Product-Details/productId/39314942 (accessed December 11, 2022).

[252] D. Escarabajal-Henarejos, D. Parras-Burgos, L. Ávila-Dávila, F.J. Cánovas-Rodríguez, J.M. Molina-Martínez, Study of the Influence of Temperature on Boron Concentration Estimation in Desalinated Seawater for Agricultural Irrigation, Water 13 (2021) 322. https://doi.org/10.3390/w13030322.

[253] A.H. Haidari, R. Gonzalez-Olmos, S.G.J. Heijman, Scaling after remineralisation of reverse osmosis permeate, Desalination 467 (2019) 57–63. https://doi.org/10.1016/j.desal.2019.06.002.

[254] D. Paul, Reformulation of the solution-diffusion theory of reverse osmosis, Journal of Membrane Science 241 (2004) 371–386. https://doi.org/10.1016/j.memsci.2004.05.026.

[255] J.G. Wijmans, R.W. Baker, The solution-diffusion model: a review, Journal of Membrane Science 107 (1995) 1–21. https://doi.org/10.1016/0376-7388(95)00102-I.

[256] Membrane Technology and Applications | Wiley Online Books, (n.d.). https://onlinelibrary-wiley-com.huaryu.kl.oakland.edu/doi/book/10.1002/9781118359686 (accessed June 30, 2023).

[257] J. Li, H. Sun, X. Ye, S. Gao, J. Yang, Economic evaluation of 20,000 M3/Day seawater desalination coupling with floating reactor nuclear power plant, IOP Conf. Ser.: Earth Environ. Sci. 300 (2019) 042053. https://doi.org/10.1088/1755-1315/300/4/042053.

[258] U. Caldera, C. Breyer, Learning Curve for Seawater Reverse Osmosis Desalination Plants: Capital Cost Trend of the Past, Present, and Future, Water Resources Research 53 (2017) 10523–10538. https://doi.org/10.1002/2017WR021402.

[259] S. Loutatidou, N. Liosis, R. Pohl, T.B.M.J. Ouarda, H.A. Arafat, Wind-powered desalination for strategic water storage: Techno-economic assessment of concept, Desalination 408 (2017) 36–51. https://doi.org/10.1016/j.desal.2017.01.002.